

Studies on the effect of internal geometry in the macroscopic deformation of solids

Ph.D. Thesis

By

T Venkatesh Varma



DEPARTMENT OF CIVIL ENGINEERING

INDIAN INSTITUTE OF TECHNOLOGY INDORE

DECEMBER 2022

Studies on the effect of internal geometry in the macroscopic deformation of solids

A THESIS

submitted to the

INDIAN INSTITUTE OF TECHNOLOGY INDORE

in partial fulfillment of the requirements for

the award of the degree

of

DOCTOR OF PHILOSOPHY

By

T Venkatesh Varma



DEPARTMENT OF CIVIL ENGINEERING

INDIAN INSTITUTE OF TECHNOLOGY INDORE

DECEMBER 2022



INDIAN INSTITUTE OF TECHNOLOGY INDORE

CANDIDATE'S DECLARATION

I hereby certify that the work which is being presented in the thesis entitled **Studies on the effect of internal geometry in the macroscopic deformation of solids** in the partial fulfillment of the requirements for the award of the degree of **Doctor of Philosophy** and submitted in the **Department of Civil Engineering, Indian Institute of Technology Indore**, is an authentic record of my own work carried out during the time period from July 2019 to December 2022 under the supervision of Dr. Saikat Sarkar, Assistant Professor, Indian Institute of Technology Indore, Indore, India.

The matter presented in this thesis has not been submitted by me for the award of any other degree of this or any other institute.

T. Venkatesh Varma
26/04/2023

Signature of the Student with Date

(T Venkatesh Varma)

This is to certify that the above statement made by the candidate is correct to the best of my knowledge.

S. 26/4/2023

Signature of Thesis Supervisor with Date

(Dr. Saikat Sarkar)

T Venkatesh Varma has successfully given his Ph.D. Oral Examination held on

25 April, 2023

ACKNOWLEDGEMENTS

I would like to take this opportunity to express my heartfelt gratitude to a number of persons who in one or another other way contributed by making this time learnable, enjoyable, and bearable. First, I would like to thank my supervisor **Dr. Saikat Sarkar**, who was a constant source of inspiration during my work. Without his constant guidance and research directions, this research work could not be completed. His continuous support and encouragement have motivated me to remain streamlined in my research work.

I am very thankful to my research collaborators **Prof. Richard V. Craster** and **Prof. Sébastien R L Guenneau** for inviting me to Imperial College London and constantly supporting me during my stay there. I would also like to thank **Dr. Stéphane Brûlé** (Seismic Hazard Expert, Menard, France), **Dr. Bogdan Ungureanu** (Associate Researcher, Department of Mathematics, Imperial College London), and **Dr. Mohammad Masiur Rahaman** (Assistant Professor, IIT Bhubaneswar) for collaborating with us on various stages of my research. Their valuable comments and suggestions helped me to improve my work at various stages. I greatly acknowledge **Dr. Abhijit Ghosh**, Department of Metallurgy Engineering and Materials Science, IIT Indore for his suggestions on the practical feasibility of my work.

I would like to appreciate the fine company of my dearest colleagues and friends especially, **Mukul Saxena**, **Gyanesh Patnaik**, **Anshul Kaushik**, **Revanth Dugalam**, and **Vinay Kumar Sharma**.

My sincere acknowledgment and respect to the Ministry of Human Resource Development (MHRD India), Scheme for Promotion of Academic Research and Collaboration (SPARC India), Research and Development section (IIT Indore), and Finance and Accounts section (IIT Indore) for supporting me with various scholarships and grants to conduct my research smoothly. I would like to highly appreciate the Civil Engineering Department staff members for their unfailing support and assistance throughout my research.

Finally, I would like to express my heartfelt respect to my parents and brother for

the love, care, encouragement, and support they have provided to me throughout my life.

T Venkatesh Varma

To my Parents

Abstract

A comprehensive understanding of the arrangements of internal geometries in solids is essential to predict their macroscopic response which evolves with time and space under external loading and ultimately leads to their failure. The internal geometries may vary over a wide range of length scales (from nanometer to meter) and at times can be highly complex, and heterogeneous and can exhibit nonlinear constitutive relations. Altering the internal geometries of a solid in an appropriate manner can enhance the overall macroscopic response leading to an efficient design. As a part of this thesis, we study the effect of internal geometry in the form of heterogeneity arising from periodic inclusions. Towards this, we borrow ideas from the analysis of mechanical metamaterials. However, large-scale implementation of metamaterial designs is rather a recent and less explored phenomenon. One such implementation is seismic metamaterials (length-scale of meter-Order) used to shield earthquake forces. But most of the works are on the experimental front and lack on the modeling front. Another interesting implementation is a metamaterial-based design of armor (length-scale of millimeter-Order) which remained largely unexplored to date. The basic idea is similar to a crystal lattice with periodic structure, when local resonators are placed in the form of stiffer inclusions, they collectively show nonintuitive behavior such as large attenuation of elastic waves. This thesis uses such a concept of metamaterials to design efficient solids with specific applications to seismic metamaterials and armor design. Initially, the effect of internal geometries (in the form of inclusion shapes and orientations) on modulating frequency bandgap is studied. This is shown with specific application to seismic metamaterials which can be deployed to shield/divert earthquake waves. It is observed that a square-shaped inclusion with sides aligned with the sides of a square lattice performs better than any other shape of the inclusions in a linear regime. After arriving at a particular choice of shape for inclusions, we test its fracture properties (fracture toughness and fracture strength). Here, it is observed that high fracture toughness and high fracture strength than its constituent material, similar to that possessed by nacre, can be achieved simultaneously if the

inclusions are compressively prestressed. Such a design is helpful in developing an efficient front panel of protective armor. Still, a stress wave will be transmitted to the back panel of the armor and we show that a metamaterial-based polymer backing panel (in which the inclusions are in form of cubic voids) can efficiently absorb the energy and attenuate the stress wave drastically in comparison to its bulk solid counterpart. En route to this, we show that the detailed finite element modeling for the internal geometries of the solid can be bypassed by using a coarse-grained formulation which is capable of accurately capturing its macroscopic response.

Keywords: Seismic metamaterials, Dispersion curves, Transmission loss, Periodic microstructure, Prestressed inclusions, High-performance composites, High fracture toughness, High fracture strength, Protective armors, coarse-graining, Finite element method (FEM), Energy absorption, Polymer-based metamaterial

List of Publications

A. Published

A1. In Refereed Journals

1. **Varma, T. V.**, Ungureanu, B., Sarkar, S., Craster, R., Guenneau, S. R. L., and Brûlé, S. *The influence of clamping, structure geometry and material on seismic metamaterial performance*, *Frontiers in Materials*, vol. 8, pp. 106, 2021 (Frontiers), DOI = “<https://doi.org/10.3389/fmats.2021.603820>”. (**IF: 3.985**)
2. **Varma, T. V.** and Sarkar, S. *Designing polymer metamaterial for protective armor: a coarse-grained formulation*, *Meccanica*, vol. 56(2), pp. 383-392, 2021 (Springer Netherlands), DOI = “<https://doi.org/10.1007/s11012-020-01201-6>”. (**IF: 2.538**)
3. **Varma, T. V.**, Rahaman, M. M., and Sarkar, S. *A numerical study to assess the role of pre-stressed inclusions on enhancing fracture toughness and strength of periodic composites*, *International Journal of Fracture*, pp. 1-17, 2022 (Springer Netherlands), DOI = “<https://doi.org/10.1007/s10704-022-00663-x>”. (**IF: 2.986**)

A2. In Refereed Conferences

1. **Varma, T. V.** and Sarkar, S. *Designing a polymer metamaterial with high energy absorption capability*, 14th World Congress on Computational Mechanics and ECCOMAS Congress (WCCM-ECCOMAS), Paris, France, January 2021 (Presented Online due to COVID).

B. To be Communicated

In Refereed Journals

1. Ungureanu, B., **Varma, T. V.**, Movchan, M., Achaoui, Y., Sarkar, S., Movchan, N., Enoch, S., Craster, R., Brûlé, S., and Guenneau, S. R. L., (2023). Seismic wave shield with cubic arrays of split-ball resonators.
2. **Varma, T. V.**, & Sarkar, S. (2023). A finite element formulation for computing dispersion diagrams and transmission losses in a mechanical metamaterial.
3. **Varma, T. V.**, & Sarkar, S. (2023). A homogenization theory for solids with a periodic arrangement of the inclusions.
4. **Varma, T. V.**, & Sarkar, S. (2023). A numerical study on the effect of inclusion types and shapes on the fracture properties of a periodic composite media.

Contents

Abstract	i
List of Publications	iii
List of Figures	ix
List of Tables	xiii
List of Abbreviations and Acronyms	xv
1 Introduction	1
1.1 Background and Motivation	3
1.2 Objectives	4
1.3 Organization of the Thesis	4
2 Literature Survey and Research Methodology	7
2.1 Importance of internal geometries in structures	7
2.2 Overview of periodic materials	8
2.3 Emergence of mechanical metamaterials	10
2.4 Basic theories of metamaterials	11
2.5 Finite element modeling for metamaterials	13
2.6 Fracture analyses on periodic materials	17
3 The Influence of Clamping, Structure Geometry, and Material on Seismic Metamaterial Performance	19
3.1 Introduction	20

3.2	Mathematical Formulation-Finite Element Approach	24
3.3	Results and Discussion	26
3.3.1	Comparison of different geometry of inclusions	26
3.3.2	Effect of varying orientation in square inclusions	38
3.3.3	Feasibility of inclusion material	40
3.4	Summary	45

4 A numerical study to assess the role of pre-stressed inclusions on enhancing fracture toughness and strength of periodic composites **47**

4.1	Introduction	48
4.2	Boundary value problem	51
4.2.1	Crack modelling	52
4.2.2	XFEM discretisation	53
4.2.3	Crack propagation	54
4.2.4	Fracture toughness	56
4.3	Numerical simulations	57
4.3.1	Simulation set-up	57
4.3.2	Toughening and strengthening mechanism in mode-I fracture	62
4.3.3	Toughening and strengthening mechanism in Mode II fracture	67
4.4	Summary	71

5 Designing polymer metamaterial for protective armor: A coarse-grained formulation **73**

5.1	Introduction	74
5.2	Mathematical formulation for coarse-grained description	77
5.3	Validation of coarse-grained methodology	83
5.4	Numerical results and discussion	85
5.4.1	Comparison of polymer metamaterial with its solid counterpart	85
5.4.2	Effect of an increasing number of layers in polymer metamaterial	87

5.4.3	Effect of varying fiber length and thickness in the microstructural geometry of polymer metamaterial	88
5.5	Summary	89
6	Conclusions and Future Work	91
6.1	Conclusions	91
6.2	Future Research Directions	93
	Bibliography	94

List of Figures

1.1	Arrangement of internal geometries in a 2D plate.	2
2.1	Periodic structures	9
2.2	Representation of a direct lattice (left figure) and Irreducible Brillouin zone (IBZ) in the reciprocal lattice (right figure).	12
3.1	Floquet-Bloch band diagrams for cylindrical inclusions obtained for a modulus of Bloch wavevector $ \mathbf{k} $, that describes the edges of the irreducible Brillouin zone ΓXM	23
3.2	Representative eigenmodes for cylindrical inertial resonators (IRs) with four inclined ligaments at high-symmetry point X of the irreducible Brillouin zone ΓXM : (A,E) Rotational mode at 48.5 Hz (IR clamped at bottom, third mode in Figure 3.1D); (B,F) Rotational mode 38.6 Hz (fourth mode in Figure 3.1B); (C,G) Longitudinal mode at 45.8 Hz (sixth mode in Figure 1B); (D,H) Torsional mode at 63.8 Hz (seventh mode in Figure 3.1B).	24
3.3	Unclamped configuration of (a) cylindrical, (c) regular-shaped square, and (e) notch-shaped square geometry inclusions in the elementary cell of periodic media (medium soil) with equal substitution ratio (0.445) and their corresponding dispersion curves (b,d,f)	29
3.4	Dispersion curves for clamped configuration of geometries shown in fig.3.3 with substitution ratio 0.445.	30
3.5	Dispersion curves and eigen modes of cylindrical inclusions for clamped and unclamped configurations.	31

3.6	Unclamped configuration of (a) coil/Labyrinthine, (c) 4 gaps split-ring and (e) 2 gaps split-ring with steel as an inclusion with substitution ratio 0.445 in medium soil matrix and corresponding dispersion curves (b, d, f).	33
3.7	Unclamped configuration of cylindrical swiss roll like geometry with different thickness of steel inclusions in medium soil matrix. Diameter of swiss roll is considered same as solid circular inclusions in Fig. 3.3.	34
3.8	Dispersion curves for unclamped configuration of Labyrinthine geometry as shown in fig. 3.6(a) with different constituent material, i.e., (a) rubber and (b) concrete.	34
3.9	Dispersion curves for clamped configuration with steel as inclusion material for (a) Labyrinthine, (b) 4 gaps split ring, and (c) swiss roll with 0.128 m thickness with substitution ratio as 0.445 (for swiss roll: 0.15).	35
3.10	Dispersion curves for unclamped configurations of Labyrinthine and 2 gap split ring steel inclusions with 0.445 substitution ratio in soft, very soft clay type 1 and very soft clay type 2.	36
3.11	Unclamped configuration (all three type of inclusion, i.e., concrete, rubber and steel), and Variation of bandgap width versus substitution ratio of triphasic inclusion in soft soil.	37
3.12	Effect of change in orientation angle (in degrees) of unclamped regular-shaped square steel inclusion with 0.445 substitution ratio in medium soil on bandgap.	39
3.13	Transmission loss for 0° and 45° oriented square steel inclusion in medium soil matrix (bottom remains unclamped).	40
3.14	Unclamped configuration of concrete inclusion (with 0.445 substitution ratio) in (a) medium soil; (c) very soft soil and corresponding dispersion curves (b,d).	42
3.15	Transmission losses for unclamped concrete inclusions in very soft soil type 1 and medium soil matrix corresponding to Fig. 3.14.	42

3.16 Dispersion curve for clamped configuration of M50 grade square concrete columns in soft soil matrix.	43
3.17 Attenuation for clamped configuration of square concrete columns in soft soil type 1 and medium soil matrix.	43
3.18 Schematic representation of the proposed design for metamaterial.	44
3.19 Bandgap versus substitution ratio plot for clamped configuration of square concrete inclusions.	45
4.1 Left sub-figure shows the periodic micro-structure described by an open set Ω with boundary $\partial\Omega = \partial\Omega_u \cup \partial\Omega_t \cup \partial\Omega_{cr} \cup \partial\Omega_0$. The domain Ω can be identified as the assembly formed by repetition of the unit cell, Ω^c having isotropic phases separated by Γ , as shown in the right sub-figure.	52
4.2 Effect of periodicity with hard inclusions under mode-I loading. A compressive pre-stress of 250 MPa is applied to the inclusions.	58
4.3 Effect of inclusion shape on fracture toughness under mode-I loading. A compressive pre-stress of 250 MPa is applied to the inclusions.	58
4.4 Convergence plot with different mesh sizes. Good convergence is shown for the mesh size 0.02 mm.	59
4.5 Simulation setup for mode-I crack propagation.	62
4.6 Toughening mechanism in mode-I fracture with hard inclusions ($\sigma_0=0$).	63
4.7 Toughening and strengthening effect in mode-I fracture with pre-stressing the hard inclusions in the principal y-direction only.	65
4.8 Toughening and strengthening effect in mode-I fracture with hard inclusions for uniaxial and biaxial, compression and tension pre-stressing force.	65
4.9 Toughening and strengthening effect in mode-I fracture with pre-stressing the soft inclusions in the principal y-direction only.	66
4.10 Toughening and strengthening effect in mode-I fracture with soft inclusions for uniaxial and biaxial, compression and tension pre-stressing force.	67

4.11 Toughening and strengthening effect in mode II fracture with hard inclusions.	68
4.12 Crack propagation under mode-II loading with $\sigma_0 = 0$	69
4.13 Toughening and strengthening effect in mode-II fracture with hard inclusions for uniaxial and biaxial, compression and tension pre-stressing force.	69
4.14 Toughening and strengthening effect in mode-II fracture with soft inclusions pre-stressed in the principal y-direction.	70
4.15 Toughening and strengthening effect in mode-II fracture with soft inclusions for uniaxial and biaxial, compression and tension pre-stressing force.	71
5.1 Schematic representation of a 3 layered polymer metamaterial panel (PMP).	78
5.2 FEM simulations to obtain elastic coefficients of connector filaments, i.e., (a) bending, (b) shear, and (c) stretch. Dimensions $L=0.25$ mm, $l=0.01$ mm and $w=d=0.1$ mm.	82
5.3 A two-layered PMP of armor with a dimension of each fiber element as, $L = 0.25$ mm, $w=d=0.1$ mm and connector as, $l=0.01$ mm, subjected to pulling by a uniformly distributed load on selected fibers.	84
5.4 Load Vs displacement plot for a two-layered PMP (corresponding to fig.5.3), simulated using full-scale finite element analysis (continuous marked line) and proposed coarse-grained formulation (star marked line).	84
5.5 Comparison of transmission losses in polymer metamaterial (PMP) and its solid counterpart bulk polymer matrix (SPP), both having thicknesses of 2 mm.	86
5.6 Comparison of transmission losses in a 4-layered and 8-layered polymer metamaterial (PMP).	87
5.7 Comparison of transmission losses in a 4-layered PMP design of armor with finer and coarser arrangement of fibers in its microstructure.	89

List of Tables

3.1	Geometry of the microstructures of seismic metamaterial	37
3.2	Material properties used in the design of seismic metamaterial	38
4.1	Ceramic material properties (taken from [1, 2])	61

List of Abbreviations and Acronyms

Al₂O₃ Alumina

AM Additive Manufacturing

BCC Body Centered Cubic

BCs Boundary Conditions

BFS Back Face Signature

BI Base Isolation

BZ Brillouin Zone

COD Crack Opening Displacement

DOF Degree of Freedom

ERR Energy Release Rate

FEM Finite Element Method

IBZ Irreducible Brillouin Zone

IRs Inertial Resonators

LEFM Linear Elastic Fracture Mechanics

MM Mechanical Metamaterials

PMM Polymer based Mechanical Metamaterial

PMP Polymer Metamaterial Panel

SBCs Surfing Boundary Conditions

SiC Silicon Carbide

SIF Stress Intensity Factor

SIMT Stress Induced Martensitic Transformation

SM Seismic Metamaterial

SPP Solid Polymer Panel

STF Shear Thickening Fluid

TMD Tuned Mass Dampers

XFEM Extended Finite Element Method

Chapter 1

Introduction

A comprehensive understanding of the deformation and failure mechanism in structures is crucial for large-scale engineering problems. This serves as a basis to refine the guidelines to arrest failure mechanisms and prevent further failure events which eventually improves the structure's intended service. The deformation of a solid is characterized by its mechanical response, which does not only depend on its intensive properties, such as density, elastic modulus, Poisson's ratio, etc., but also on the subsystem's internal geometry and its arrangements. The internal geometry collectively defines the shape of a unit cell and the shape of its inclusions in a periodic setup. The inclusions can also have voids, defects or imperfections. Fig. 1.1 shows the different arrangement of the "internal geometry". Fig. 3.3(a) shows the square shaped unit cell with different shape of the voids in it, whereas fig. 1.1(b) shows the unit cell with different inclusion shapes in it. By tweaking these geometrical parameters, such as unit cell shape, size, inclination angle, etc. one can get insights about the local response, which affects the bulk, an overall response such as modulating frequency bandgap, attenuating stress waves, crack bending, improving energy absorption capability, etc. For instance, adding a strut to BCC micro lattice of a stainless steel wire mesh (typically used in transport conveyor belts) increases its stiffness and changes its deformation modes. Thus, the mechanical response of a solid is directly related to the underlying details of the internal geometries (also called unit cells/micro-structure), which at times can be highly heterogeneous, complex, and can have non-linear con-

stitutive relations. This in-situ mechanical approach unfolds the interface mechanics and leads to a strengthening mechanism.

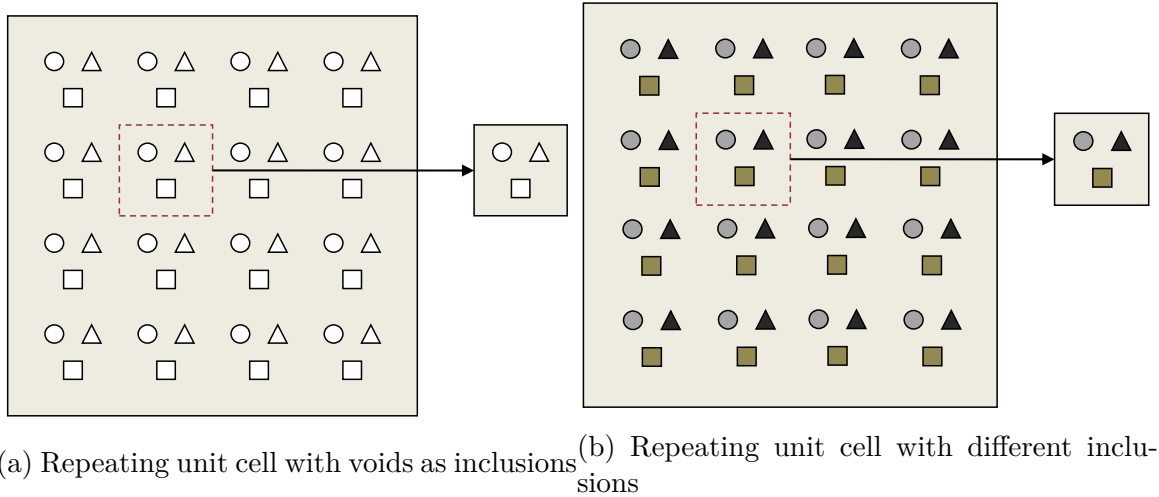


Figure 1.1: Arrangement of internal geometries in a 2D plate.

The applicability may vary over a wide range of length scales (from nanometer to meter) of the solid's microstructural geometry. This concept immediately reminds us of composites, known as metamaterials, which are assemblies of multiple elements usually arranged in periodic patterns at sub-wavelength scales. These composites do not only derive their properties from the constituent materials, but also from the combination of elements with given shapes and orientations, such as the consecrated split ring resonators and swiss-rolls [3]. With unusual material properties and advanced functionalities, metamaterials can be a key to revolutionizing the mechanics and structural engineering field. Their remarkable features like programmable frequency bandgap, negative poisson's ratio, malleability, etc. make it possible to control, divert or shield the elastic waves/stress waves. This thesis uses the concept of metamaterials to show the effect of varying the internal geometries and their material constituents on the macroscopic properties (such as modulating frequency bandgaps, crack propagation, energy absorption, etc.) of a solid body.

1.1 Background and Motivation

Understanding structural deformation serves as a key to solving many engineering problems. An important aspect of this is to save structures against vibrations caused by elastic waves propagating through them.

While there are techniques to suppress structural vibrations via external means, there are certain limitations in some of these approaches, e.g., Tuned Mass Dampers (TMD) and Base Isolations (BI) [4, 5, 6, 7, 8, 9]: BI induces large movement of the structures which may not be acceptable, TMD works only for a narrow frequency range outside of which it may work adversely which is again a major issue because identifying the frequency contents in the structure correctly is not straightforward as it may change significantly with time due to structural degradation and environmental change [10, 11]. In this context, metamaterials, if exploited appropriately, can provide us with robust strategies.

Metamaterials at the micro- and nanometer scales have already shown tremendous impact in photonics and phononics, their extensions to solving large-scale engineering problems are a rather recent and less explored phenomenon. One such large-scale implementation is seismic metamaterial (SM) which can be used as an earthquake shield. The basic idea is to deploy a series of resonators buried in soil or above-surface around a structure so that certain frequencies of seismic waves cannot propagate through them and affect the primary structure, which can be a building, a bridge, or an entire city. These resonators are typically conceived in the form of periodically placed tubes inside the soil or above the surface forest of trees [12]. Another interesting large-scale application is a metamaterial-based armor design. In engineering new types of composite armors, their material constituents play an important role in translating the kinetic energy of the impacts into internal energy, which many researchers have explored [13]. However, a metamaterial-based armor design can enhance the overall performance in terms of retarding the impact projectile penetration (function of the front metal panel), transmitting the shock wave, or dissipating the energy (function of the back polymer panel). These composites usually derive their non-intuitive prop-

erties from the arrangement of the unit cell geometry and the same has remained unexplored to date. The effect of varying the geometry of the unit cell and their material constituents on the macroscopic properties of a solid body is not yet addressed such as the variation in frequency bandgaps, fracture toughness, fracture strength, energy absorbing capacity, etc. Moreover, analyzing metamaterials involves extreme computational overhead in solving the continuum equations which is not possible to afford for the large engineering scale of our interest.

1.2 Objectives

Based on the above discussion, we aim to achieve the following objectives in this thesis:

- [1] To study the effect of different types of internal geometries and material constituents in modulating frequency contents in the propagating waves, with application to seismic metamaterials.
- [2] To study the effect of internal geometry on fracture toughness and fracture strength in a solid with periodic inclusions with application to designing armor front panel.
- [3] To develop a coarse-grained formulation to effectively compute the overall response of a solid with internal geometries with application to designing armor backing panel.

1.3 Organization of the Thesis

The thesis is organized into six chapters which are as follows;

- [1] Chapter 1: Includes the introduction to the thesis topic, the importance of the study, research background, objectives of the study, and thesis organization.

- [2] Chapter 2: Covers past literature relevant to the work, the basic theory of 3D elastic equations incorporating Bloch's theorem to analyze the periodic medium.
- [3] Chapter 3: Discuss the effect of different geometry and material constituents in modulating frequency contents in the propagating wave. This is shown with specific applications to seismic metamaterials on a meter scale.
- [4] Chapter 4: Shows the effect of internal geometry on fracture toughness and fracture strength in a solid with periodic inclusions. A strategy for designing a metamaterial-based front panel of body armor is discussed.
- [5] Chapter 5: Describes a coarse-grained formulation to effectively compute the overall response of a solid body with periodic voids. This is shown with specific application to a polymer-based metamaterial backing panel of body armor.
- [6] Chapter 6: This chapter draws some conclusions about the overall study and possible future directions.

Chapter 2

Literature Survey and Research

Methodology

This chapter provides an overview of the importance of internal geometries in a solid body, the relevant theories of metamaterials, and the computational methodology used to analyze them. The whole chapter is divided into five sections. Section 2.1 draws the users attention toward understanding the importance of internal geometries in structures with reference to some past studies. Section 2.2 shows an overview of the periodic materials with emphasis on their periodicity. Section 2.3 shows the emergence of metamaterials which are basically an arrangement of inclusions (internal geometry in our case) in a periodic pattern in a given matrix. Then the basic theories which will be used to analyze a metamaterial are discussed in section 2.4. Section 2.5 discusses a finite element based modeling for the metamaterials.

2.1 Importance of internal geometries in structures

Studies on the internal geometry of structures have been the focus of research for many decades, e.g., from biological systems to aircraft designs [14, 15]. Here, we consider voids and inclusions as a source of altering internal geometry in a solid body. Such a source gives rise to heterogeneity in the material. It is well known that such geometries offer variation in the macroscopic response by a change in volume fraction,

e.g., heat conductance through a porous medium increases with an increase in the pore size [16, 17]. However, a change in the macroscopic response can also be achieved by changing their shapes, orientation, and spatial distribution at the same volume fraction. This offers many engineering advantages such as a cost-effective design and removing fabrication difficulties involved with different materials.

The importance of internal geometry in structures can be seen in many past studies. The length scale of these geometries may vary from micro-meter to meter. Cao *et al.* [18] studied the effect of inclusion shapes and orientations on plastic and viscoplastic deformations of a rock mineral. It is observed that there is less influence of this on the macroscopic yield stress, however, there are significant influences on macroscopic plastic and viscoplastic strains. This also shows that all the macroscopic properties will not be affected by microscopic changes in the internal geometries. Internal geometries are also important in the case of industrial precipitators where the crystallizer size determines the quality of precipitated particles [19]. Not only in metal or ceramics, internal geometries also play a crucial role in polymers too. Jayan *et al.* have shown the influence of internal geometries on woven-like structures whose chemical constituent is an E-glass tow [20]. Similarly, Vallons *et al.* showed a new stitching pattern as an alteration to the internal geometries of a fabric composite and observed strength variation in the longitudinal and transverse directions [21]. These internal geometries when arranged in a repetitive sense form a periodic pattern that holds exotic properties during the dynamic behavior of a structure.

2.2 Overview of periodic materials

Periodic structures are known to attract the interest of many well-known scientists such as Cauchy, Lord Rayleigh, Kelvin, Vincent etc. since the early 19th Century. Most of the works during that time involved in developing electric filters out of periodic networks [22, 23]. Later, Bloch proposed a generalized theory for Floquet's results for the wavy nature of a particle moving in a periodically repeating environment [24]. The theory today is known as Bloch's theorem for wave propagation in a periodic medium

and fits in many applications [25, 26, 27, 28]. A detailed description of this theory is given in the section 2.4 of this chapter in the context of metamaterials. For a detailed study on wave propagation in the periodic medium, one can refer to Brillouin's Book [29].

The periodicity of a structure can be defined in one-dimensional (1D), two-dimensional (2D), or three-dimensional (3D) as shown in figure 2.1, composed of the smallest repeating element known as a unit cell. Researchers have observed that these periodic structures may hold exotic properties, e.g., vibration shielding [30, 31, 32, 33]. One may note that the dynamic behavior of structures is a complex phenomenon and analyses of large structures such as aircraft is computationally very expensive. However, if these structures are composed of repeating substructures, the analyses become easier since we will be dealing only with the substructure with periodicity incorporated. Now, if we introduce the geometric and material periodicity in the mathematical modeling of these structures, their dynamic behavior can be represented as a wave propagating through the structure and this gave rise to the concept of mechanical metamaterials which is discussed in the next subsection. Thus, the computational effort depends only on the complexity of the substructure (or unit cell in our case) rather than the whole structure.

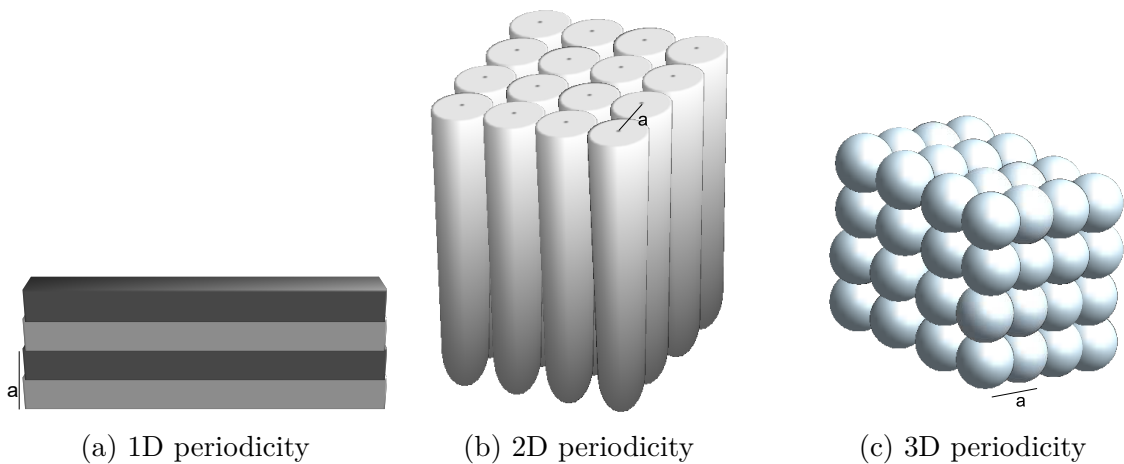


Figure 2.1: Periodic structures

2.3 Emergence of mechanical metamaterials

In the parallel research area of electromagnetism, there is a keen interest in composites, known as metamaterials, which are assemblies of multiple elements usually arranged in periodic patterns at subwavelength scales. These materials were introduced as a means to achieve effective electromagnetic properties not from the properties of the constituent materials, but from the combination of elements with given shapes and orientations, such as split ring resonators [34]. Such periodically arranged elements take their name from the shape of the thin metal sheets they are made of that allow for artificial magnetism, not present in the constituent materials (metal surrounded by plastic, neither of which are magnetic media), through the precise manipulation of electric and magnetic components of the electromagnetic field and their interplay. Indeed, the electromagnetic field is tremendously enhanced due to internal capacitance and inductance phenomena upon the resonance of the thin sheets. From the highly dispersive nature of the metamaterials around the resonant frequencies of split ring resonators and other arrangements, such as swiss-rolls, it is possible to block, absorb, enhance, or even bend electromagnetic waves propagating through a doubly or triply periodic array of them, as low-frequency stopbands and strong anisotropy (apparent in distorted isofrequency contours in pass bands) take place [35].

The story of metamaterials doesn't end with electromagnetism. Later, a new class of materials, known as mechanical metamaterials (MM), showed nonintuitive mechanical properties when combined with different structures. Early in 1987, Lakes experimentally showed that a material can have a negative Poisson's ratio, i.e., it expands laterally when stretched in contrast to the ordinary materials [36]. Thereon a series of works have been done on mechanical metamaterials, both experimentally and numerically, which show nonintuitive mechanical properties, e.g., negative compressibility MM [37], auxetic MM [38, 39], multistable MM to trap energy [40, 41], Programmable MM [42, 43], Soft MM [44], bio-inspired MM [45], topological MM [46], etc. Most of the studies on MM were confined to nano- and micro-scale and their large-scale extension on the meter-scale remained unexplored. However, the last

decade has seen their meter-scale applications too, e.g. forest trees acting as a MM to attenuate Rayleigh waves [47], seismic metamaterials (SMs) [48, 49], etc. Mechanical metamaterials if designed appropriately can actually shield frequency contents ranging from a few hertz to kilo-hertz. The relevant literature used in the work is shown in the subsequent chapters for convenience.

2.4 Basic theories of metamaterials

The basic theories of metamaterials are derived from solid-state physics concepts. We start with understanding the term reciprocal lattice, which plays a crucial role in periodic structures. In general, the reciprocal lattice is the Fourier transform of a direct lattice, if the latter is a periodic spatial function in real space. The reciprocal lattice represents a reciprocal space of spatial frequencies containing all sets of wavevectors in the Fourier series. Suppose, we define the direct lattice as $\mathbf{R}_n = n_1\mathbf{a}_1 + n_2\mathbf{a}_2 + n_3\mathbf{a}_3$ where \mathbf{a}_i is the primitive vectors and $n_i \in \mathcal{Z}$; \mathcal{Z} is the set of integers. Its reciprocal lattice is represented as $\mathbf{G}_m = m_1\mathbf{b}_1 + m_2\mathbf{b}_2 + m_3\mathbf{b}_3$ where $m_i \in \mathcal{Z}$ and $\mathbf{b}_i = \frac{2\pi}{V}\mathbf{a}_j \times \mathbf{a}_k$; $V = \mathbf{a}_i \cdot \mathbf{a}_j \times \mathbf{a}_k$; $\{i, j, k\} = \{1, 2, 3\}$.

Next, we describe the Brillouin zone (BZ) which is a primitive cell of the reciprocal lattice as described above. BZ for a direct lattice is shown in figure 2.2. n^{th} BZ is the locus of all points reachable from the origin of the reciprocal lattice by exactly crossing $n - 1$ distinct Bragg planes. Consequently, we define the Irreducible Brillouin Zone (IBZ) as the first BZ reduced by all of the symmetries in the point group of the reciprocal lattice, i.e., the wavevector k is swept from 0 to π/a as shown in the figure.

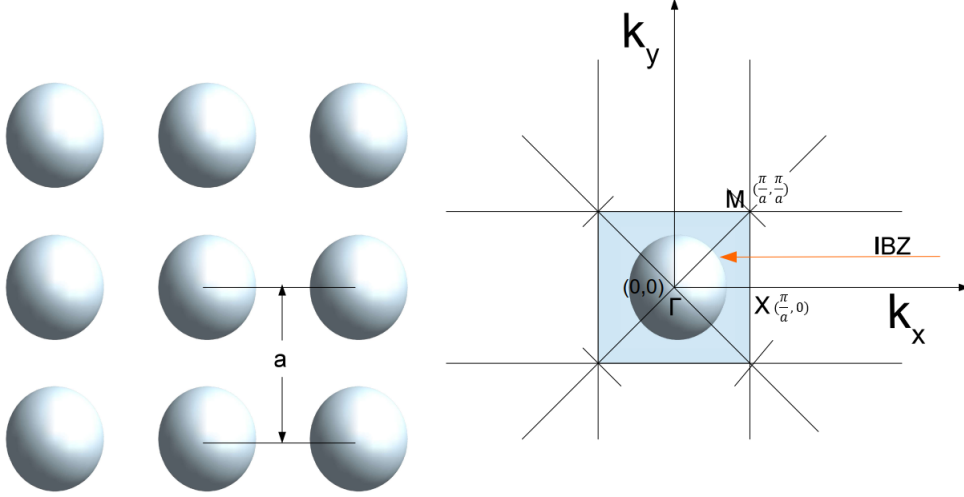


Figure 2.2: Representation of a direct lattice (left figure) and Irreducible Brillouin zone (IBZ) in the reciprocal lattice (right figure).

Now, it comes to account for the periodicity of the lattice. Here we use Floquet-Bloch periodic condition and express the displacement vector $\mathbf{u}(\mathbf{r})$ as:

$$\mathbf{u}(\mathbf{r}, t) = \tilde{\mathbf{u}}(\mathbf{r})e^{i(\mathbf{k}\cdot\mathbf{r}-\omega t)} \quad (2.1)$$

where, ω is the angular frequency and $\tilde{\mathbf{u}}$ is the displacement modulation function whose periodicity is identical to the lattice periodicity:

$$\tilde{\mathbf{u}}(\mathbf{r} + \mathbf{a}) = \tilde{\mathbf{u}}(\mathbf{r}) \quad (2.2)$$

$\mathbf{k} = (k_x, k_y, k_z)$ is the wavevector along the X, Y, and Z-direction of the BZ. Using Eq. (2.2) in Eq. (2.1), we get:

$$\begin{aligned} \mathbf{u}(\mathbf{r} + \mathbf{a}, t) &= \tilde{\mathbf{u}}(\mathbf{r} + \mathbf{a})e^{i(\mathbf{k}\cdot(\mathbf{r}+\mathbf{a})-\omega t)} \\ &= e^{i\mathbf{k}\cdot\mathbf{a}}\tilde{\mathbf{u}}(\mathbf{r})e^{i(\mathbf{k}\cdot\mathbf{r}-\omega t)} \\ &= e^{i\mathbf{k}\cdot\mathbf{a}}\mathbf{u}(\mathbf{r}, t) \end{aligned} \quad (2.3)$$

Eq. (2.3) represents the periodic boundary conditions for the displacement function. This implies that the output wave is having a phase difference of $\mathbf{k} \cdot \mathbf{a}$ with the input wave. The dispersion diagrams presented in this thesis are obtained by substituting

Eq. (2.3) in the governing equation of motions (shown in the subsequent chapters) and solving an eigenvalue problem.

2.5 Finite element modeling for metamaterials

We take an elastic medium consisting of isotropic homogeneous phases, for which the governing equation is [50]:

$$(\lambda + \mu) \frac{\partial^2 u_j}{\partial x_j \partial x_i} + \mu \frac{\partial^2 u_i}{\partial x_j \partial x_j} = \rho \frac{\partial^2 u_i}{\partial t^2} \quad (2.4)$$

which is valid in each homogeneous phase and is described by a constant density ρ and Lamé parameters $\lambda = \frac{E}{2(1+\nu)}$ and $\mu = \frac{E\nu}{(1+\nu)(1-2\nu)}$; E is the elastic modulus and ν is the Poisson's ratio of the isotropic phase. $\{u_i\}_{i=1}^3 = \{u, v, w\}$ is the displacement field vector having components u , v and w in the x, y and z-direction in space, respectively. On expanding and expressing in Cartesian coordinates, Eq. (2.4) takes the form;

$$\begin{aligned} (\lambda + \mu) (u_{xx} + v_{yx} + w_{zx}) + \mu (u_{xx} + u_{yy} + u_{zz}) &= \rho u_{tt} \\ (\lambda + \mu) (u_{xy} + v_{yy} + w_{zy}) + \mu (v_{xx} + v_{yy} + v_{zz}) &= \rho v_{tt} \\ (\lambda + \mu) (u_{xz} + v_{yz} + w_{zz}) + \mu (w_{xx} + w_{yy} + w_{zz}) &= \rho w_{tt} \end{aligned} \quad (2.5)$$

where the double subscript $(a)_{(bb)}$ represents the second order derivative of a with respect to b . For further analyses we consider the following solution forms for the field variables:

$$\begin{aligned} u &= \tilde{u}(\mathbf{r}) e^{(\mathbf{K} \cdot \mathbf{r} - i\omega t)} \\ v &= \tilde{v}(\mathbf{r}) e^{(\mathbf{K} \cdot \mathbf{r} - i\omega t)} \\ w &= \tilde{w}(\mathbf{r}) e^{(\mathbf{K} \cdot \mathbf{r} - i\omega t)} \end{aligned} \quad (2.6)$$

where, \mathbf{r} is the position vector, $\mathbf{K} = \{k_x, k_y, k_z\}$ is the wave number and ω is the frequency associated with the wave. The various derivatives in Eq. (2.5) can be written as the following using Eq. (2.6):

$$\begin{aligned}
u_{xx} &= [\tilde{u}_{xx} + 2i\tilde{u}_x k_x - k_x^2 \tilde{u}] e^{(\mathbf{K} \cdot \mathbf{r} - i\omega t)} \\
u_{xy} &= [\tilde{u}_{xy} + i\tilde{u}_y k_x + i\tilde{u}_x k_y - k_x k_y \tilde{u}] e^{(\mathbf{K} \cdot \mathbf{r} - i\omega t)} \\
u_{xz} &= [\tilde{u}_{xz} + i\tilde{u}_z k_x + i\tilde{u}_x k_z - k_x k_z \tilde{u}] e^{(\mathbf{K} \cdot \mathbf{r} - i\omega t)} \\
u_{yy} &= [\tilde{u}_{yy} + 2i\tilde{u}_y k_y - k_y^2 \tilde{u}] e^{(\mathbf{K} \cdot \mathbf{r} - i\omega t)} \\
u_{zz} &= [\tilde{u}_{zz} + 2i\tilde{u}_z k_z - k_z^2 \tilde{u}] e^{(\mathbf{K} \cdot \mathbf{r} - i\omega t)} \\
u_{tt} &= \omega^2 \tilde{u} e^{(\mathbf{K} \cdot \mathbf{r} - i\omega t)}
\end{aligned} \tag{2.7}$$

Similar expressions can be arrived at for the derivatives associated with v and w . Accordingly Eq. (2.5) can be written as:

$$\begin{aligned}
(\lambda + \mu) [\tilde{u}_{xx} + \tilde{v}_{yx} + \tilde{w}_{zx}] - \mu (\tilde{u}_{xx} + \tilde{u}_{yy} + \tilde{u}_{zz}) + ik_x [(\lambda + \mu) (2\tilde{u}_x + \tilde{v}_y + \tilde{w}_z) + 2\mu \tilde{u}_x] \\
+ ik_y [(\lambda + \mu) \tilde{v}_x + 2\mu \tilde{u}_y] + ik_z [(\lambda + \mu) \tilde{w}_x + 2\mu \tilde{u}_z] - k_x^2 [(\lambda + \mu) \tilde{u} + \mu \tilde{u}] - k_y^2 \mu \tilde{u} - k_z^2 \mu \tilde{u} \\
- k_x k_y (\lambda + \mu) \tilde{v} - k_x k_z (\lambda + \mu) \tilde{w} = -\rho \omega^2 \tilde{u}
\end{aligned} \tag{2.8}$$

We now perform the weak formulation for Eq. (2.8) as below:

$$\begin{aligned}
& -(\lambda + \mu) \left[\int_{\Omega} N_x \tilde{u}_x dV + \int_{\Omega} N_x \tilde{v}_y dV + \int_{\Omega} N_x \tilde{w}_z dV \right] \\
& - \mu \left(\int_{\Omega} N_x \tilde{u}_x dV + \int_{\Omega} N_y \tilde{u}_y dV + \int_{\Omega} N_z \tilde{u}_z dV \right) \\
& + ik_x \left[(\lambda + \mu) \left(2 \int_{\Omega} N \tilde{u}_x dV + \int_{\Omega} N \tilde{v}_y dV + \int_{\Omega} N \tilde{w}_z dV \right) \right] \\
& + 2\mu ik_x \int_{\Omega} N \tilde{u}_x dV \\
& + ik_y \left[(\lambda + \mu) \int_{\Omega} N \tilde{v}_x dV + 2\mu \int_{\Omega} N \tilde{u}_y dV \right] \\
& + ik_z \left[(\lambda + \mu) \int_{\Omega} N \tilde{w}_x dV + 2\mu \int_{\Omega} N \tilde{u}_z dV \right] \\
& - k_x^2 \left[(\lambda + \mu) \int_{\Omega} N \tilde{u} dV + \mu \int_{\Omega} N \tilde{u} \right] \\
& - k_y^2 \mu \int_{\Omega} N \tilde{u} dV - k_z^2 \mu \int_{\Omega} N \tilde{u} dV \\
& - k_x k_y (\lambda + \mu) \int_{\Omega} N \tilde{v} dV - k_x k_z (\lambda + \mu) \int_{\Omega} N \tilde{w} dV
\end{aligned} \tag{2.9}$$

$$= -\rho\omega^2 \int_{\Omega} N\tilde{u}dV$$

where N is 3D shape functions. Taking $\tilde{u}_x = N_j\hat{u}_j$, $\tilde{u}_y = N_j\hat{u}_j$, and $\tilde{u}_z = N_j\hat{u}_j$ (assuming Einstein's summation convention), and similarly for v and w , we arrive at the following equations:

$$\begin{aligned}
& -(\lambda + \mu) \left[\int_{\Omega} N_x N_{xj} dV \hat{u}_j + \int_{\Omega} N_x N_{yj} dV \hat{v}_j + \int_{\Omega} N_x N_{zj} dV \hat{w}_j \right] \\
& -\mu \left(\int_{\Omega} N_x N_{xj} dV \hat{u}_j + \int_{\Omega} N_y N_{yj} dV \hat{u}_j + \int_{\Omega} N_z N_{zj} dV \hat{u}_j \right) \\
& + ik_x \left[(\lambda + \mu) \left(2 \int_{\Omega} NN_{xj} dV \hat{u}_j + \int_{\Omega} NN_{yj} dV \hat{v}_j + \int_{\Omega} NN_{wj} \hat{w}_j \right) \right] \\
& + 2\mu ik_x \int_{\Omega} NN_{xj} dV \hat{u}_j \\
& + ik_y \left[(\lambda + \mu) \int_{\Omega} NN_{xj} dV \hat{v}_j + 2\mu \int_{\Omega} NN_{yj} dV \hat{u}_j \right] \\
& + ik_z \left[(\lambda + \mu) \int_{\Omega} NN_{xj} dV \hat{w}_j + 2\mu \int_{\Omega} NN_{zj} dV \hat{u}_j \right] \\
& - k_x^2 \left[(\lambda + \mu) \int_{\Omega} NN_j dV \hat{u}_j + \mu \int_{\Omega} NN_j dV \hat{u}_j \right] \\
& - k_y^2 \mu \int_{\Omega} NN_j dV \hat{u}_j - k_z^2 \mu \int_{\Omega} NN_j dV \hat{u}_j \\
& - k_x k_y (\lambda + \mu) \int_{\Omega} NN_j dV \hat{v}_j - k_x k_z (\lambda + \mu) \int_{\Omega} NN_j dV \hat{w}_j \\
& = -\rho\omega^2 \int_{\Omega} NN_j dV \hat{u}_j
\end{aligned} \tag{2.10}$$

Similarly in the Y-direction,

$$\begin{aligned}
& -(\lambda + \mu) \left[\int_{\Omega} N_y N_{xj} dV \hat{u}_j + \int_{\Omega} N_y N_{yj} dV \hat{v}_j + \int_{\Omega} N_y N_{zj} dV \hat{w}_j \right] \\
& -\mu \left(\int_{\Omega} N_x N_{xj} dV \hat{v}_j + \int_{\Omega} N_y N_{yj} dV \hat{v}_j + \int_{\Omega} N_z N_{zj} dV \hat{v}_j \right) \\
& + ik_x \left[(\lambda + \mu) \int_{\Omega} NN_{yj} dV \hat{u}_j + 2\mu \int_{\Omega} NN_{xj} dV \hat{v}_j \right] \\
& + ik_y \left[(\lambda + \mu) \left(\int_{\Omega} NN_{xj} dV \hat{u}_j + 2 \int_{\Omega} NN_{yj} dV \hat{v}_j + \int_{\Omega} NN_{zj} dV \hat{w}_j \right) \right] \\
& + 2ik_y \mu \int_{\Omega} NN_{yj} dV \hat{v}_j
\end{aligned}$$

$$\begin{aligned}
& + ik_z \left[(\lambda + \mu) \int_{\Omega} NN_{yj} dV \hat{w}_j + 2\mu \int_{\Omega} NN_{zj} dV \hat{v}_j \right] \\
& - k_x^2 \left[\mu \int_{\Omega} NN_{xj} dV \hat{v}_j \right] \\
& - k_y^2 \left[(\lambda + \mu) \int_{\Omega} NN_{yj} dV \hat{v}_j + \mu \int_{\Omega} NN_{yj} dV \hat{v}_j \right] \\
& - k_z^2 \mu \int_{\Omega} NN_{zj} dV \hat{v}_j
\end{aligned} \tag{2.11}$$

and in the Z-directions,

$$\begin{aligned}
& - (\lambda + \mu) \left[\int_{\Omega} N_z N_{xj} dV \hat{u}_j + \int_{\Omega} N_z N_{yj} dV \hat{v}_j + \int_{\Omega} N_z N_{zj} dV \hat{w}_j \right] \\
& - \mu \left(\int_{\Omega} N_x N_{xj} dV \hat{w}_j + \int_{\Omega} N_y N_{yj} dV \hat{w}_j + \int_{\Omega} N_z N_{zj} dV \hat{w}_j \right) \\
& + ik_x \left[(\lambda + \mu) \int_{\Omega} NN_{zj} dV \hat{u}_j + 2\mu \int_{\Omega} NN_{xj} dV \hat{w}_j \right] \\
& + ik_y \left[(\lambda + \mu) \int_{\Omega} NN_{zj} dV \hat{v}_j + 2 \int_{\Omega} NN_{yj} dV \hat{w}_j \right] \\
& + ik_z \left[(\lambda + \mu) \left(\int_{\Omega} NN_{xj} dV \hat{u}_j + 2 \int_{\Omega} NN_{yj} dV \hat{v}_j + \int_{\Omega} NN_{zj} dV \hat{w}_j \right) \right] \\
& + 2\mu ik_z \int_{\Omega} NN_{zj} dV \hat{w}_j - k_x^2 \mu \int_{\Omega} NN_{xj} dV \hat{w}_j - k_y^2 \mu \int_{\Omega} NN_{yj} dV \hat{w}_j \\
& - k_z^2 \left[(\lambda + \mu) \int_{\Omega} NN_{zj} dV \hat{w}_j + \mu \int_{\Omega} NN_{zj} dV \hat{w}_j \right] \\
& - k_x k_z (\lambda + \mu) \int_{\Omega} NN_j dV \hat{u}_j - k_z k_y (\lambda + \mu) \int_{\Omega} NN_j dV \hat{v}_j \\
& = -\rho\omega^2 \int_{\Omega} NN_j dV \hat{w}_j
\end{aligned} \tag{2.12}$$

The above equations (Eq. (2.10), (2.11) and (2.12)) can be arranged in matrix form as below:

$$(\mathbf{K} - \omega^2 \mathbf{M})\mathbf{U} = 0 \tag{2.13}$$

where, \mathbf{K} and \mathbf{M} are global stiffness and mass matrices, respectively, and \mathbf{U} is the assembled displacement vector. We perform eigenvalue analyses on Eq. (2.13) after imposing periodic boundary conditions using Bloch's theorem via Eq. (2.3). Thus,

\mathbf{K} will be a function of wavevector \mathbf{k} , swept across the boundaries of IBZ and corresponding ω 's are calculated.

2.6 Fracture analyses on periodic materials

The failure of structures always poses a serious threat to designers. Advances in the field of fracture mechanics has helped to analyze structures with pre-existing cracks. Linear elastic fracture mechanics (LEFM) have been extensively used to analyze the possible crack propagation and its stability on a structure with pre-existing cracks or flaws. The non-local concepts in LEFM such as stress intensity factor (SIF), energy release rate (ERR), and energy-based criterion for crack propagation guarantee the mesh independency in the solutions. Crack propagations in periodic structures are complex since it involves discontinuity jumps in stress and displacements over the interfaces of different phases in the unit cell [51, 52, 53]. Extended finite element method (XFEM) has proven to be advantageous in simulation cracks in structures with voids or inclusions [54, 55, 56]. The complexity of simulating a crack in a heterogeneous material is that there is a discontinuity in the strain (displacement derivative wrt spatial coordinate) on the inclusion-matrix interfaces in addition to the regular displacement discontinuity on the crack surfaces. Thus to capture both the discontinuities (strong discontinuity in displacement field and weak discontinuity in strain), two different enrichment functions are employed. To calculate the fracture energy in terms of asymptotic displacement and stress fields in a linearly elastic solid, we use stress intensity factor (SIF), e.g., in mode-I fracture, the following expression is used:

$$\sigma_{ij} = \left(\frac{K_I}{\sqrt{2\pi r}} \right) f_{ij}(\theta) \quad (2.14)$$

where, σ_{ij} is the Cauchy stresses, r is the distance from the crack tip, f_{ij} are functions that depends on geometrical parameters. Here, K_I is the SIF. The energy release rate for a crack to grow is given by:

$$G = \frac{\partial U}{\partial a} \quad (2.15)$$

where U is the elastic energy of the system and a is the crack length. For inclusions, on interfaces Γ , the equilibrium condition is taken as a continuous displacement field, i.e., $[[\mathbf{u}]] := \mathbf{u}^{(2)} - \mathbf{u}^{(1)} = \mathbf{0}$ and discontinuous traction field, i.e., $[[\mathbf{t}]] := -(\boldsymbol{\sigma}^{(2)} - \boldsymbol{\sigma}^{(1)}) \mathbf{n}^{(1)}$; superscripts (1) and (2) denote the two sides of the interface Γ . A detailed description of fracture simulation and XFEM implementation is given in chapter 4.

Chapter 3

The Influence of Clamping, Structure Geometry, and Material on Seismic Metamaterial Performance

Diverting and controlling the impact of elastic vibrations upon an infrastructure is a major challenge for seismic hazard mitigation and for the reduction of machine noise and vehicle vibration in the urban environment. Seismic metamaterials (SMs), with their inherent ability to manipulate wave propagation, provide a key route for overcoming the technological hurdles involved in this challenge. This chapter shows engineering the structure of the SM, which serves as a basis to tune and enhance its functionality. Inspired by split rings, swiss rolls, and notch-shaped, and labyrinthine designs of elementary cells in electromagnetic and mechanical metamaterials, we investigate altering the internal geometries of SMs with the aim of creating large bandgaps in a subwavelength regime. Interestingly, clamping an SM to the bedrock creates a zero-frequency stopband, but further effects can be observed in the higher frequency regime due to their specific geometry. We show that square stiff inclusions perform better in comparison to circular ones while keeping the same filling fraction. En route to enhancing the bandgap, we have also studied the performance of SMs with different constituent materials; we find that steel columns, as inclusions, show large bandgaps, however, the columns are too large for steel to be a feasible material in practical or financial terms. Plain concrete would be preferable for industry-level scaling up of the

technology because, concrete is cost-effective, easy to cast directly at the construction site, and easy to provide arbitrary the geometry of the structure. As a part of this study, we show that concrete columns can also be designed to exhibit bandgaps if we cast them within a soft soil coating surrounding the protected area for various civil structures like a bridge, buildings, oil pipelines, etc. Although our motivation is for ground vibration, and we use the frequencies, lengthscales, and material properties relevant to that application, it is notable that we use the equations of linear elasticity, and our investigation is more broadly relevant in solid mechanics.

3.1 Introduction

Controlling elastic waves near structures is key to addressing a large class of civil engineering problems ranging from seismic hazard mitigation to stopping unwanted noise and vibration produced by vehicles, heavy machinery on construction sites, etc. [57, 58, 59, 60]. Seismic waves lead to the destruction of civil installations and loss of life, thus forming one of the most important and difficult challenges for civil engineers; the reduction of urban noise and vibration is also important because they create health issues and have other consequences, such as affecting highly sensitive scientific and medical instruments. There are many other applications, e.g., in the context of ground motions produced from even minor tremors, industrial machinery, or suburban rail transport systems degrading the structural integrity of nearby buildings, pipeline systems, and sensitive instruments; additionally, small-scale damage to structures in petrochemical industries or nuclear reactors can have devastating consequences. Traditional approaches for vibration mitigation, mostly in the form of base isolation (BI) and tuned mass damper (TMDs) have certain limitations [4, 5, 6, 7, 8, 9]: BI induces large movement of the structures which may not be acceptable, TMD works only for a narrow frequency range outside of which it may work adversely which is again a major issue because identifying the frequency contents in the structure correctly is not straightforward as it may change significantly with time due to structural degradation and environmental change [10, 11].

Metamaterials have the capability of manipulating a desired range of frequency components in the propagating wave, an aspect that has been extensively used in electromagnetics, optics, and micro and nano-scale mechanics [61, 62, 63, 64, 65, 66, 67, 68, 69, 70, 71, 72, 73]. However, their large scale extension, which can be extremely useful in solving many of the important engineering problems, mentioned above, requires development. Recent developments have indicated that metamaterials, if designed appropriately, can indeed provide a robust solution for the manipulation of elastic waves, thanks to their ability to create large frequency bandgaps even at large scale [12, 74, 75, 76, 77, 78, 79, 80, 81, 82, 83, 84, 85].

Early work by Economou and Sigalas [86] in 1993 established a global trait that a denser inclusion in the microstructure geometry of periodic media exhibits bandgaps for 2D and 3D structures. This phenomenon is predicted in [87, 25, 88] by using the Floquet-Bloch theory which can be applied to different wave types traveling through a periodic media. Experimentally, Meseguer and Holgado (1999), and Meseguer *et al.* (1999), showed the attenuation of surface elastic waves in a marble quarry containing repetitive circular holes [89]. The bandgaps obtained in the process are in the range of Kilo-Hertz which is not important for seismic applications because seismic forces mostly contain frequencies in the range of few Hertz only [90, 91, 92, 93]. First, full-scale experiments to attenuate surface waves, such as Rayleigh and Love waves, were conducted by Brûlé *et al.* (2014, 2017), in structured soil [12, 78, 94, 67]. The soil was engineered with cylindrically configured voids as inclusions in a periodic manner. This experiment shows the feasibility of using metamaterial at a meter-scale important for civil engineering applications.

A variety of extensions of these concepts are aimed at creating larger bandgaps and forcing these to occur at the low frequencies required for civil engineering applications. Recently, Miniaci *et al.* (2016) [48] numerically analyzed and designed optimal configurations for inclusions of micro-structure geometry, i.e., cross-shaped voids and hollow cylindrical and locally resonant inclusions (e.g., steel, rubber, and concrete), which shield low-frequency contents in seismic forces. Their parametric study on the filling fraction of inclusions in microstructure shows a possibility of enhancing the

bandgap. The ultimate goal of bandgap engineering in this context is to create a zero-frequency bandgap, i.e., one that starts at zero frequency and then extends over a broad range of low frequencies. Achaoui *et. al.* (2017) [95] show that this can be achieved with cylindrical steel inclusions clamped to a bed rock that lies underneath a soil layer; they also considered struts linking the cylindrical steel columns.

Here, we focus on large-scale metamaterials made by periodically installing stiff columns in a matrix-like soil. There are many aspects that are not yet known about such metamaterials, e.g., the effect of structure geometry, that is the detailed geometry within a single building block of the periodic medium, and material constituents. Although the possibility of enhancing the bandgap via varying the substitution ratio of stiffer inclusions is established, the effect of varying the structure geometry and keeping the same filling fraction is yet to be addressed. In the present study, we investigate the effect of the structure geometry in SMs with the aim of creating large band gaps, keeping the volume of inclusions the same. As an illustrative example of the importance of both clamping and structure geometry, we consider, in Figure 3.1, two similar geometries for SMs when they vibrate freely (A,B) and when they are clamped to the bedrock (C,D). We see in Figure 3.1 that just simply tilting some junctions between a cylinder and a bulk medium has a profound impact on stopband width, as noted in earlier studies on phononic crystals consisting of inertial resonators [96, 97, 98]. Interestingly, we find that a torsional mode is associated with the upper edge of the stopband in (A,B), see Figures 2D,H for the case of inertial resonators (IRs) with tilted junctions (also known as ligaments). Such resonance is akin to those studied in chiral elastic metamaterials in a very different range of frequencies [99]. Furthermore, a similar geometrical effect occurs in the higher frequency spectrum when the inclusion is clamped at the bottom. This emphasizes the importance of structure geometry as an additional mechanism to tune higher frequency band spectra of clamped SMs. We also explore the performance of SMs by considering different constituent materials. Specifically, we aim to maximize the bandgap width as well as the number of stopbands since the SMs may have to safeguard different types of civil installations with varied frequency contents ranging from massive tall buildings with

very small natural frequencies to fluid conveyors containing large natural frequencies [100, 101]. Enroute to enhancing the bandgap, we report an innovative design for SM, which is very pertinent to civil engineering practices.

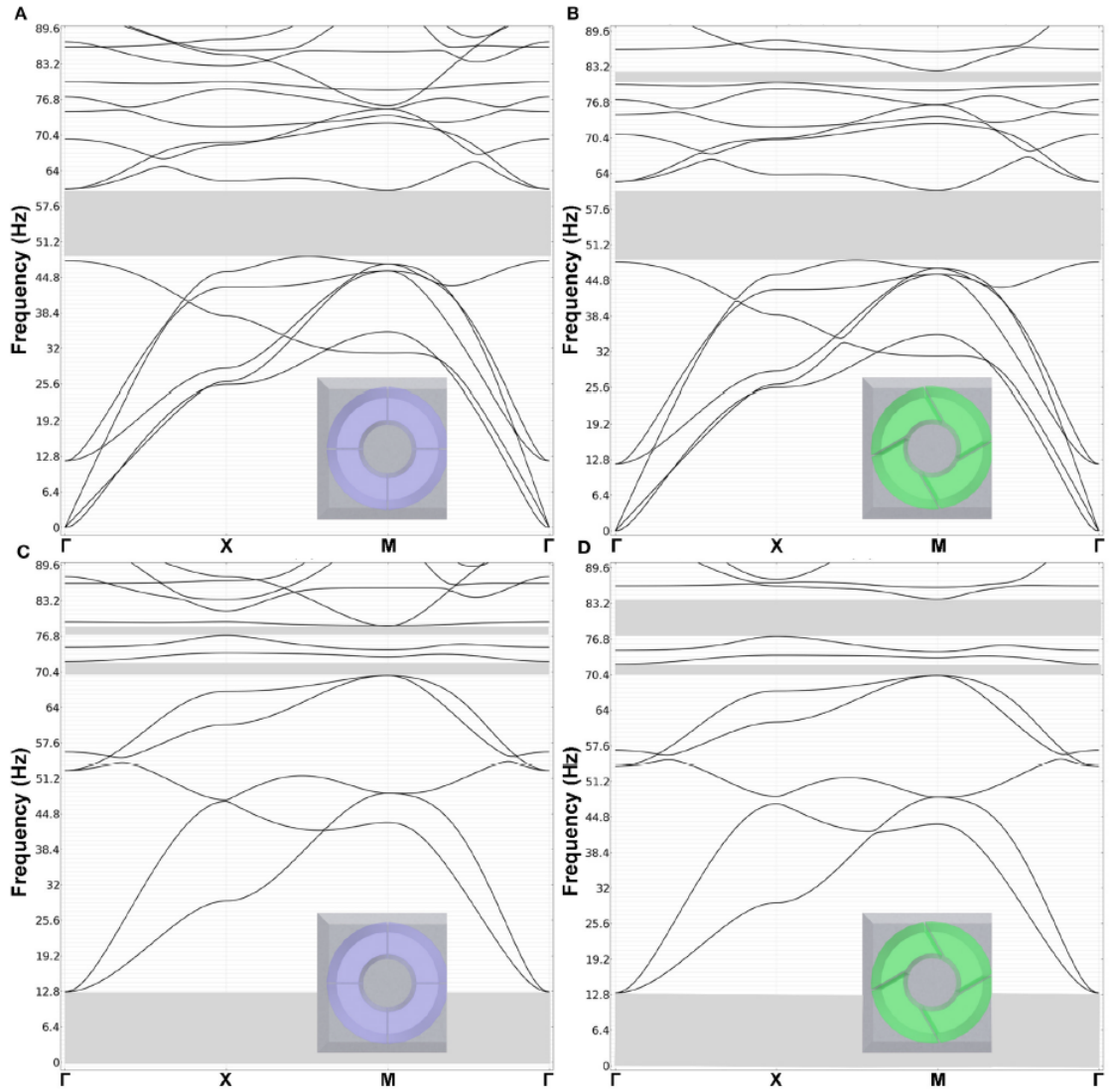


Figure 3.1: Floquet-Bloch band diagrams for cylindrical inclusions obtained for a modulus of Bloch wavevector $|\mathbf{k}|$, that describes the edges of the irreducible Brillouin zone ΓXM .

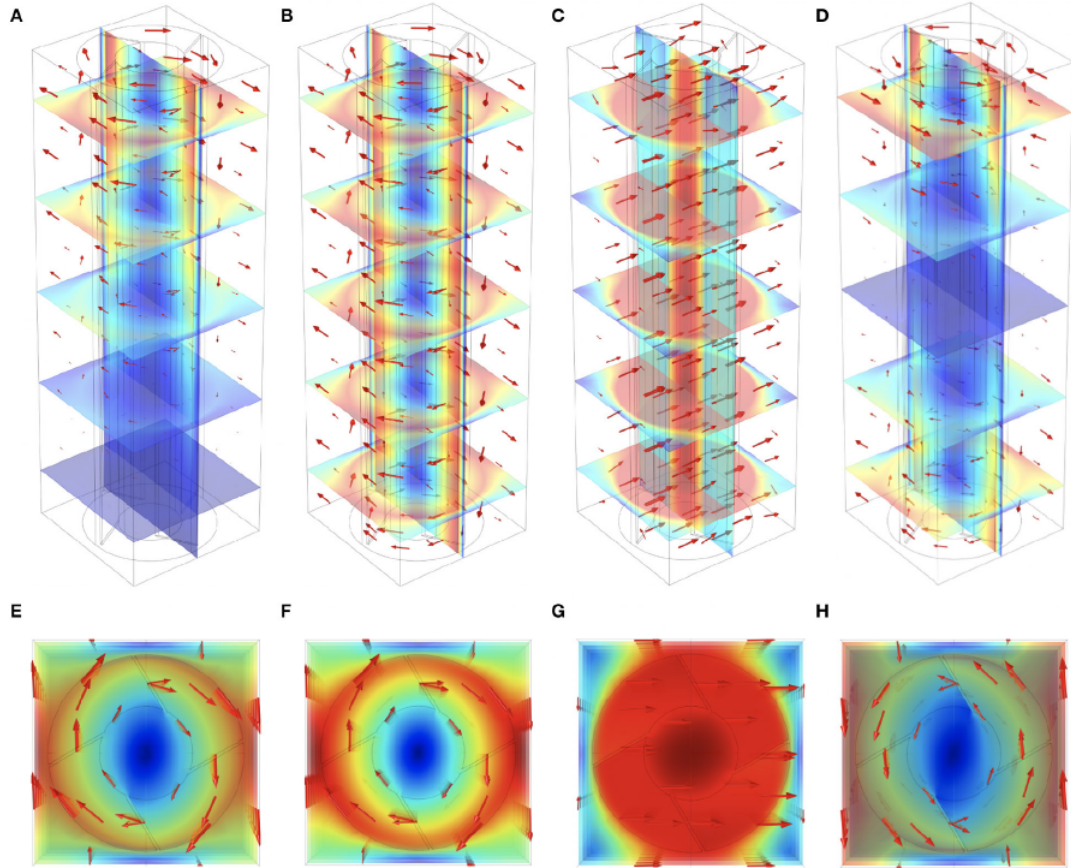


Figure 3.2: Representative eigenmodes for cylindrical inertial resonators (IRs) with four inclined ligaments at high-symmetry point X of the irreducible Brillouin zone ΓXM : (A,E) Rotational mode at 48.5 Hz (IR clamped at bottom, third mode in Figure 3.1D); (B,F) Rotational mode 38.6 Hz (fourth mode in Figure 3.1B); (C,G) Longitudinal mode at 45.8 Hz (sixth mode in Figure 1B); (D,H) Torsional mode at 63.8 Hz (seventh mode in Figure 3.1B).

3.2 Mathematical Formulation-Finite Element Approach

A periodic medium can be analyzed by sequential translational operations performed on its elementary cell, by making use of a lattice vector $\mathbf{a} = (a_1, a_2)$. The inherent periodicity of this cell enables us to characterize the dispersion properties of elastic waves propagating within such a periodic medium, via Bloch's theorem as in Eq. 3.1, where $\mathbf{k} = \{k_x, k_y\}$ is Bloch wavevector and $\mathbf{x} = (x_1, x_2)$ [29]:

$$\phi(\mathbf{x} + \mathbf{a}) = \phi(\mathbf{x})e^{i\mathbf{k}\cdot\mathbf{a}} \quad (3.1)$$

Elastic wave propagation through a linear elastic medium is governed by the elastic Navier equation as given in Eq. 3.2; λ and μ are Lamé's constant, ρ is the density of the elastic medium, and $\{u_i\}_{i=1}^3 = \{u, v, w\}$ represents three components of the displacement field in space. While using Eq. 3.2, a no-slip condition is ensured between the two homogeneous mediums, i.e., relative displacement will be zero between the two mediums.

$$(\lambda + \mu) \frac{\partial^2 u_j}{\partial x_j \partial x_i} + \mu \frac{\partial^2 u_i}{\partial x_j \partial x_j} = \rho \ddot{u}_i \quad (3.2)$$

Rewriting Eq. 3.1 as $u = \tilde{u}(\mathbf{x}, t)e^{i(\mathbf{k}\cdot\mathbf{x} - \omega t)}$, where \mathbf{x} and t represent space and time, and ω is angular frequency, and substituting it in Eq. 3.2, we arrive at Eq. 3.3 by discretizing \tilde{u} in weak form using 3D shape functions in a finite element approach [102]. \mathbf{K} and \mathbf{M} being global stiffness and mass matrices, respectively, which are basically functions of Bloch wavevector \mathbf{k} , and \mathbf{u} is the assembled displacement vector.

$$(\mathbf{K} - \omega^2 \mathbf{M})\mathbf{U} = 0 \quad (3.3)$$

Bloch analyses is conducted by computing dispersion curves via varying $\mathbf{k} = \{k_x, k_y\}$ along the edges of irreducible Brillouin zone (IBZ). For a square lattice, IBZ lies along the edges of the triangle ΓMX ; $\Gamma = (0, 0)$, $M = (\frac{\pi}{a}, \frac{\pi}{a})$ and $X = (\frac{\pi}{a}, 0)$, where $a = a_1 = a_2$. For a real valued \mathbf{k} , the frequencies (ω) are obtained by solving an appropriate eigenvalue problem, thereby constructing the dispersion curves via plotting real valued frequencies corresponding to \mathbf{k} [103, 104]. Since dispersion curves are computed over a medium representing an infinite array of micro-structured geometry, they alone do not fully reveal the inherent effectiveness of SM design. For this purpose, transmission spectra is also computed, which is a measure of wave propagation attenuation/transmission losses over a finite medium [105].

3.3 Results and Discussion

In this section, we present dispersion curves and transmission losses for different microstructure geometries. We have already illustrated the importance of microstructure geometry with cylindrical inertial resonators that make possible a torsional mode associated with a large stopband of around 50 Hz when IRs are freely vibrating, see Figures 3.1B, 3.2D,H in section 3.1. Clamping IRs to the bedrock suppresses all ground vibrations below 13 Hz but prevents the appearance of the torsional mode, so the stopband at 50 Hz disappears. We further note that tilting the ligaments of IRs of both the freely vibrating (Figure 3.1B) and clamped (Figure 3.1D) cases, opens a high-frequency stopband around 83 Hz. Depending upon applications (e.g., earthquake protection which is mostly in the 0–10 Hz range, or, for instance, suppression of ground vibration due to the car and railway traffic, which is concerned with higher frequencies), civil engineers might focus on clamping to bedrock, or on micro-structure geometry, of SMs. Thus, there is certainly a trade-off between micro-structure geometry and clamping that needs to be taken into account in the design of clamped SMs in order to achieve optimal performance in a range of frequencies of interest. To the best of our knowledge, this has never been studied before, and this is the main scope of the present section. To arrive at a microstructure that maximizes the bandgap (with or without clamping), we compare different results keeping the substitution ratio the same. Having arrived at a particular configuration, we explore the effect of changes in orientation of the inclusion from 0 to 45°. After this, we move to the aspect of material constituents for inclusion, and we also focus on cost-effectiveness and ease of fabrication of arbitrary microstructure geometry.

3.3.1 Comparison of different geometry of inclusions

Basic civil engineering infrastructures are constructed on medium to dense soil for their obvious stability purposes. Satisfying this, realistic soil conditions are adopted in present work, i.e., medium soil with parameters as Elastic modulus, $E = 153$ MPa, Poisson's ratio, $\mu = 0.3$ and density, $\rho = 1800$ kg/m³. Micro-structure of the peri-

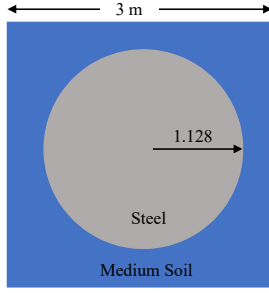
odic media is configured with steel columns as inclusions in three forms having same substitution ratio as shown in Fig. 3.3.

- Cylindrical steel column of height 10 m and circular cross-section of radius 1.128 m.
- Regular sized square steel column of same height, i.e., 10 m. The cross-section of regular sized square is taken as 2 m \times 2 m.
- Notch-shaped square steel column again with same height, i.e., 10 m. 0.4 m \times 0.6 m notch is provided in a square of 2.25 m size as shown in Fig. 3.3(e).

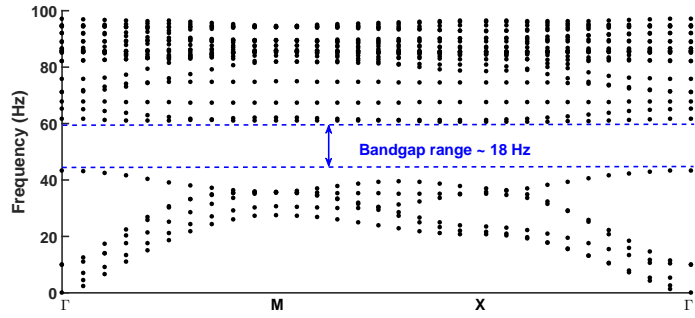
Each form of inclusion is embedded in an unstructured medium soil matrix (3 m \times 3 m \times 10 m) so as to form a microstructure of the periodic media; top and bottom of the microstructure remain unclamped. Elastic properties of steel is chosen as $E = 200$ GPa, Poisson's ratio, $\mu = 0.33$ and density, $\rho = 7850$ kg/m³. We have also used soft clay models (which will be seen subsequently) to study their effect on bandgap enhancement. A comparison of its dispersion properties, obtained along the edges of the irreducible Brillouin zone ΓMX , can be made from Fig. 3.3. Bandgaps are obtained in all the configurations, i.e., microstructure with inclusions having circular, regular square, and notch-shaped square cross-sections. The square cross-section inclusions show a higher range of bandgap (approximately 28 Hz and 34 Hz in regular and notch-shaped, respectively) in comparison to circular cross-section inclusion (approximately 18 Hz) for the same substitution ratio of steel.

A comparison of stop-bands for these configurations is also obtained (see Fig. 3.5), by clamping the bottom of the microstructure. Here, the column inclusions with circular cross-sections show a better stop-band (approximately 15 Hz) in contrast to regular square-shaped inclusions (approximately 7.62 Hz). However, the notch-shaped square inclusion shows a slightly higher stop-band (approximately 17 Hz) to that of the circular cross-section for the same substitution ratio of steel inclusion. Along with stop-band, bandgap at a higher frequency range is also observed for all three forms of inclusions. The circular cross-section shows a higher bandgap of around 21

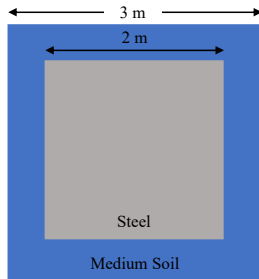
Hz in comparison to regular square-shaped cross-section which has only about 3.3 Hz. The notch-shaped square cross-section shows a slightly higher range of bandgap, approximately 21.75 Hz (7.85 Hz + 14 Hz), than the circular cross-sectioned inclusion. However, the bandgaps in circular and notch-shaped inclusions are positioned at a higher frequency spectrum, which is less important for engineering applications.



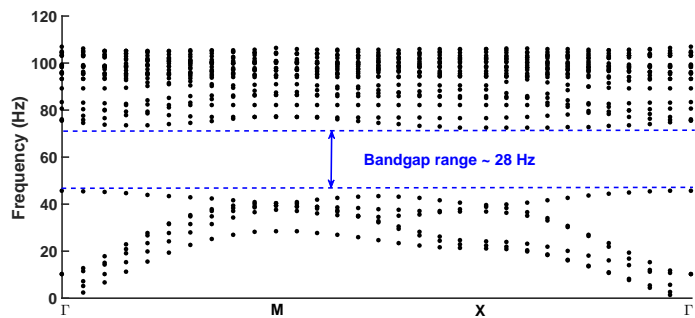
(a) Cross-section of cylindrical steel inclusion with 0.445 substitution ratio



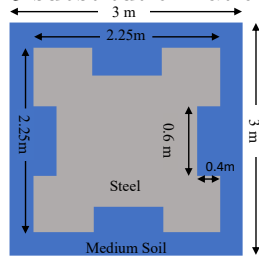
(b) Dispersion curves for cylindrical inclusion



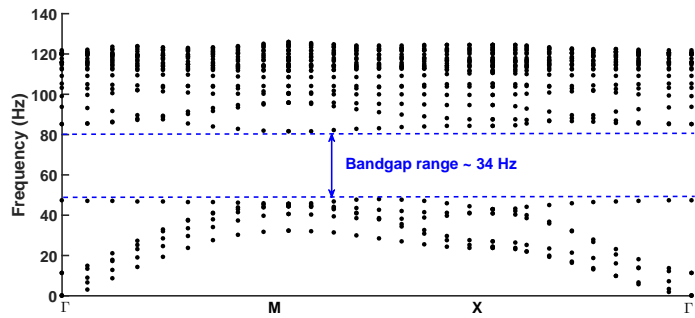
(c) Cross-section of regular square steel inclusion with 0.445 substitution ratio



(d) Dispersion curves for square inclusion

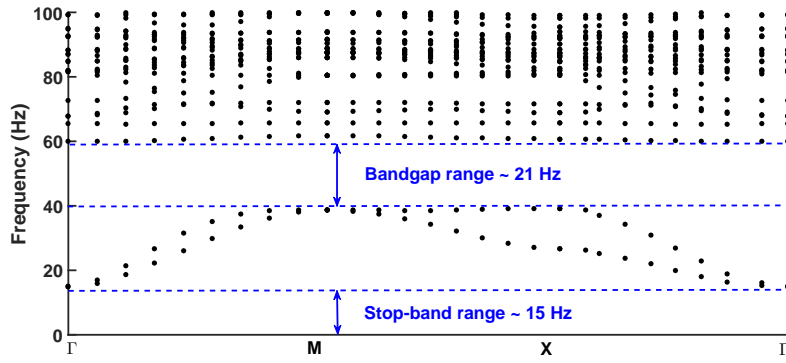


(e) Cross-section of notch-shaped square steel inclusion with 0.445 substitution ratio

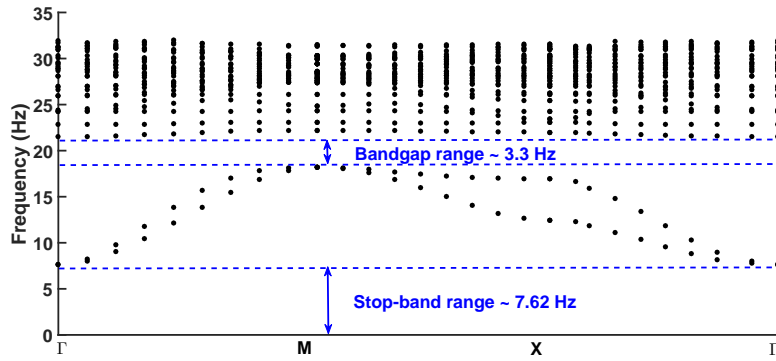


(f) Dispersion curves for notch-shaped square inclusion

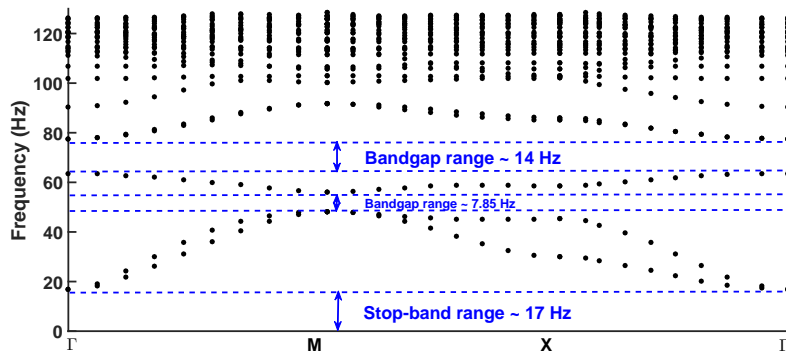
Figure 3.3: Unclamped configuration of (a) cylindrical, (c) regular-shaped square, and (e) notch-shaped square geometry inclusions in the elementary cell of periodic media (medium soil) with equal substitution ratio (0.445) and their corresponding dispersion curves (b,d,f)



(a) Dispersion curves for circular cross-section with 1.128 m radius as shown in figure 3.3(a)

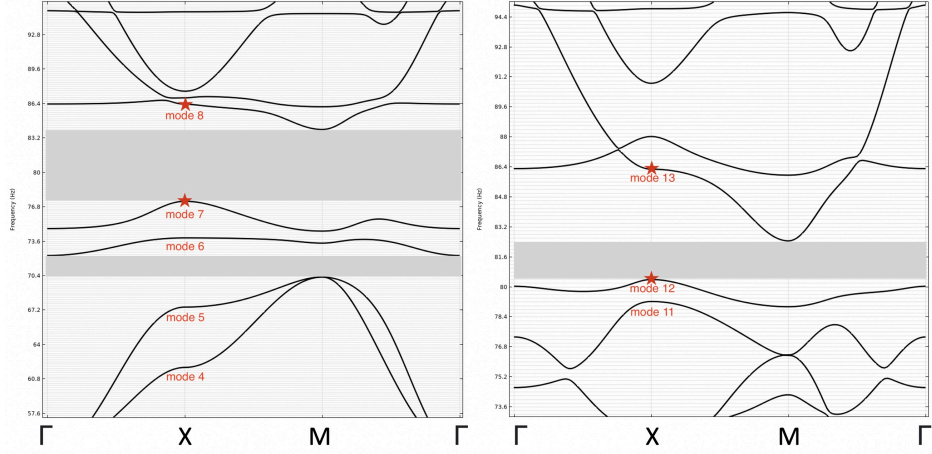


(b) Dispersion curves for a regular-shaped square cross-section of side length 2 m as shown in figure 3.3(c)

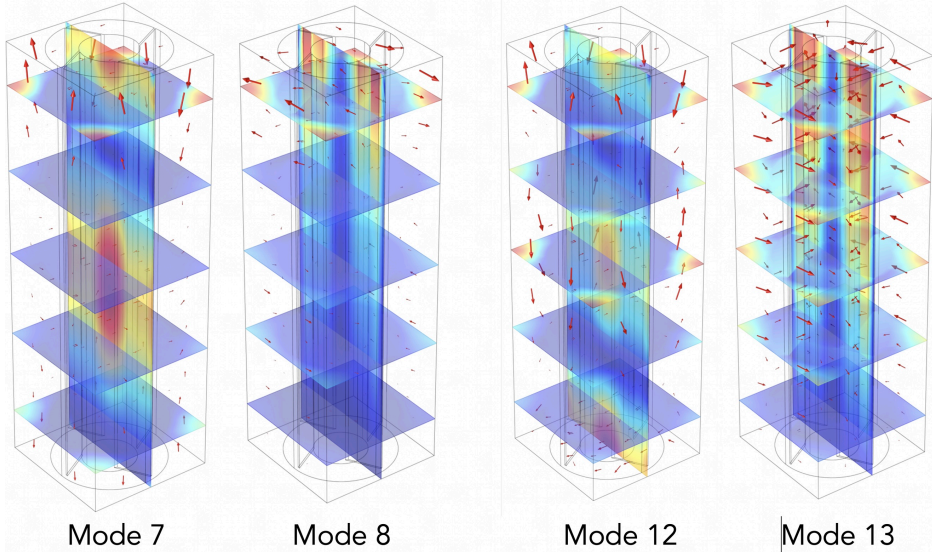


(c) Dispersion curves for notch-shaped square cross-section (four notches of dimension 0.6 m \times 0.4 m in a 2 m square as shown in figure 3.3(e))

Figure 3.4: Dispersion curves for clamped configuration of geometries shown in fig. 3.3 with substitution ratio 0.445.



(a) Dispersion curves for cylindrical inclusions for clamped (left) and unclamped (right) with 4 inclined ligaments.



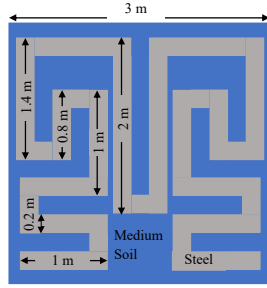
(b) Representative eigenmodes for cylindrical inertial resonators (IRs) with 4 inclined ligaments at high-symmetry point X of the irreducible Brillouin zone ΓXM corresponding to the star points in Fig.3.5 a: 7th and 12th modes are longitudinal, 8th is torsional and 13 rotational.

Figure 3.5: Dispersion curves and eigen modes of cylindrical inclusions for clamped and unclamped configurations.

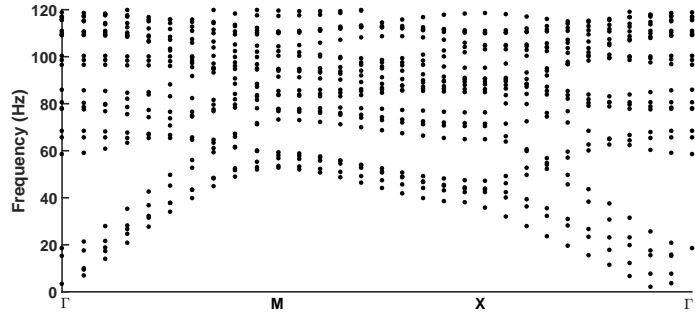
Other investigated microstructure geometries are coil/Labyrinthine (complex sheet piling type of inclusion), split ring-like and swiss roll-like cylindrical steel inclusions in medium soil (see Fig. 3.6 and 3.7). The same substitution ratio, i.e., 0.445 was considered in the former two microstructures, whereas the swiss roll-like inclusion is considered with a diameter equal to solid circular inclusion as in Fig. 3.3, i.e.,

1.128 m with a substitution ratio of 0.15. Notably, in medium soil, without clamping the bottom, split-ring-like inclusion with 4 gaps shows a band gap of approximately 10.6 Hz, whereas the Labyrinthine inclusion shows no bandgap. Testing with another material constituent for Labyrinthine inclusion (Fig. 3.6(a)), i.e., with rubber and concrete, no bandgap was observed (see Fig. 3.8). On the other hand, a split-ring with 2 gaps shows an enhanced bandgap (12 Hz in the range of 46.84 Hz- 59.23 Hz) as compared to 4 gap split-ring (10.6 Hz in the range of 48.53 Hz- 58.35 Hz) with same substitution ratio (0.445). Dispersion curves for swiss roll-like steel inclusion with different thickness, i.e., 0.128 m and 0.03 m in medium soil (3 m × 3 m × 10 m) is obtained by without clamping the bottom and is shown in Fig. 3.7. Clearly, there is no bandgap for these configurations. The stop-bands for configurations in Fig. 3.6 and 3.7 are obtained by clamping the bottom and is shown in Fig. 3.9. It is observed that Labyrinthine inclusion gives a higher stop-band in contrast to the other two, i.e., 14.7 Hz for Labyrinthine steel inclusion in comparison to 12.7 Hz and 11 Hz in split-ring and swiss-roll-like steel inclusions.

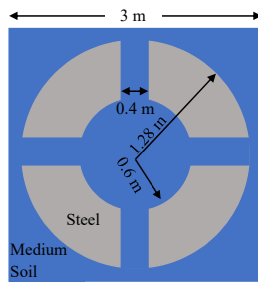
Investigating with different soil properties, i.e., with soft soil having properties $E = 96.5$ MPa, $\mu = 0.33$ and $\rho = 1650$ kg/m³ and very soft soil type 1 with properties $E = 10$ MPa, $\mu = 0.25$ and $\rho = 1400$ kg/m³, Labyrinthine and 2 gap split ring-like steel inclusion shows an improvement on bandgaps obtained via dispersion curves in Fig. 3.6. Labyrinthine steel inclusion shows a bandgap of 6 Hz in the range of 38 Hz - 44 Hz in soft soil (Fig. 3.10(a)) in contrast to medium soil (Fig. 3.6(b)), which shows no bandgap. Split ring with 2 gaps shows an enhanced bandgap (approx. 17 Hz) in soft soil with soil properties $E = 96.5$ MPa, $\mu = 0.33$ and $\rho = 1650$ kg/m³ (Fig. 3.10(b)). The bandgap is also obtained in a lower region than that obtained in the medium soil (Fig. 3.6(f)). On further exploring soil properties, 2 gap split ring shows an excellent improvement over the bandgap in a very soft soil type 2 with soil properties $E = 5$ MPa, $\mu = 0.35$ and $\rho = 1633$ kg/m³. A bandgap of 5 Hz is obtained at a much lower region (approx. 8 Hz - 13 Hz) in very soft soil type 2 for 2 gap split ring (Fig. 3.10(c)). Finally, we investigated a typical configuration such as a triphasic inclusion as shown in Fig. 3.11 [106].



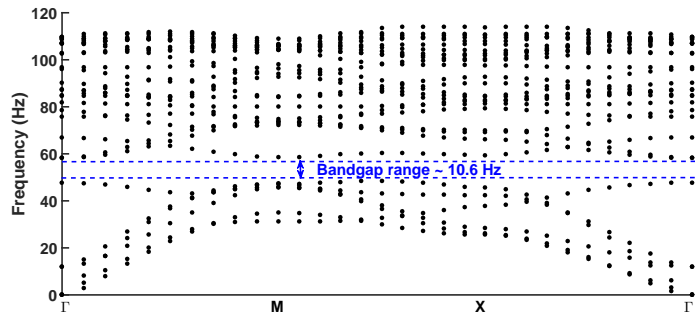
(a) Cross-section of cylindrical coil/Labyrinthine inclusion with substitution ratio 0.445



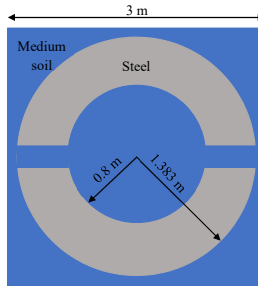
(b) Dispersion curves for cylindrical coil/Labyrinthine inclusion



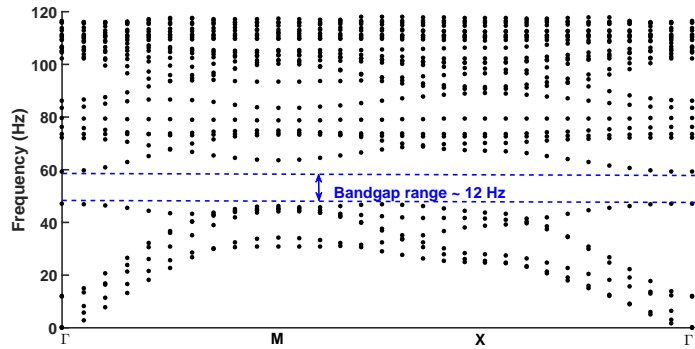
(c) Cross-section of 4 gaps cylindrical split-ring inclusion with substitution ratio 0.445



(d) Dispersion curves for 4 gaps cylindrical split-ring inclusion

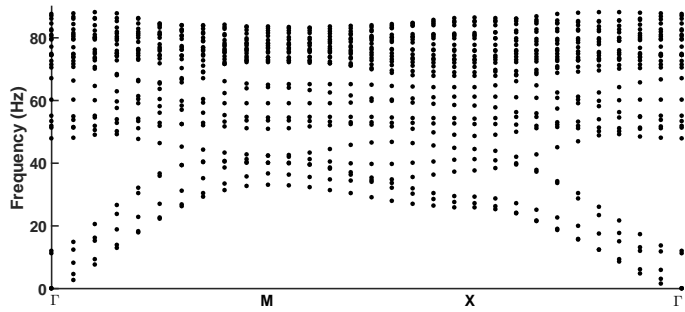
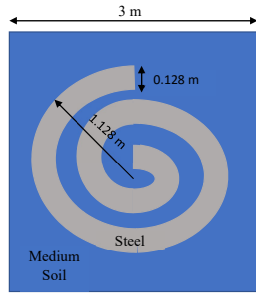


(e) Cross-section of 2 gaps cylindrical split-ring inclusion with substitution ratio 0.445

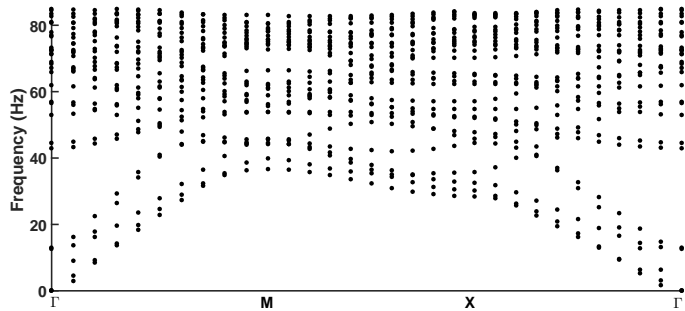
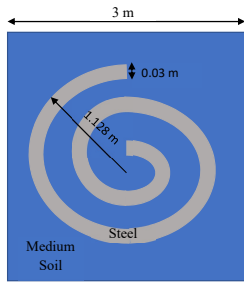


(f) Dispersion curves for 2 gaps cylindrical split-ring inclusion

Figure 3.6: Unclamped configuration of (a) coil/Labyrinthine, (c) 4 gaps split-ring and (e) 2 gaps split-ring with steel as an inclusion with substitution ratio 0.445 in medium soil matrix and corresponding dispersion curves (b, d, f).

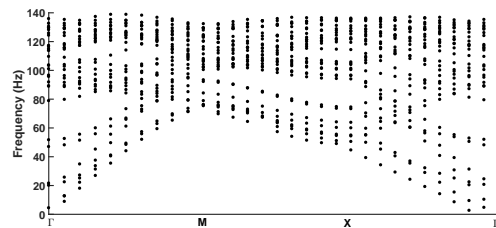
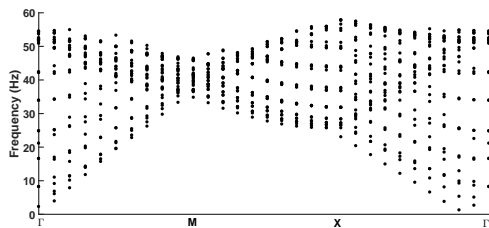


(a) Cross-section of cylindrical swiss roll-like inclusion with thickness 0.128 m (b) Dispersion curves for cylindrical swiss roll inclusion with thickness 0.128 m



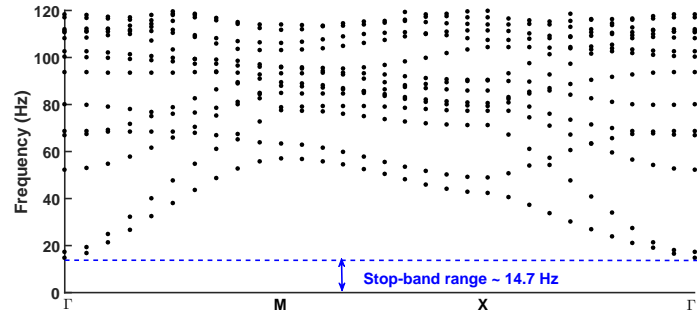
(c) Cross-section of cylindrical swiss roll inclusion with thickness 0.03 m (d) Dispersion curves for cylindrical swiss roll-like inclusion with thickness 0.03 m

Figure 3.7: Unclamped configuration of cylindrical swiss roll like geometry with different thickness of steel inclusions in medium soil matrix. Diameter of swiss roll is considered same as solid circular inclusions in Fig. 3.3.

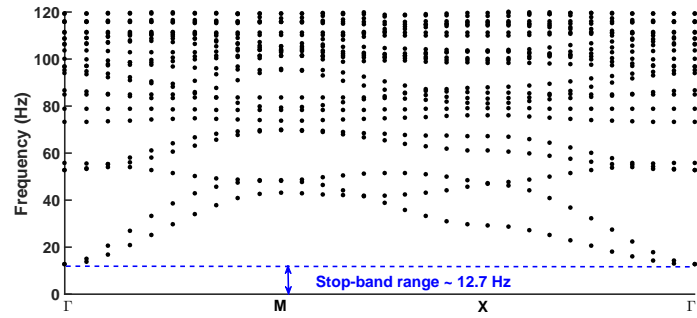


(a) Dispersion curve for Labyrinthine microstructure with rubber as inclusion (b) Dispersion curve for Labyrinthine microstructure with concrete as inclusion

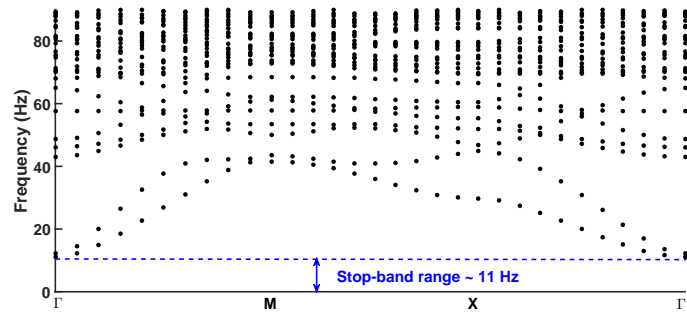
Figure 3.8: Dispersion curves for unclamped configuration of Labyrinthine geometry as shown in fig. 3.6(a) with different constituent material, i.e., (a) rubber and (b) concrete.



(a) Dispersion curves for cylindrical Labyrinthine inclusion

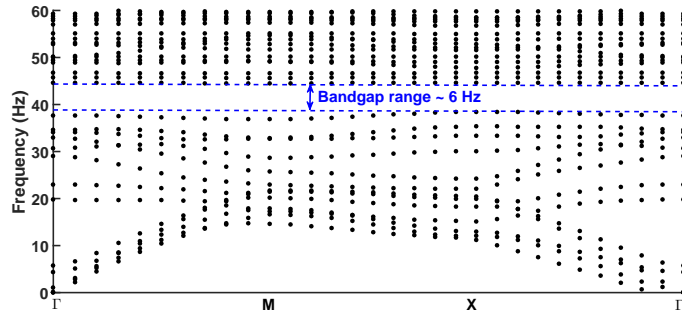


(b) Dispersion curves for cylindrical split-ring-like inclusion

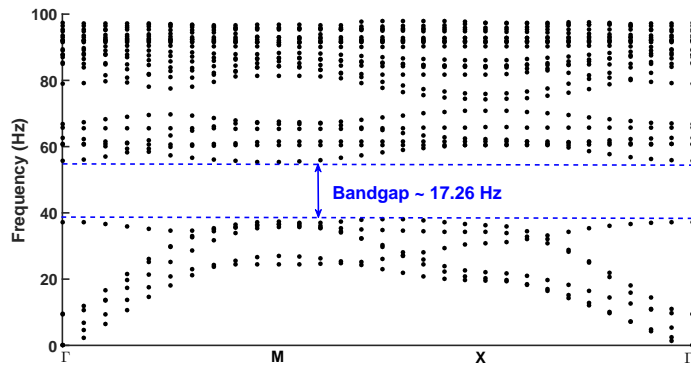


(c) Dispersion curves for cylindrical swiss-roll-like inclusion

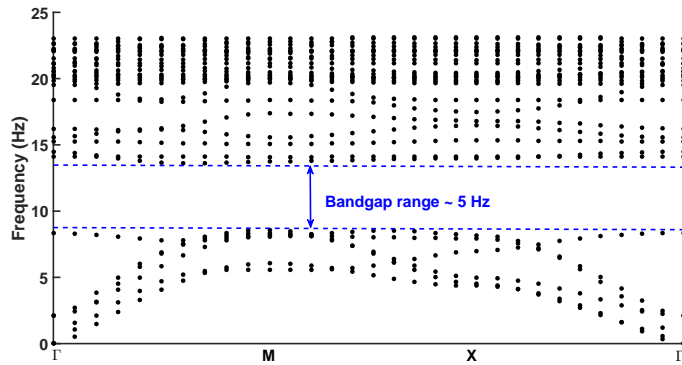
Figure 3.9: Dispersion curves for clamped configuration with steel as inclusion material for (a) Labyrinthine, (b) 4 gaps split ring, and (c) swiss roll with 0.128 m thickness with substitution ratio as 0.445 (for swiss roll: 0.15).



(a) Dispersion curves for cylindrical Labyrinthine inclusion in very soft clay type 1 (cross-section details in Fig. 3.6(a))



(b) Dispersion curves for 2 gap cylindrical split-ring-like inclusion in soft soil (cross-section details in Fig. 3.6(e))



(c) Dispersion curves for 2 gap cylindrical split-ring-like inclusion in very soft clay type 2 (cross-section details in Fig. 3.6(e))

Figure 3.10: Dispersion curves for unclamped configurations of Labyrinthine and 2 gap split ring steel inclusions with 0.445 substitution ratio in soft, very soft clay type 1 and very soft clay type 2.

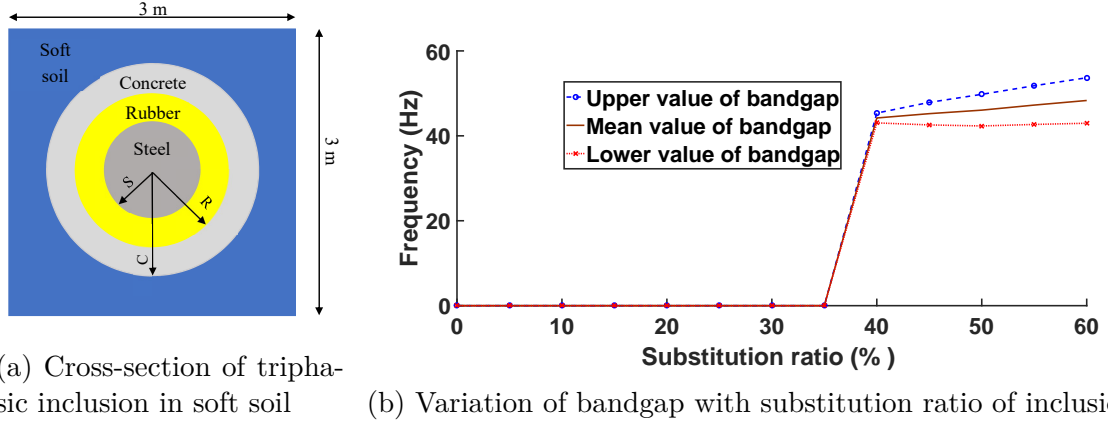


Figure 3.11: Unclamped configuration (all three type of inclusion, i.e., concrete, rubber and steel), and Variation of bandgap width versus substitution ratio of triphasic inclusion in soft soil.

A circular cylinder of steel, surrounded by a thick rubber shell, surrounded by a concrete outer shell within a bulk of soft soil with parameters $E = 96.5$ MPa, $\mu = 0.33$ and $\rho = 1650$ kg/m³ as shown in Fig. 3.11(a). The ratio of the radius of each inclusion material is taken such as $\frac{S}{R} = \frac{R}{C} = 0.83$, where S, R, and C denote the radius of steel, rubber and concrete, respectively. The dimension of the unit cell is 3 m \times 3 m \times 10 m. With increasing substitution ratio of material constituents, the varying bandgap width is plotted as shown in fig. 3.11(b). It can be seen that the band gap for triphasic inclusion appears at lower substitution rates than for monophasic substitution cases. For convenience, we summarize the geometry and elastic properties of the microstructures in the following tables.

Table 3.1: Geometry of the microstructures of seismic metamaterial

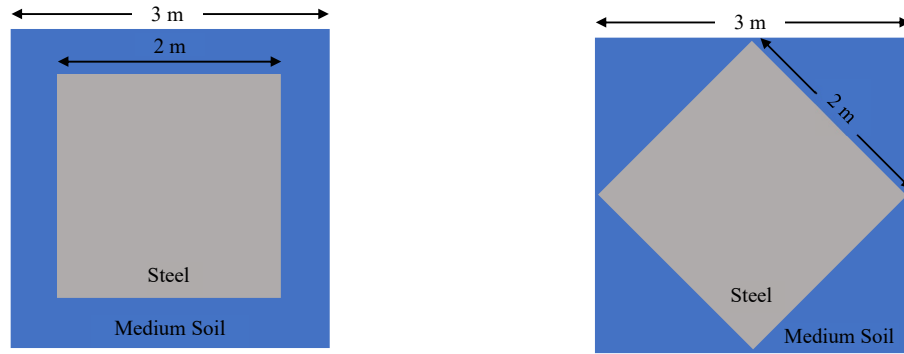
Types	Width/thickness (m)	Length (m)	Diameter (m)	Substitution ratio
Medium soil	3	3	-	-
Loose soil	3	3	-	-
Regular shaped square inclusion	2	2	-	0.445
Notch shaped square inclusion	2.25	2.25	-	0.445
Labyrinthine like inclusion	0.2	7	-	0.445
4 gap split ring inclusion	-	-	Outer 1.3 Inner 0.62	0.445
2 gap split ring inclusion	-	-	Outer 1.423 Inner 0.84	0.445

Table 3.2: Material properties used in the design of seismic metamaterial

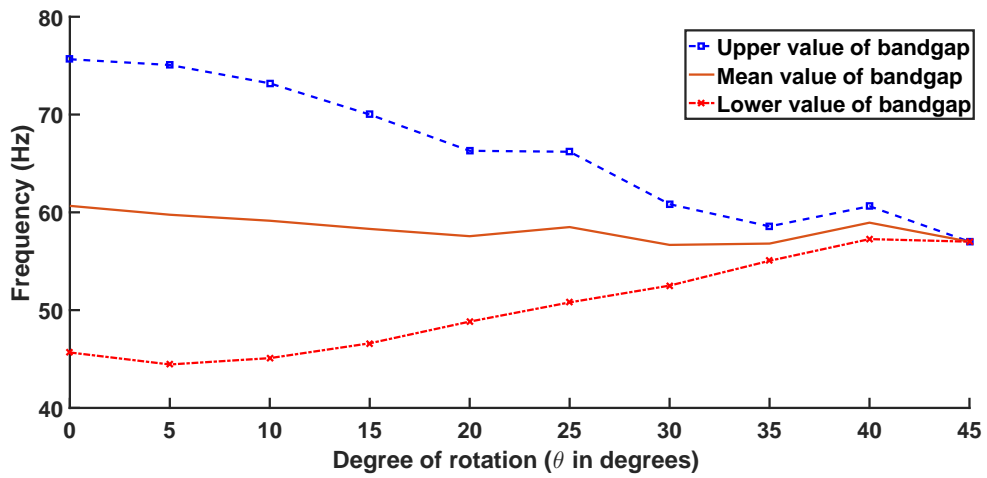
Material	Elastic modulus (MPa)	Poisson's ratio	Density (kg/m ³)
Medium soil	153	0.3	1800
Soft soil	96.5	0.33	1650
Very soft clay type 1	10	0.25	1400
Very soft clay type 2	5	0.35	1633
Steel	2×10^5	0.33	7850
Concrete	3.5×10^4	0.15	2400

3.3.2 Effect of varying orientation in square inclusions

Verifying in subsection [3.3.1](#), that square geometry as inclusions perform better, here we explore the effect of varying its orientation within the microstructure of periodic media by rotating the same from 0° to 45° . With this exercise, we further explore the microstructure geometries towards achieving higher bandgaps. Steel inclusion is considered as column with regular-shaped square geometry ($2 \text{ m} \times 2 \text{ m} \times 10 \text{ m}$) within an unstructured medium soil ($3 \text{ m} \times 3 \text{ m} \times 10 \text{ m}$), with properties same as in section [3.3.1](#). The orientation of square inclusion is made to vary from 0° to 45° , in increments of 5° . Fig. [3.12\(c\)](#) shows the plot for bandgaps obtained from varying the orientation of inclusion plotted against the angle. Interestingly, the plot shows a declining trend for the bandgap with increase in angle, starting from 28 Hz at 0° to 0 Hz at 45° . Thus, we summarize that a square inclusion oriented at 0° gives a wider bandgap in comparison to other orientations when examined with same substitution ratio. To further investigate the efficacy of the design, transmission losses (see Fig. [3.13](#)) are computed over a finite array of SM design consisting of five square steel columns (oriented at 0° and 45° , respectively). For the computation, Rayleigh wave is incident normally as a line source. With 0° orientation a dip is observed in the range of 58 Hz-82 Hz, which shows possible large wave attenuation/transmission loss, whereas no such observations is made for the 45° case.



(a) Cross-section of 0° orientation of square inclusion with 0.445 substitution ratio (b) Cross-section of 45° orientation of square inclusion with 0.445 substitution ratio



(c) Bandgap for unclamped configuration versus orientation angle (degree) plot for square inclusion (steel) in medium soil at same substitution ratio, i.e., 0.445

Figure 3.12: Effect of change in orientation angle (in degrees) of unclamped regular-shaped square steel inclusion with 0.445 substitution ratio in medium soil on bandgap;

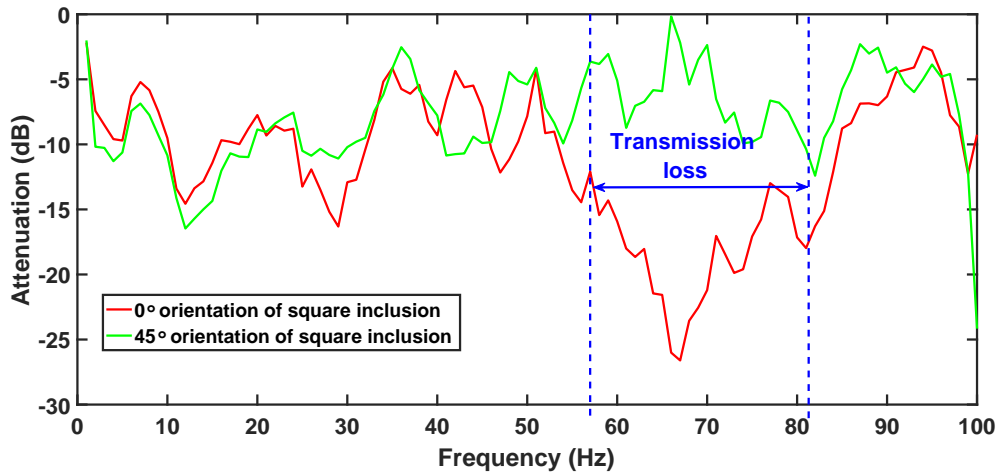


Figure 3.13: Transmission loss for 0° and 45° oriented square steel inclusion in medium soil matrix (bottom remains unclamped).

3.3.3 Feasibility of inclusion material

So far we have discussed about the geometry of the inclusions within the unit cell, so as to generate a wide bandgap and its positioning in the frequency spectrum. However, we have exclusively utilized steel as its constituent material for the purpose. But it is not feasible, both economically and technically, to generate such a large volume of steel having dimensions $2 \text{ m} \times 2 \text{ m} \times 10 \text{ m}$ making up a volume of 40 m^3 and give them complex cross-section geometry via standard industrial fabrication processes. Conversely, concrete having an advantage over steel, in terms of fire and corrosion resistance, low density, resistant to impact of high groundwater level and other on-field applications like easily mouldable into desired shapes, makes it a better choice within civil engineering domain. Noting this fact, we compared the dispersion properties of concrete inclusions (M50 grade) with that of steel inclusions (Figs. 3.3(d) and 3.14(b)); both having same substitution ratio (0.445) and embedded in medium soil whose geometry and elastic properties are same as in section 3.3.1. The elastic properties of M50 grade concrete is taken as $E = 35.35 \text{ GPa}$, Poisson's ratio, $\mu = 0.15$ and density, $\rho = 2400 \text{ kg/m}^3$. Unfortunately, concrete inclusions in medium soil matrix shows no bandgap frequencies (Fig. 3.14(b)). However, as discussed earlier, concrete

being an ideal choice for most of the civil installations, we performed a parametric study with different grades of concrete combined with soft, medium and dense soil. In the process, we arrive at a design of SM having M50 grade concrete inclusion in very soft soil type 1 (soil properties is taken as $E = 10$ MPa, Poisson's ratio, $\mu = 0.25$ and density, $\rho = 1400$ kg/m³), showing a bandgap of approximately 3.91 Hz in the range of 18.45 Hz-22.36 Hz (Fig. 3.14(d)). Transmission loss are computed using a finite strip of five concrete square columns in very soft soil type 1 which shows large Rayleigh wave attenuation in range of 15 Hz- 25 Hz, in comparison to medium soil (Fig. 3.15). Zero frequency stop-band computation (see Fig. 3.16) distinctly shows two bandgaps; ultra-low stop-band frequency (0-7.62 Hz) and a higher range of bandgap, approximately 3.28 Hz (range 18.72 Hz-22 Hz). Transmission loss for 0° oriented regular-shaped square concrete columns in very soft soil type 1 ($E = 10$ MPa, $\mu = 0.25$ and $\rho = 1400$ kg/m³) and medium ($E = 153$ MPa, $\mu = 0.3$ and $\rho = 1800$ kg/m³) soil matrix is also computed over a finite array of the design region (see Fig. 3.17). Clearly, concrete columns in soft soil type 1 attenuate the Rayleigh wave vibrations to a larger extent in comparison to medium soil matrix in stop-band.

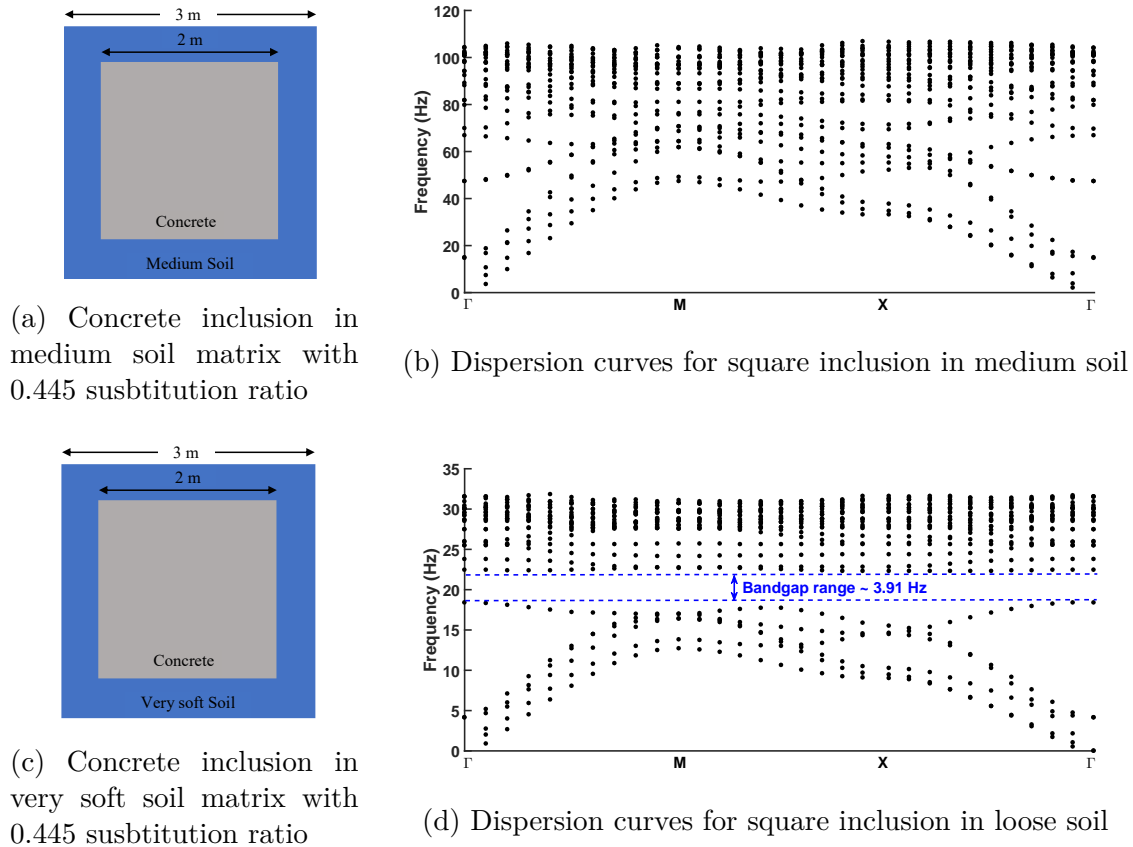


Figure 3.14: Unclamped configuration of concrete inclusion (with 0.445 substitution ratio) in (a) medium soil; (c) very soft soil and corresponding dispersion curves (b,d).

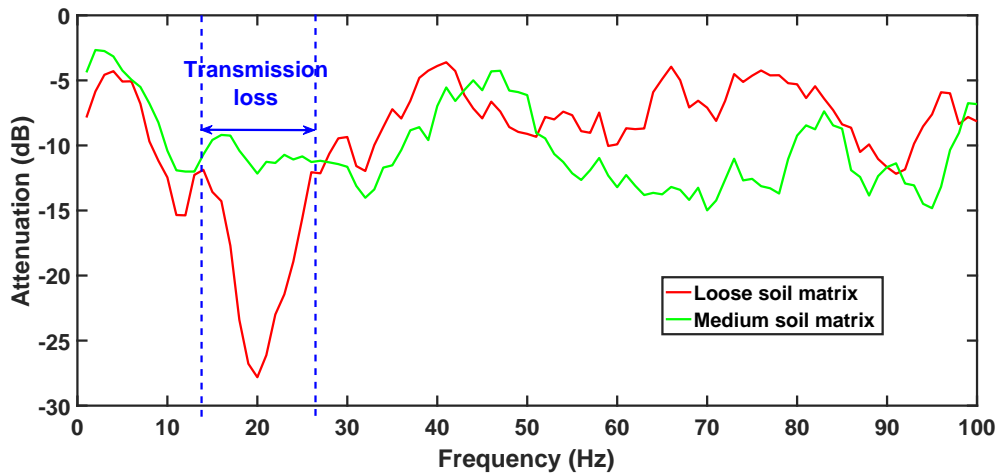


Figure 3.15: Transmission losses for unclamped concrete inclusions in very soft soil type 1 and medium soil matrix corresponding to Fig. 3.14.

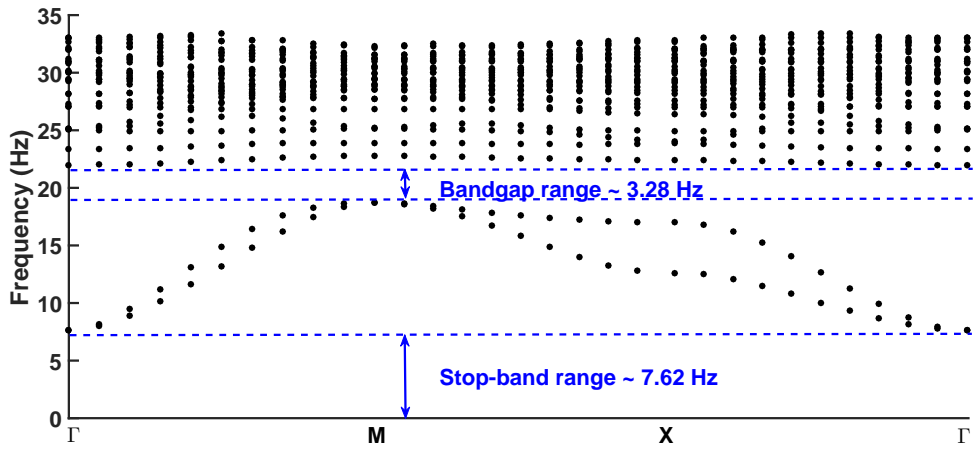


Figure 3.16: Dispersion curve for clamped configuration of M50 grade square concrete columns in soft soil matrix.

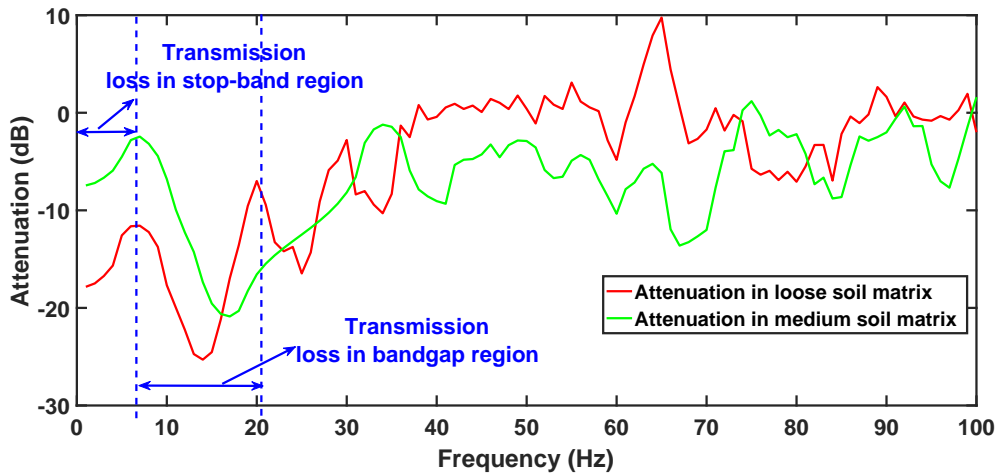


Figure 3.17: Attenuation for clamped configuration of square concrete columns in soft soil type 1 and medium soil matrix.

As mentioned earlier, since loose soil is not suitable for construction purposes, we recommend the following architecture. As shown in Fig. 3.18, for a finite region to be protected (denoted with A in Fig. 3.18), the SM microstructure should be designed using square inclusions of concrete columns oriented at 0° in a narrow strip of very soft soil matrix in Fig. 3.18, leaving the residual region in its natural/structured state, making civil constructions possible on the residual region. Another aspect is that since

the civil installations within the protected region may vary largely, with varied natural frequency ranges and importance, concrete columns of such a high dimension may not be necessary always. For the same, a parametric study on obtaining stop-bands with different concrete sizes is performed and the results are shown in Fig. 3.19. The effect of variation of stop-band follows a linear trend with increasing substitution ratio of regular-shaped square concrete columns. Such graphs can be used for calibration purpose for optimal SM design.

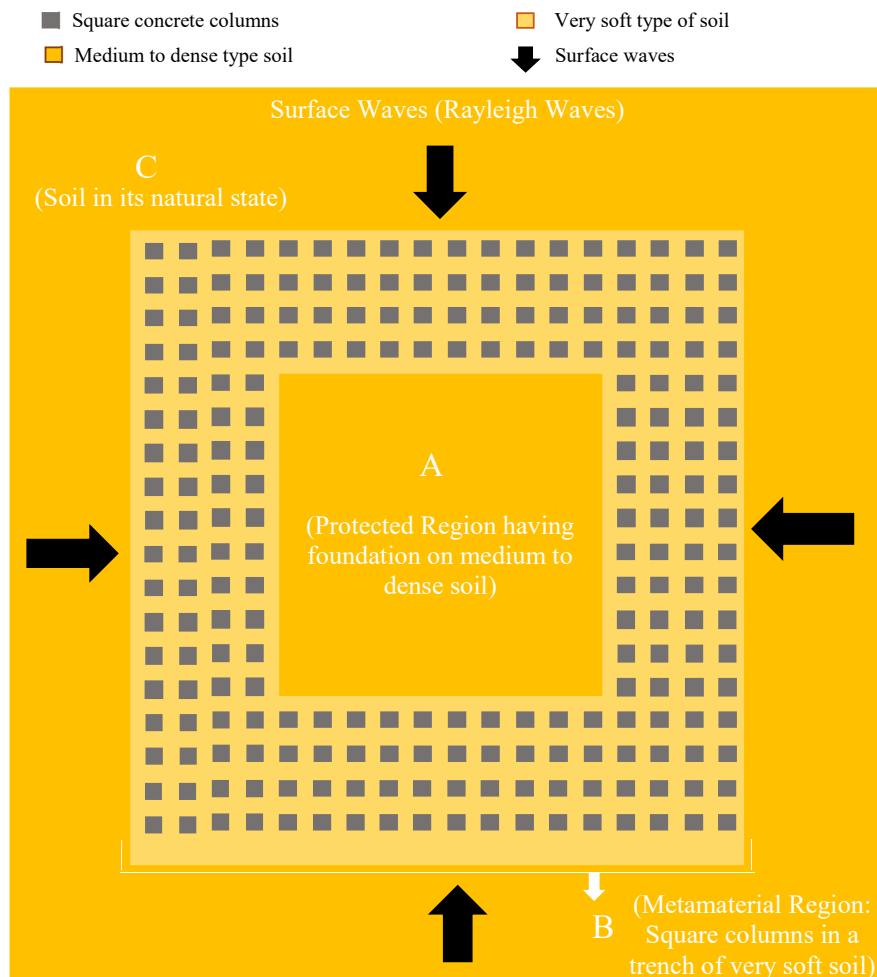


Figure 3.18: Schematic representation of the proposed design for metamaterial.

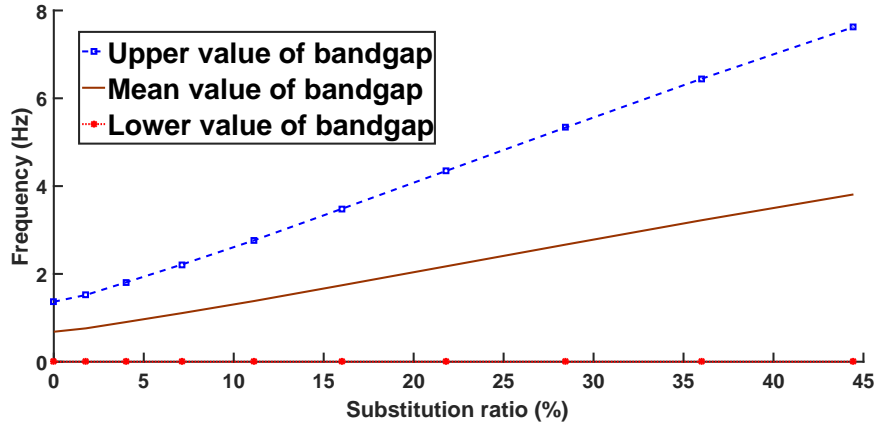


Figure 3.19: Bandgap versus substitution ratio plot for clamped configuration of square concrete inclusions.

3.4 Summary

In this chapter, we first noticed the importance of structure geometry to further enhance the filtering effects of clamped seismic metamaterials consisting of cylindrical inertial resonators clamped at their bottom. The clamping makes possible a zero-frequency stopband of interest for earthquake protection, whereas the microstructure allows for additional stopbands at higher frequencies that might find applications in the suppression of ground vibrations induced by traffic. We stress that such types of cylindrical inclusions mixing stress-free and clamped boundary conditions have no counterpart in electromagnetism since these conditions model infinite conducting inclusions in irreconcilable light polarizations (transverse electric and magnetic fields, for stress-free and clamped conditions, respectively). We have explored the effect of different internal geometries of SMs toward obtaining a wider bandgap with an equal amount of inclusions and its positioning in the frequency spectrum, i.e., a lower bandgap region (approximately below 20 Hz) is essential for most of the engineering applications. We have arrived at a configuration of columns having a square cross-section with sides aligned with a square lattice that gives a wider bandgap in comparison to circular cross-section inclusions for the same substitution ratio of the

constituent material. This has been demonstrated by computing transmission losses in addition to the dispersion curves for different internal geometries of the SM. We have also performed an analysis of the constituent material, observing that, not only steel but concrete the conventional construction material, can also be used to design inclusions for large wave attenuation. This is important for the industrial scale-up of the technology because, concrete is cost-effective, easy to cast directly at the construction site, and easy to provide arbitrary geometry of the microstructure. We have observed that concrete shows a bandgap for very soft soil. Since very soft soil is not suitable for construction, we prescribe an architecture of SM, with concrete inclusions in a narrow strip of very soft soil matrix surrounding the protected region. Even though we have arrived at an efficient design of SM, our study opens the door to further generalization. For example, we assume linear elastic materials, and it would be interesting to see what happens in the case of material and geometric non-linearity; soil often shows a significant amount of plastic deformation. In a future study, we would like to pay more attention to damping of ground vibrations, introducing so-called K-Dampers, such as those used to reduce vibration of bridges [107] and to mitigate site-city interactions [78] using the SMs which we introduced here.

Chapter 4

A numerical study to assess the role of pre-stressed inclusions on enhancing fracture toughness and strength of periodic composites

A rational design for simultaneous toughening and strengthening in composites would be significant for myriad applications in fracture-related problems. Nacre simultaneously exhibits extremely high toughness (approximately 3000 times the constituent materials) and high strength, being one of the classic examples of the brilliant solutions nature can come up with based on necessity. Several experimental studies have suggested that the underlying “brick and mortar” microstructure of the nacre could be responsible for the high performance (high strength and high toughness). However, it has been realized that the engineered composites can not achieve the desired performance by only mimicking the “brick and mortar” structure. Naturally, the question arises whether there is any additional mechanism that is possibly responsible for the high performance of nacre and may be mimicked in the engineered composites to achieve the desired high performance. In this chapter, numerical simulations show that the design of high-performance engineered composites can be achieved by introducing pre-stress in the inclusions. We have carried out mode-I and mode-II fracture simulations in periodic composites with both hard and soft pre-stressed inclusions to

assess their role in the performance of composites. For modeling crack propagation in mode I, we have adopted the surfing boundary conditions proposed by [108], and appropriately extended it for modeling crack propagation in mode II. The present work indicates that a study on the existence of a pre-stressed condition of the platelets in the nacre may be a topic of research interest to explore the origin of the high performance of the nacre.

4.1 Introduction

From naturally formed biological systems, e.g. nacre, to engineered materials, heterogeneity arising from internal geometry has been found to enhance the fracture property of solids ([109, 110, 111, 112, 113]). With the advent of additive manufacturing technology, the idea of incorporating inclusions is increasingly becoming popular. It is now possible to introduce heterogeneity in a homogeneous media via elastic mismatch on a micro to macro scale. However, a rational design to achieve simultaneously toughened and strengthened material to resist fracture is still a challenge to modern engineering ([114]). Towards achieving this we note that many biological systems resolve this issue by efficiently evolving their material composition and internal geometries, incorporating hard minerals into soft polymer matrices, and forming intricate composites to resist external threat ([115, 116, 117, 118, 119]). For instance, nacre with the chemical composition of 95% aragonite (a ceramic material) and 5% biopolymer shows excellent fracture properties (fracture toughness is about 3000 times its main constituent, aragonite). This extremely high toughness is not yet achieved in synthetic nacre-inspired composites ([120, 121]). While bio-inspired composites show enhanced fracture toughness, unfortunately, they suffer from compromising strength. A common choice for hard inclusions is high-modulus ceramic in the usual soft matrix, e.g. in designing protective armor. High fracture toughening is achieved by introducing ceramic-based hard inclusions in a soft matrix that provides contrast in elastic properties and thereby, crack repelling, deflection, meandering, etc. ([122, 123, 124]). Due to the stress discontinuities at the matrix-inclusion interface, delamination also

occurs that drastically reducing the fracture strength of the composite. Therefore, there is a trade-off between fracture strength and fracture toughness that poses a major difficulty.

Past studies have shown that the effective fracture toughness of an engineered composite is larger than its constituent material, but not so significantly high as seen in nacre ([125]). [108], [126], [127], [128], [129] and [130] have shown that layered solid with alternating layers of different elastic moduli and fracture toughness has an overall toughness that surpasses its constituents. They ascribe the toughening mechanism of solid layers to stress fluctuations and crack re-nucleation. They have used the so-called surfing boundary conditions (SBCs) for the crack to propagate. However, layered solids are difficult to implement in composites like armors, and also, the obtained toughness is not so significant in comparison to its constituent materials. Moreover, these studies are only restricted to macroscopic mode-I loading (opening mode), whereas, mode-II loading (shear mode) is itself a critical phenomenon to understand in resisting fracture. In the present work, we propose introducing pre-stress in the inclusions as a possible route to design engineered composites with desired fracture toughness and strength. For our numerical simulations, we have adopted the SBCs proposed by [108] and appropriately extended it to mode-II fracture propagation. We have chosen a microstructural (or unit cell) configuration for the composite having a hard/soft cubic shape of inclusions in an alumina matrix. We have selected ceramic composites in the present study as they can be easily synthesized by reactive hot pressing in the form of nanocomposites ([1], [131]) and have wide usage in armor applications. In this context one may note that shape memory ceramics are classic examples where initial stresses can be introduced via stress induced martensitic transformation (SIMT) in which morphology is governed by shear-strain energy ([132], [133], [134]). This diffusion-less transformation is accomplished by large change in shape/volume and thereby local compressive/tensile stresses are introduced, while its crystallography changes from tetragonal to monoclinic phase (austenite to martensite phase) ([135], [136]).

The pre-stressing technique has always been advantageous in increasing the load-carrying capacity of materials and structures ([137]). Understanding the effect of

pre-stressing a material, both on theoretical and practical fronts, always forms active research, especially in the context of fracture mechanics. For example, studies on stress concentration, shear band formation, and energy release rate (ERR) when a stiffener is placed in a pre-stressed orthotropic elastic medium ([138, 139, 140]); studies on stress intensity factors (SIF) and crack opening displacement (COD) at the crack tips in a pre-stressed cracked-isotropic elastic medium ([141, 142]); studies on calculating J -integral and fatigue crack arrest in pre-stressed reinforced concrete and steel members ([31, 143]), etc. However, most of these studies are limited to understanding macroscopic behavior and remain silent on microscopic details, which are important aspects in heterogeneous media since crack propagation can be entirely different on a micro-scale owing to the elastic contrasts in the medium. In our numerical results, we show that the minimum driving force for a crack to propagate in a heterogeneous media can be substantially increased if pre-stresses are induced in the inclusion, thus increasing its fracture toughness and strength.

In this work, we have shown the effect of pre-stressed inclusion on the performance of composites for crack propagation under a quasi-static condition. Since crack propagation in a heterogeneous media is a complex phenomenon within itself, present work is limited to linear elasticity problems, i.e., brittle fracture in both matrix and inclusions. Moreover, brittle solids are prone to catastrophic failure which itself forms an important study. We have considered the cubic shape of inclusions for which a plane stress modeling can be done [112] and carried out two-dimensional fracture simulations by introducing pre-stress in the inclusion. Here, the effect of compressing and tensile prestressed inclusions on the fracture toughness and fracture strength is addressed. We have organized the rest of the article as follows. We have defined a boundary value problem in Section 4.2 on a periodic microstructure with an initial crack. We have briefly described surfing boundary conditions (SBCs) proposed by [108] for mode I and proposed an extension of the idea of SBCs to mode II crack propagation. We have provided mode I and mode II fracture simulations on periodic composites with both hard and soft inclusions in Section 4.3.

4.2 Boundary value problem

Consider a periodic composite body that can be described by an open set Ω with boundary $\partial\Omega$ and periodic unit cell Ω^c as shown in Fig. 4.1. Dirichlet boundary conditions are applied as prescribed displacements $\bar{\mathbf{u}}$ on $\partial\Omega_u$ and Neumann conditions are applied as prescribed traction $\bar{\mathbf{t}}$ with surface normal \mathbf{n} on $\partial\Omega_t$. The material body may consist of several isotropic inclusions $\Omega =: \{\Omega_c^i\}_{i=1}^n$ with $\Omega_c^i \cap \Omega_c^j = \emptyset$, separated by interfaces Γ^i . Let the crack surface be defined by $\partial\Omega_{cr} = \partial\Omega_{cr}^+ \cup \partial\Omega_{cr}^-$ with superscripts '+' and '-' as upper and lower surfaces, respectively. Let \mathbf{b} be the body force per unit volume. The linear momentum balance for the material body is given below:

$$\nabla \cdot \boldsymbol{\sigma} + \mathbf{b} = \mathbf{0} \quad \text{in } \Omega, \quad (4.1)$$

with boundary conditions as:

$$\begin{aligned} \mathbf{u} &= \bar{\mathbf{u}} & \text{on } \partial\Omega_u, \\ \boldsymbol{\sigma} \mathbf{n} &= \bar{\mathbf{t}} & \text{on } \partial\Omega_t, \\ \boldsymbol{\sigma} \mathbf{n} &= \mathbf{0} & \text{on } \partial\Omega_{cr}, \end{aligned} \quad (4.2)$$

where $\boldsymbol{\sigma}$ is the Cauchy stress tensor, related to strain $\boldsymbol{\epsilon}$ tensor as $\boldsymbol{\sigma} = \mathbb{C}\boldsymbol{\epsilon}$; \mathbb{C} is the fourth order elasticity tensor. For inclusions, on interfaces Γ^i , the equilibrium condition is taken as continuous displacement field, i.e., $[[\mathbf{u}]] := \mathbf{u}^{(2)} - \mathbf{u}^{(1)} = \mathbf{0}$ and discontinuous traction field, i.e., $[[\mathbf{t}]] := -(\boldsymbol{\sigma}^{(2)} - \boldsymbol{\sigma}^{(1)}) \mathbf{n}^{(1)}$; superscripts (1) and (2) denote the two sides of the interface Γ^i . In presence of an initial stress $\boldsymbol{\sigma}_0$ in the material body, the linear momentum balance can be given by

$$\nabla \cdot (\boldsymbol{\sigma} + \boldsymbol{\sigma}_0) + \mathbf{b} = \mathbf{0} \quad \text{in } \Omega. \quad (4.3)$$

The finite element discretized form of Eqn. (4.3) can be arrived at by writing the

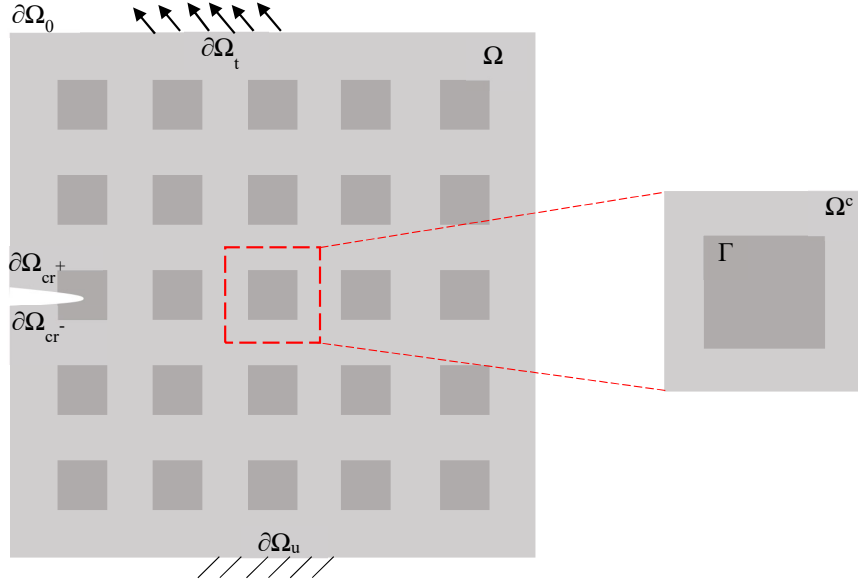


Figure 4.1: Left sub-figure shows the periodic micro-structure described by an open set Ω with boundary $\partial\Omega = \partial\Omega_u \cup \partial\Omega_t \cup \partial\Omega_{cr} \cup \partial\Omega_0$. The domain Ω can be identified as the assembly formed by repetition of the unit cell, Ω^c having isotropic phases separated by Γ , as shown in the right sub-figure.

corresponding virtual work relation as given below:

$$\int_{\Omega} (\boldsymbol{\sigma} + \boldsymbol{\sigma}_0) : \tilde{\boldsymbol{\epsilon}} d\Omega = \int_{\Omega} \mathbf{b} \cdot \tilde{\mathbf{u}} d\Omega + \int_{\partial\Omega_t} \mathbf{t} \cdot \tilde{\mathbf{u}} d(\partial\Omega_t), \quad (4.4)$$

where tilde symbol denotes the virtual field and $\mathbf{u} \in \mathcal{U}$ is kinematically admissible displacement field such that

$$\mathcal{U} = \left\{ \mathbf{u} \mid \mathbf{u} \in (H^1(\Omega))^d, \mathbf{u} = \bar{\mathbf{u}} \text{ on } \partial\Omega_u \right\}, \quad (4.5)$$

where d is the dimension of \mathbf{u} . Functions of $H^1(\Omega)$ are implicitly discontinuous on crack surface $\partial\Omega_{cr}$. ($\tilde{\cdot}$) symbol denotes the virtual field.

4.2.1 Crack modelling

We have modeled crack using the level set method in an extended finite element framework ([144], [145], [146], [147]). For an arbitrary point $\mathbf{x} \in \Omega$, ϕ and φ are defined as:

[1] ϕ is the signed distance function from the crack surface $\partial\Omega_{cr}$ given by:

$$\phi(\mathbf{x}) = \min_{\bar{\mathbf{x}} \in \partial\Omega_{cr}} \|\mathbf{x} - \bar{\mathbf{x}}\| (\mathbf{n}^+ \cdot (\mathbf{x} - \bar{\mathbf{x}})) \quad (4.6)$$

where \mathbf{n}^+ is the outward normal vector to $\partial\Omega_{cr}$.

[2] φ is signed distance function approximately orthogonal to ϕ , i.e.,

$$\nabla\phi \cdot \nabla\varphi \approx 0 \quad (4.7)$$

Crack-tip is defined by intersection of $\phi(\mathbf{x}) = 0$ and $\varphi(\mathbf{x}) = 0$; and crack surface by $\phi(\mathbf{x}) = 0$ and $\varphi(\mathbf{x}) < 0$. Crack-tip polar coordinates can be represented as:

$$r = \sqrt{\phi^2(\mathbf{x}) + \varphi^2(\mathbf{x})}, \quad \theta = \tan^{-1} \left(\frac{\phi}{\varphi} \right) \quad (4.8)$$

4.2.2 XFEM discretisation

Eq. (4.4) is discretized in Galerkin form considering arbitrariness of nodal variations in an extended finite element method (XFEM) framework to account for discontinuities in displacement fields due to crack ([148, 149, 150]). The XFEM approximation for the field variable is given by ([151, 152, 153, 56, 154, 155]):

$$\begin{aligned} \mathbf{u}^h(\mathbf{x}) = & \sum_{J \in \mathcal{N}_s} N_J(\mathbf{x}) \mathbf{u}_J \\ & + \sum_{J \in \mathcal{N}_{cs}} N_J(\mathbf{x}) (H(\phi(\mathbf{x})) - H(\phi(\mathbf{x}_J))) \mathbf{a}_J \\ & + \sum_{J \in \mathcal{N}_{ct}} N_J(\mathbf{x}) R(\mathbf{x}) \left(\sum_{k=1}^4 (F_k(\mathbf{x}) - F_k(\mathbf{x}_J)) \mathbf{b}_J^k \right) \\ & + \sum_{J \in \mathcal{N}_{int}} N_J(\mathbf{x}) \xi(\mathbf{x}) \mathbf{q}_J, \end{aligned} \quad (4.9)$$

where, \mathcal{N}_s , \mathcal{N}_{cs} , \mathcal{N}_{ct} and \mathcal{N}_{int} are nodal sets corresponding to standard DOF \mathbf{u}_J , enriched DOF \mathbf{a}_J having crack surface, \mathbf{b}_J having crack tip and \mathbf{q}_J passing the interface Γ in their support domain. Note that \mathbf{a}_J and \mathbf{b}_J are additional DOFs that are used

to adjust the amplitude of shape functions to approximate the displacement field in the presence of strong discontinuities such as cracks. Similarly \mathbf{q}_J is for weak discontinuities such as an interface. Jumps in the displacement field along the crack surface are introduced by Heaviside step function $H(\phi)$: +1 if ϕ is on one side of the crack surface and -1 otherwise ([54]). The basis function $F(x)$ for the asymptotic near crack-tip displacement field can be given in terms of polar coordinates centered at the crack tip as

$$F(r, \theta) = \left[\sqrt{r} \sin \frac{\theta}{2}, \sqrt{r} \cos \frac{\theta}{2}, \sqrt{r} \sin \frac{\theta}{2} \sin \theta, \sqrt{r} \cos \frac{\theta}{2} \sin \theta \right]. \quad (4.10)$$

The ramp function $R(\mathbf{x}) = \sum_{J \in \mathcal{N}_r} N_J(\mathbf{x})$ is used to adjust $F(x)$ such that it decreases progressively and vanishes outside a chosen support, r for the crack tip, where \mathcal{N}_r is the nodal set that contains the chosen radius r . To modify the shape functions of the blending elements around the weak discontinuity, Γ , we have used a function $\xi(\mathbf{x})$ defined as ([54]):

$$\xi(\mathbf{x}) = \sum_{J \in \mathcal{N}_{int}} |\phi(\mathbf{x}_J)| N_J(\mathbf{x}) - \left| \sum_{J \in \mathcal{N}_{int}} \phi(\mathbf{x}_J) N_J(\mathbf{x}) \right| \quad (4.11)$$

4.2.3 Crack propagation

Cracks grow along the weakest plane and generate non-zero stress intensity factors (SIF) in mode-I and II. Therefore, a mixed-mode crack propagation criterion is required to check the initiation of crack growth and to determine its direction and increment. Out of the several mixed-mode crack growth criteria, we chose the maximum circumferential tension criteria. The use of this criterion is motivated by the assumption that the size of the investigated structure has a minor influence on the crack path since the solutions are based on the local stress field close to the crack tip ([156]). A crack will open in a radial direction within a plane perpendicular to the maximum tension when the maximum circumference tension stress intensity factor

exceeds a critical material constant ([55]). Hence the criterion is defined as:

$$\frac{K_I}{K_{eq}} \cos^3 \frac{\theta_0}{2} - \frac{3 K_{II}}{2 K_{eq}} \cos \frac{\theta_0}{2} \sin \theta_0 = 1, \quad (4.12)$$

where K_I and K_{II} are stress intensity factors corresponding to mode-I and II loading respectively and K_{eq} is the material fracture toughness. θ_0 is the kinking angle at the crack tip found by solving the following equation:

$$K_I \sin \theta + K_{II} (3 \cos \theta - 1) = 0 \text{ with } \begin{cases} K_{II} \sin \frac{\theta}{2} < 0 \\ -\pi \leq \theta \leq \pi \\ K_I > 0. \end{cases} \quad (4.13)$$

Eq. (4.12) seems to depend only on values K_I and K_{II} , thus, no other data from the numerical model is required to compute the kinking angle. While simulating crack propagation, SIFs in the above expressions are evaluated by interaction integral method ([157]). The consequence of choosing such crack evolution criteria can be estimated as follows. For a pure mode-I loading, K_{II} will not evolve and θ remains zero. Similarly, for pure mode-II loading, K_I will not evolve, however; θ will have a finite value. To study the crack propagation in a heterogeneous media, we have used SBCs ([108]). This defines a macroscopic propagation law without resolving the microscopic details of the media. We apply a displacement-controlled load $\mathbf{u}^*(x, y, t)$ conforming to the analytic fracture mode displacement fields. SBCs are successfully applied as K_I controlled displacement fields under mode-I loading ([126, 128, 129, 130, 158]). We endeavor to extend this for K_{II} controlled displacement fields under mode-II loading ([159]). For that, we apply displacement-controlled loads as $\mathbf{u}_I^*(x, y, t) = \mathbf{U}_I(x - vt, y)$ and $\mathbf{u}_{II}^*(x, y, t) = \mathbf{U}_{II}(x - vt, y)$; where \mathbf{U}_I and \mathbf{U}_{II} are the analytic displacement

fields in opening and shearing mode, respectively:

$$\begin{aligned}
\text{Mode-I} & \begin{cases} \mathbf{U}_{Ix}(t) = \frac{K_I}{2\mu} \sqrt{\frac{r(t)}{2\pi}} (\kappa - \cos \theta(t)) \cos \frac{\theta(t)}{2} \\ \mathbf{U}_{Iy}(t) = \frac{K_I}{2\mu} \sqrt{\frac{r(t)}{2\pi}} (\kappa - \cos \theta(t)) \sin \frac{\theta(t)}{2}, \end{cases} \\
\text{Mode-II} & \begin{cases} \mathbf{U}_{IIx}(t) = \frac{K_{II}}{2\mu} \sqrt{\frac{r(t)}{2\pi}} (\kappa + 2 + \cos \theta(t)) \sin \frac{\theta(t)}{2} \\ \mathbf{U}_{IIy}(t) = -\frac{K_{II}}{2\mu} \sqrt{\frac{r(t)}{2\pi}} (\kappa - 2 + \cos \theta(t)) \cos \frac{\theta(t)}{2}, \end{cases}
\end{aligned} \tag{4.14}$$

where $(r(t), \theta(t))$ are time-dependent crack tip polar coordinates steadily translating with velocity v and is given by $r(t) = \sqrt{(x - vt)^2 + y^2}$ and $\theta(t) = \arctan \frac{y}{x - vt}$. Note that Eq. (4.14) serves as a boundary condition for the crack to propagate macroscopically with constant imposed velocity v . t represents a "fictitious" time used for the incremental formulation as the crack tip proceeds in space. For all the numerical simulations, we adopt a time step size $\Delta t = 0.05L/v$, where L is the length of domain in x-direction. One may refer to [126] for better understanding on time step (Δt) and imposed velocity (v). The magnitude of the loading is governed by varying stress intensity factor (K_I and K_{II}) and shear modulus (μ). For plane stress, $\kappa = \frac{3-\nu}{1+\nu}$ and for plane strain, $\kappa = 3 - 4\nu$. These boundary conditions act as a driving force for the crack at macroscopic scale, but will not, in any manner, restrain its growth at the microscopic scale, i.e., crack may deflect, meander, arrest, etc. at the microscopic level due to the presence of elastic contrast in heterogeneous media.

4.2.4 Fracture toughness

In linear elastic fracture mechanics (LEFM), the energy release rate at each instant is computed via far-field J -integral ([160]).

$$J = \int_{\mathcal{L}} (\mathcal{W} n_{\mathcal{L}_x} - \sigma_{ij} u_{i,x} n_{\mathcal{L}_j}) \partial \mathcal{L}, \tag{4.15}$$

where, \mathcal{W} is the strain energy density, \mathcal{L} is a closed counter-clockwise contour around the crack tip and $\mathbf{n}_{\mathcal{L}} = n_{\mathcal{L}x}\mathbf{e}_x + n_{\mathcal{L}y}\mathbf{e}_y$ is the outward normal to \mathcal{L} and $J = G_c = \frac{K_I^2}{E}$; G_c being critical energy release rate and referred as fracture toughness of the material. We compute the macroscopic energy release rate (J -integral) at each instant, which demonstrates a periodic pattern. We denote the maximum of this value as the effective fracture toughness of the heterogeneous medium, i.e., $G_c^{eff} = \max_t J(t)$ [108]. We chose the domain to be large enough as compared to the heterogeneity scale in the media and crack sufficiently far from the boundary to make J -integral path independent ([161]).

4.3 Numerical simulations

4.3.1 Simulation set-up

For numerical simulations, we have considered an alumina (Al_2O_3) matrix having geometry $11 \text{ mm} \times 11 \text{ mm}$. The results are computed using in-house code developed on MATLAB 2019a. To show the effect of hard and soft inclusions, we have chosen silicon carbide (SiC) and alumina (elastic modulus less than that used for matrix), respectively, as materials. The material properties are given in table 4.1. These materials are commonly used ceramics in armor applications [1]. The inclusions are symmetrically placed with center-to-center spacing of 2 mm, e.g. as shown for hard inclusions in fig. 4.5. The domain size in comparison to the inclusion size is approximately 11 times. However, we have also shown the effect of the size of the inclusions and the effect of type of periodicity with increasing domain size. We test-run simulations with increasing domain size and compute normalized J-integral (the path remains the same for all the domains). A compressive prestress load of 250 MPa is applied to the hard inclusions to study the effect. Note that the inclusion size and spacing between them for all the domains remain the same. From fig. 4.3(b), we observe that convergence is achieved beyond 21×21 inclusions. It also shows that a compressive prestress force in the inclusions shows an increase in fracture toughness in all the test domains. Fig. 4.2

shows that fracture strength is also converged after 21×21 inclusions. Next, to study the effect of inclusion shape, we test run with square-shaped, circular-shaped, and triangular-shaped inclusions on the converged domain, i.e., 21×21 inclusion domain. It is observed that with hard inclusions, there is not much change in the J-integral, i.e., the shape of the inclusions has a negligible effect with hard inclusions (even with applied compressive prestressing in the inclusions). we aim to address such concepts in our future work.

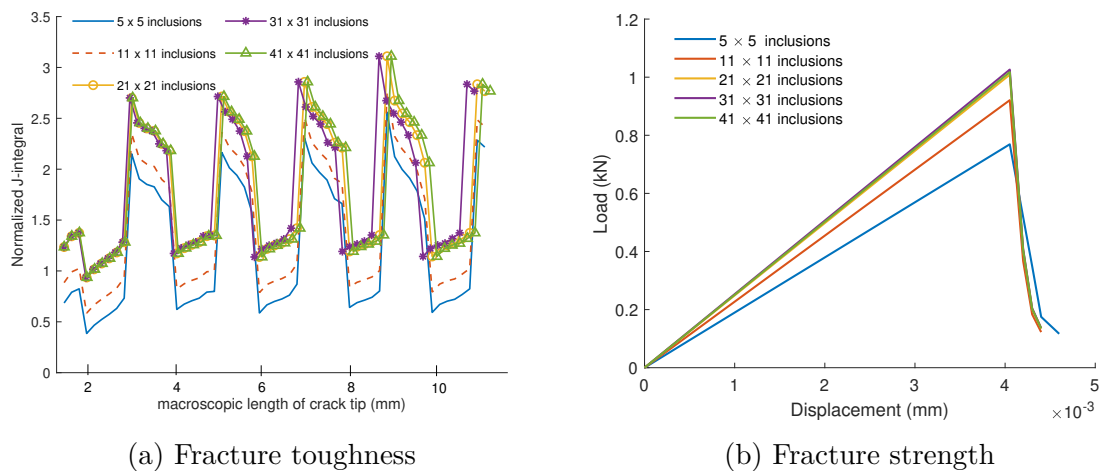


Figure 4.2: Effect of periodicity with hard inclusions under mode-I loading. A compressive pre-stress of 250 MPa is applied to the inclusions.

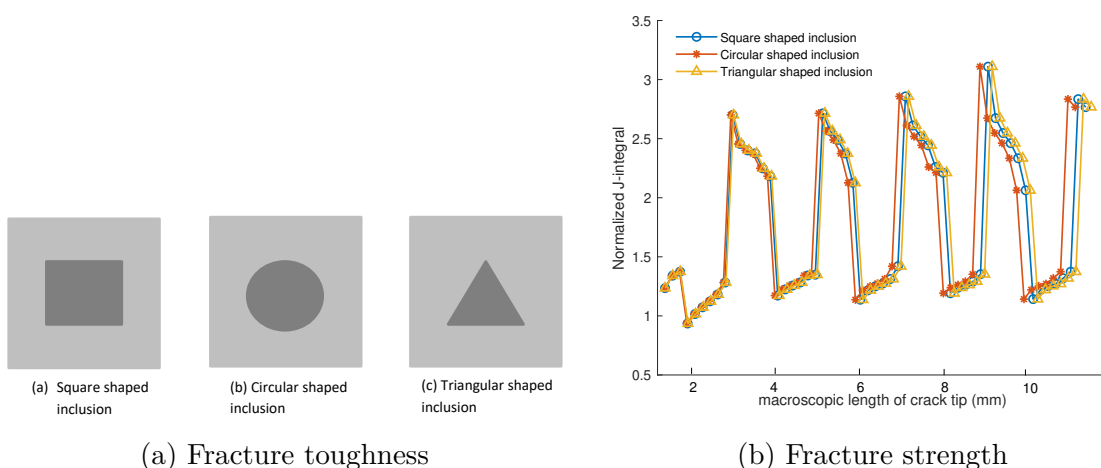


Figure 4.3: Effect of inclusion shape on fracture toughness under mode-I loading. A compressive pre-stress of 250 MPa is applied to the inclusions.

The present work is only based on five rows and five columns inclusions (denoted as 5×5) merely on pragmatic grounds and computational ease. The main focus of the present work is to discuss the effect of applying to prestress force in the inclusions. A predefined edge crack of 0.5 mm in length is given for initiating crack propagation. The inclusion geometries are all set as squares of side length 1 mm. Following [112, 111], we have considered square cross-sectioned inclusions with sides aligned with a cubic lattice. This type of arrangement has an advantage over other shapes and orientations in terms of attenuating the elastic waves propagating through the media and obtaining a wider frequency bandgap in the linear regime. Unless otherwise specified, geometries and material properties are kept the same for all our simulations. After mesh refinement and convergence study for the numerical model, the domain is discretized using 114962 triangular elements and 57480 nodes. Note that the length of the element edges is considered as an immediate measure of the mesh refinement level adopted in our simulations. Mesh is not refined in the crack propagation direction. However, after the convergence study, a mesh with a maximum size of 0.025 yields good results. A convergence plot for the same is shown below.

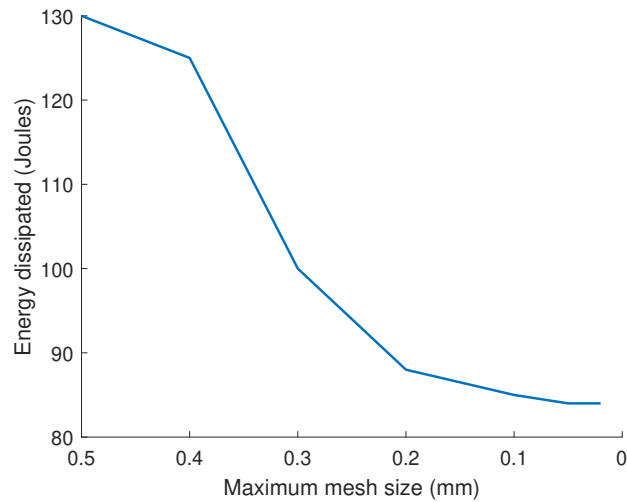


Figure 4.4: Convergence plot with different mesh sizes. Good convergence is shown for the mesh size 0.02 mm.

The minimum and maximum sizes of the elements are 0.021 mm and 0.025 mm, respectively, and the corresponding areas are 0.0376 mm^2 and 0.0703 mm^2 , respectively.

It should be noted that numerical integration should be performed on sub-elements since discontinuity will exist in the integrands across the crack interface as it cuts the elements. For each increment in crack length, i.e., for each t we have used a polar integration scheme for crack tip element with branch enrichment with 13 and 7 integration points per sub-element in the radial and angular directions, respectively [162]. The Standard quadrature scheme with 33 and 1 integration points per sub-element is used for completely split with branch enrichment and Heaviside enrichment, respectively. For the non-split elements with branch enrichment standard quadrature scheme with 33 integration points per element is used. SBCs, as given in Eq. (4.14), are applied as displacement load at the top and bottom edges of the domain Ω . K_I/K_{II} and μ in Eq. (4.14) are set as: $K_I/K_{II} = 1.5\sqrt{G_c^{num}E}$ and $\mu = \frac{E}{2(1+\nu)}$. G_c^{num} is the critical energy release rate estimated [163] (using LEFM) by solving a conjugate numerical model with homogenized elastic properties :

$$G_c^{num} = -\frac{dU_s}{dl_i} + \frac{dW_{ext}}{dl_i} \quad (4.16)$$

where, first term of Eq. (4.16) denotes the rate of strain energy release from the domain and second term denotes the rate of external work done with respect to the extension of crack tip branch area l_i . U_s for the model is estimated from the homogenized elastic tensor calculated by asymptotic homogenization method, where the relation of stress to strain can be defined as [164, 165].

$$\boldsymbol{\sigma} = \mathbb{C} : \boldsymbol{\epsilon} = (\mathbb{C} - \mathbb{C}^0) : \boldsymbol{\epsilon} + \mathbb{C}^0 : \boldsymbol{\epsilon} \quad (4.17)$$

where \mathbb{C}^0 is the elastic tensor of homogeneous material and the material difference at any arbitrary location of solid having \mathbb{C} as elastic tensor will result in polarization stress $\boldsymbol{\tau} = (\mathbb{C} - \mathbb{C}^0) : \boldsymbol{\epsilon}$. Substituting Eq. (4.17) into (4.3), we get

$$\nabla \cdot (\boldsymbol{\tau} + \boldsymbol{\sigma}_0 + \mathbb{C}^0 : \boldsymbol{\epsilon}) + \mathbf{b} = \mathbf{0} \quad (4.18)$$

Extending and Writing Eq. (4.18) in Einstein tensor form, we get:

$$\mathbb{C}_{ijkl}^0 u_{k,lj} + b_i + (\tau_{ij,j} + \sigma_{0ij,j}) = 0 \quad (4.19)$$

the solution to Eq. (4.19), i.e., displacement fields takes the following form ([166, 165]):

$$\mathbf{u} = \mathbf{u}^0(\mathbf{x}, \mathbf{y}) + \gamma \mathbf{u}^1(\mathbf{x}, \mathbf{y}) \quad (4.20)$$

where $\mathbf{y} = \mathbf{x}/\gamma$ denotes the position relation in macro- and micro-coordinate with a constant $0 < \gamma \ll 1$. \mathbf{u}^0 is the solution on macro-scale to $\mathbb{C}_{ijkl}^0 u_{k,lj} + b_i + \sigma_{0ij,j} = 0$, where as \mathbf{u}^1 is the solution on micro-scale to the following characteristic equation ([165]):

$$\int_{\Omega} \mathbb{C}_{ijmn} \epsilon_{ij} \epsilon_{mn} (u_i^{1(kl)}) d\Omega = \int_{\Omega} \mathbb{C}_{ijkl} \epsilon_{ij} \epsilon_{mn}^{0(kl)} d\Omega \quad (4.21)$$

where, $\epsilon_{mn}^{0(kl)}$ are linearly independent unit test strains which in 2D takes the form $[1 \ 0 \ 0]^T$, $[0 \ 1 \ 0]^T$ and $[0 \ 0 \ 1]^T$, respectively. Finally, the homogenized elastic tensor can be written as ([167]):

$$\mathbb{C}_{ijkl}^H = \frac{1}{\|\Omega\|} \int_{\Omega} \mathbb{C}_{mnrst} (\epsilon_{mn}^{0(ij)} - \epsilon_{mn}^{ij}(u_m^{1(ij)})) (\epsilon_{rs}^{0(kl)} - \epsilon_{rs}^{kl}(u_m^{1(kl)})) d\Omega \quad (4.22)$$

Here, $\|\Omega\|$ denotes the volume of the unit cell. Note that, for all our numerical cases, we set time step as $\Delta t = 0.05L/v$; L is the length of the domain Ω and report J -integral in a normalized form, i.e., $\bar{J} = J/G_c^{num}$.

Table 4.1: Ceramic material properties (taken from [1, 2])

Materials	Elastic modulus E (GPa)	Poisson's ratio	Toughness (MPa \sqrt{m})
Alumina (as matrix)	221	0.20	3.0
Alumina (as soft inclusions)	160	0.20	3.0
Silicon carbide (as hard inclusions)	453	0.16	5.1

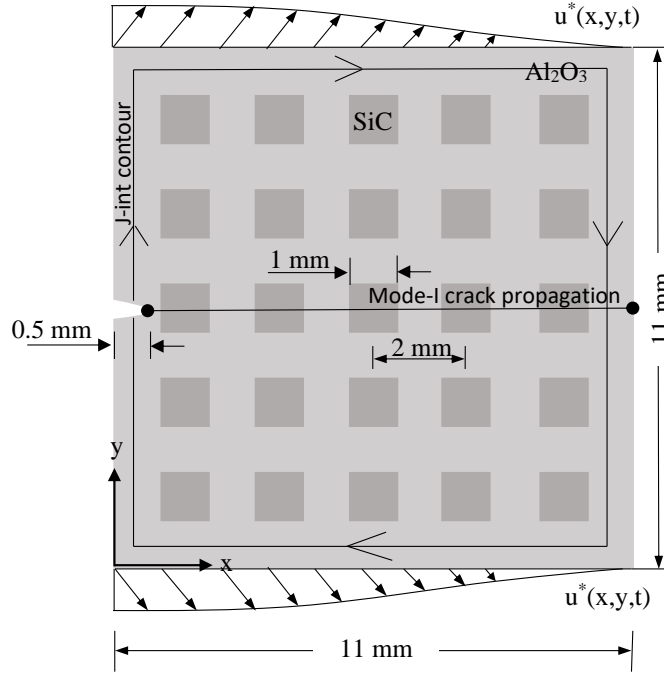


Figure 4.5: Simulation setup for mode-I crack propagation.

4.3.2 Toughening and strengthening mechanism in mode-I fracture

4.3.2.1 Effect of hard inclusions

We set the geometry, material properties, and initial crack for the numerical model as stated in section 4.3.1. SBCs in mode-I (Eq. (4.14)) are applied at the top and bottom edges as tension forces. These forces will open up the crack and pure mode-I propagation is obtained. Initially, σ_0 is set to zero, i.e. null pre-stress. We compute G_{Ic} (or J), G_{Ic}^{num} and crack growth for each time step and have shown the plots in fig. 4.6(a). $J - integral$ increases as the crack propagates in the matrix (Al_2O_3) and decreases as it propagates in the hard region (SiC). To be precise, the stresses in heterogeneous media significantly vary due to elastic contrast. These stresses are low in the matrix region due to low elastic modulus, and thus, the driving force should be large enough to initiate crack propagation. $J - int$ thus begins to rise till it reaches a critical value and suddenly breaks through the matrix-inclusion interface. This is accompanied by sudden drop in the $J - int$. In the stiffer region (SiC), due to high

stress, the crack propagates at a relatively smaller driving force, which in the figure is shown by the drop in $J - int$. Moreover, G_{Ic}/G_{Ic}^{num} reaches a value approximately 2.1 times than the value of uniformly varying toughness (homogenized toughness, G_c^{num}), before the crack can propagate the macroscopic distance. This shows that the macroscopic toughness is higher than the uniformly varying toughness of the medium.

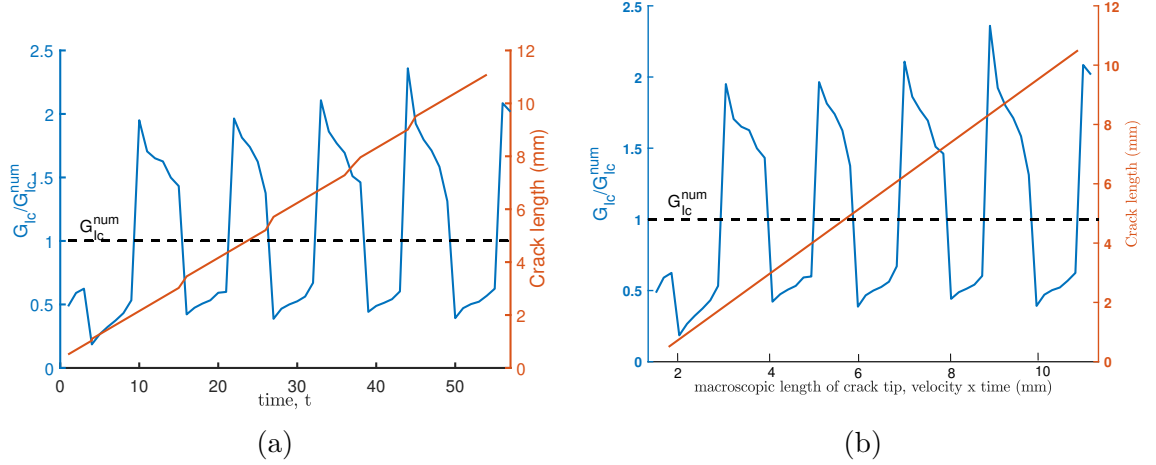


Figure 4.6: Toughening mechanism in mode-I fracture with hard inclusions ($\sigma_0=0$).

Stating on crack propagation, we observe that smooth propagation is lacking. Although, it propagates along a straight line, the crack gets trapped in the matrix region at the matrix-inclusion interface and G_{Ic}/G_{Ic}^{num} begins to rise. When G_{Ic}/G_{Ic}^{num} reaches a critical value, the crack breaks through the interface and enters the hard silicon carbide region. This is accompanied by small kinks in the crack propagation plot and sudden drops in G_{Ic}/G_{Ic}^{num} . The crack then propagates smoothly for a short duration before it gets trapped at the next interface. Since the crack propagates along a straight line and $\sigma_0 = 0$, the toughening mechanism is purely due to elastic heterogeneity and has no influence on other parameters.

Next, we investigate the effect of σ_0 , which has non-zero values in the inclusion region and zero elsewhere, i.e., pre-stressing the inclusions only. This can be made possible on practical front by means of stress induced martensitic transformation (SIMT) in the inclusion ceramic where the volume expansion introduces residual stresses. In such cases, negligible strains are developed at the interfaces in the matrix, which van-

ish away from the interface. Unless stated otherwise, σ_0 holds this description for the rest of the article. Initially, we apply pre-stress in the principal y-direction of the inclusions, i.e. in the transverse direction of crack propagation. We set $\sigma_{yy}^0 = \{\pm 250 \text{ MPa}, \pm 500 \text{ MPa}\}$; where ‘+’ and ‘-’ denotes tension and compression respectively. These values are justified, since in martensitic transformed ceramics residual stresses can be in the order of gigapascal [168]. Fig. 4.7(a) shows that a 250 MPa compressive pre-stress increases the effective toughness of the medium by 1.112 than that of without any pre-stress value, whereas a tensile pre-stress decreases it to 0.91. Further applying a compressive pre-stress (say 500 MPa), we can achieve approximately 1.21 times the increment in the fracture toughness. Similarly, if we increase the tensile prestress value up to 500 MPa, the fracture toughness is reduced to 0.82 times approximately. This is because a compressive pre-stress in the transverse direction of crack propagation tends to suppress the crack opening whereas in the case of tensile pre-stress it does the opposite. Note that in both the cases, i.e., tensile and compressive pre-stress, G_{Ic}^{eff} is higher than G_{Ic}^{num} . Thus, we can say that fracture toughness increases by applying a compressive pre-stressing force in the inclusions. Fig. 4.7(b) shows the load-displacement curve for different pre-stressing values in the principal y-direction. We observe that there is a significant increase by approximately 1.14 times the load-carrying capacity of the structure with pre-stressing the inclusions by 250 MPa. However, tensile pre-stress tends to decrease the load-carrying capacity of the structure by approximate 0.88 times %. Thus, this shows that with pre-stressing the inclusions, fracture strength also increases. Fig. 4.8 shows all possible cases for pre-stressing the inclusions, i.e., bi-axial compression ($\sigma_{xx}^0, \sigma_{yy}^0 < 0$), bi-axial tension ($\sigma_{xx}^0, \sigma_{yy}^0 > 0$), uni-axial tension ($\sigma_{xx}^0 > 0$ and $\sigma_{yy}^0 = 0$ or vice versa) and uni-axial compression ($\sigma_{xx}^0 < 0$ and $\sigma_{yy}^0 = 0$ or vice versa). As can be seen from the numerical simulations, a 250 MPa bi-axial compressive pre-stress loading increases the fracture toughness about 1.07 times than that of without bi-axial loading and simultaneously fracture strength is increased by 1.11 times than that of without bi-axial loading. Similarly, a 500 MPa bi-axial compressive pre-stress increases fracture toughness by 1.15 times and fracture strength by 1.2 times. On the other hand, a 250 MPa of

bi-axial tension loading reduces the fracture toughness and strength to 0.95 times and 0.97 times, respectively. Similarly, a 500 MPa of bi-axial tension loading reduces the fracture toughness and strength to 0.91 and 0.93 times, respectively.

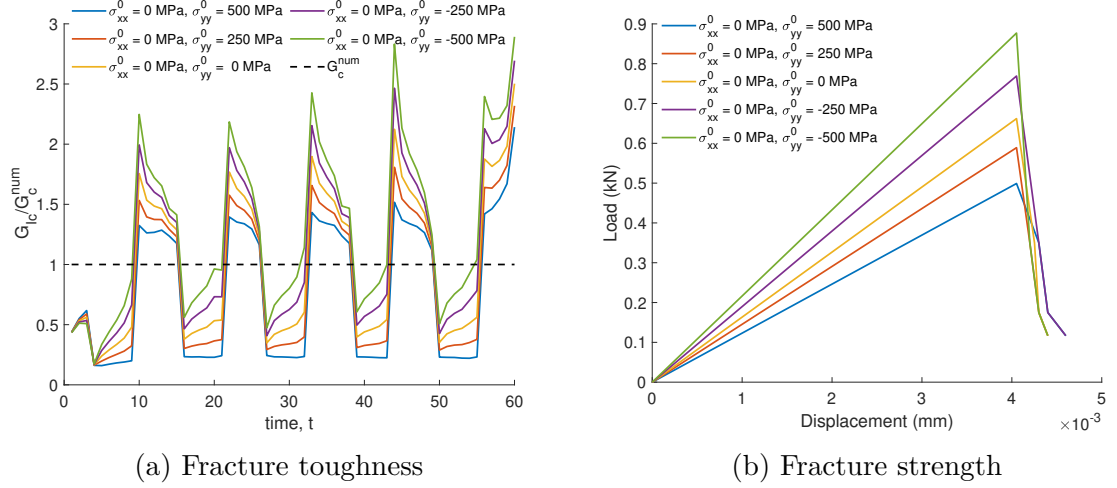


Figure 4.7: Toughening and strengthening effect in mode-I fracture with pre-stressing the hard inclusions in the principal y-direction only.

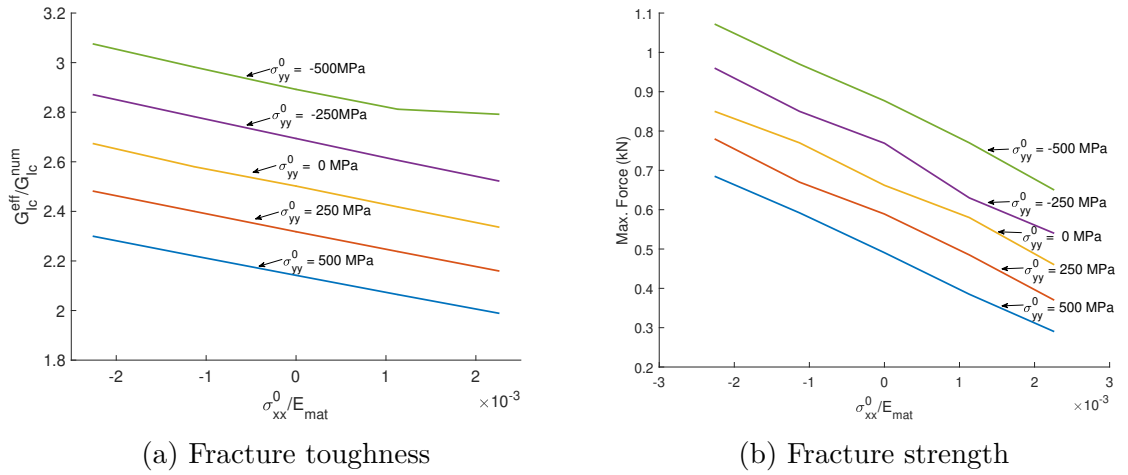


Figure 4.8: Toughening and strengthening effect in mode-I fracture with hard inclusions for uniaxial and biaxial, compression and tension pre-stressing force.

4.3.2.2 Effect of soft inclusions

We proceed, as discussed in the previous example, and set the geometries and the boundary conditions (SBCs in mode-I) same as that used in earlier (section 4.3.2.1).

For soft inclusions, we have considered the same material as a matrix, i.e, alumina but with lower elastic modulus. Fig. 4.9(a) shows the effect of pre-stressing the inclusions in uniaxial direction (y-direction) on fracture toughness. It is observed that the effective fracture toughness of the medium with soft inclusions is higher than that in comparison to the hard inclusions at the same pre-stressing values. This is because the matrix is now a stiffer region in comparison to the inclusions, and stresses in the inclusions are comparatively lower. Thus, the driving force in the inclusions should be high enough to initiate crack propagation. In the matrix, due to high stresses as compared to the inclusion region, the crack will propagate at a relatively smaller driving force. Moreover, the effective toughness in the case of soft inclusions is higher than the uniformly varying toughness, i.e. $G_{Ic}^{eff} > G_{Ic}^{num}$, thus showing a toughening mechanism. However, it is observed that there is no significant enhancement of fracture strength with soft inclusions (Fig. 4.9(b)). The strength will decrease when using softer materials. A plot for variation of normalized G_c^{eff} with σ_{xx}^0 (as a fraction of elastic modulus of the matrix) for all possible cases is shown in fig. 4.10(a). Clearly, applying bi-axial compressive pre-stress to the inclusions shows significant enhancement in the fracture toughness. However, there is only a slight improvement in the fracture strength (Fig. 4.10(b)).

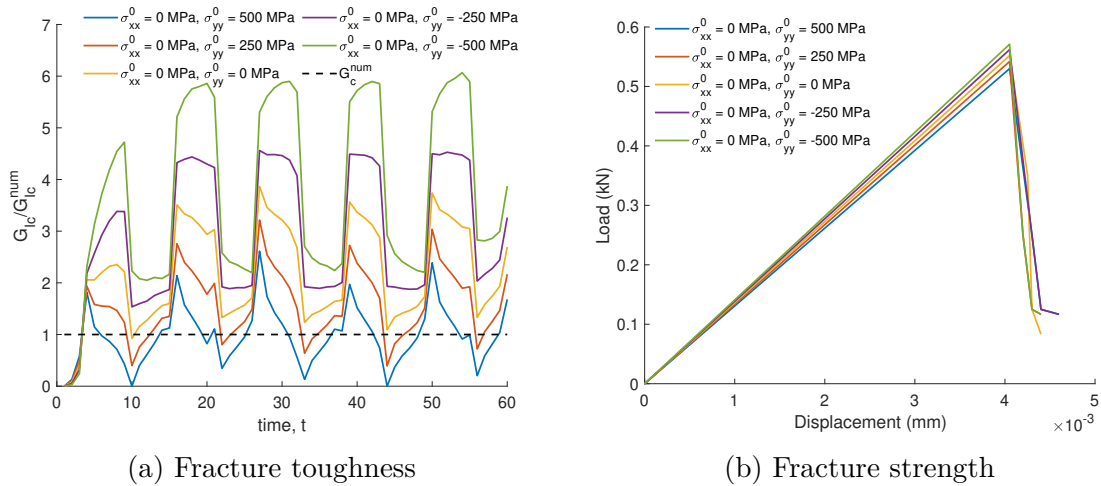


Figure 4.9: Toughening and strengthening effect in mode-I fracture with pre-stressing the soft inclusions in the principal y-direction only.

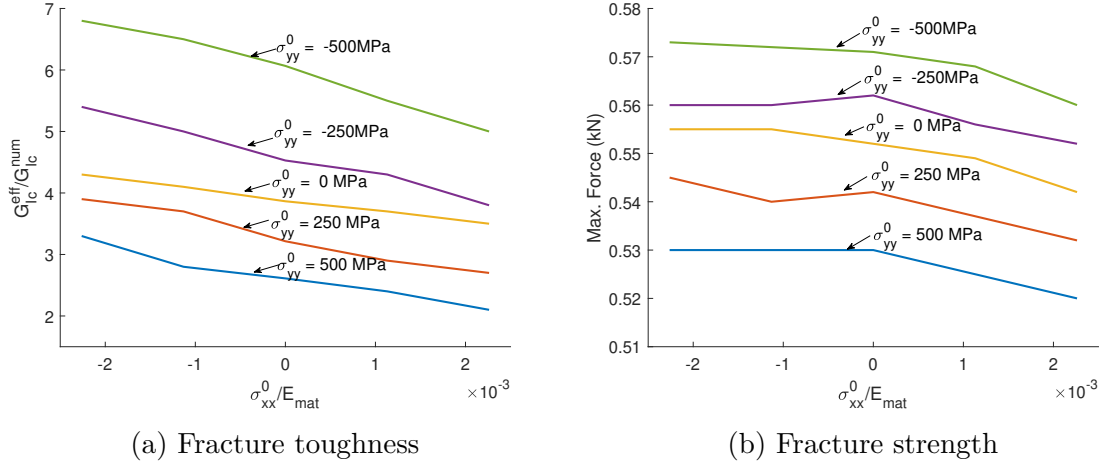


Figure 4.10: Toughening and strengthening effect in mode-I fracture with soft inclusions for uniaxial and biaxial, compression and tension pre-stressing force.

4.3.3 Toughening and strengthening mechanism in Mode II fracture

4.3.3.1 Effect of hard inclusions

The geometries and material properties are taken the same as used for mode-I crack propagation as in section 4.3.2. We use the boundary conditions as given in Eq. (4.14). Top edge is given U_{IIx} in the positive x-direction, whereas U_{IIy} is kept zero in the top edge. U_{IIx} and U_{IIy} for the bottom edge of the domain is kept zero as well. The left and right edge are kept free. These BCs will act as a driving force for the crack propagation which is purely mode-II in character. It is observed that with an initial crack length of 0.5 mm (as used for mode-I), the crack does not grow even when applying high shear force. The crack starts to grow when the length is approx. 0.97 mm. So we chose the initial crack length as 0.97 mm (since at 1 mm length the crack tip is exactly at the matrix-inclusion interface and its effect cannot be seen). We compute G_{IIc} for each time step with different values of σ_0 as shown in fig. 4.11(a). It is observed that with $\sigma_0 = 0$, i.e., null pre-stress, G_{IIc}^{eff} is approximately 1.7 times higher than G_c^{num} . This again shows that elastic contrast indicates a toughening mechanism. G_{IIc} is asymmetric and non-periodic in the plot since the crack cuts an

unequal fraction of the inclusions while it propagates from matrix to inclusion region and vice-versa in mode-II fracture (crack propagation is shown in fig. 4.12). Now, uni-axial pre-stressing force is applied in the principal y-direction of the inclusions. It is observed that effective toughness becomes 1.12 and 1.19 times with application of 250 MPa and 500 MPa of compressive pre-stressing force, respectively whereas it decreases to 0.95 and 0.89 times with 250 MPa and 500 MPa of tensile pre-stressing force, respectively. However, in both the cases G_{IIc}^{eff} is higher than G_{IIc}^{num} . Thus, a larger driving force is required for a crack to propagate in mode-II with hard inclusions and an effective toughening mechanism can be obtained. Fig. 4.11(b) shows the load-displacement curve for the hard-inclusion model with the same set of pre-stressing forces used to show effective fracture toughness. It is indicated that the load-carrying capacity of the structure by the application of 250 MPa compressive pre-stressing force is improved by approximately 1.18 times than that of without applying any pre-stressing force. This shows that pre-stressing the inclusions can enhance the fracture toughness and fracture strength simultaneously. Fig. 4.13(a) and 4.13(b) shows the variation of normalized G_{IIc}^{eff} and max. force carrying capacity of the structure with σ_{xx}^0 , respectively, for different σ_{yy}^0 . Thus, it can be seen that the fracture toughness and fracture strength are enhanced with the application of bi-axial compressive pre-stressing force to the inclusions.

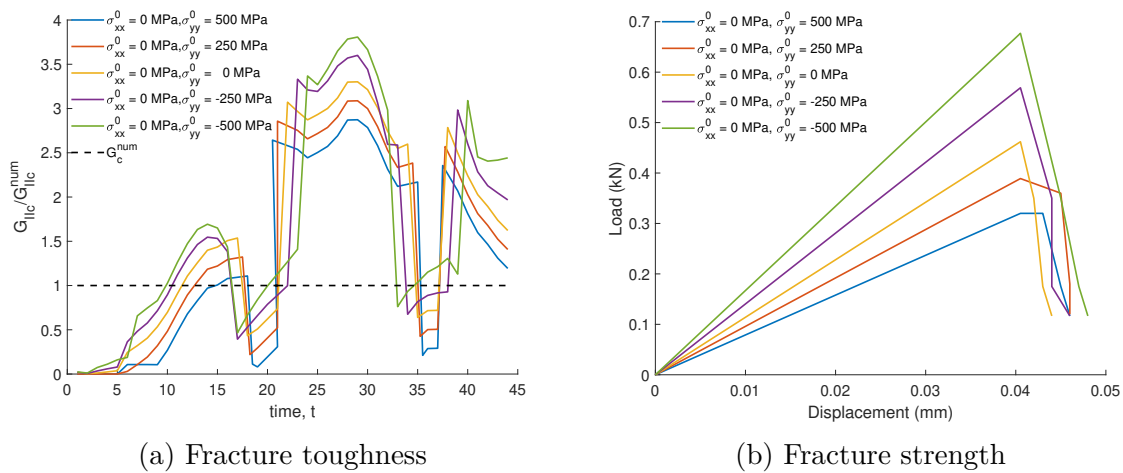


Figure 4.11: Toughening and strengthening effect in mode II fracture with hard inclusions.

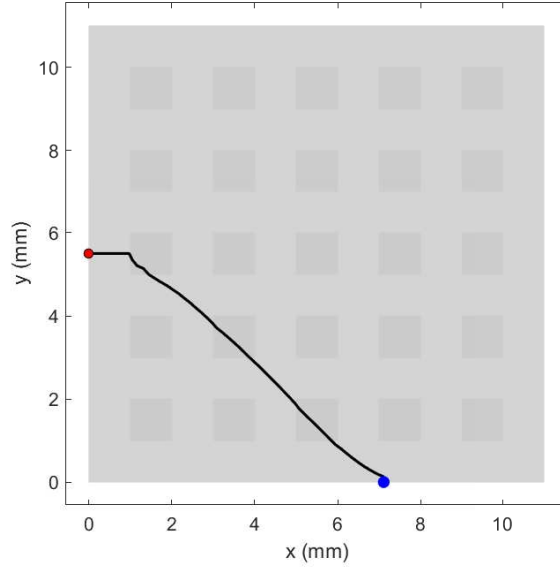


Figure 4.12: Crack propagation under mode-II loading with $\sigma_0 = 0$.

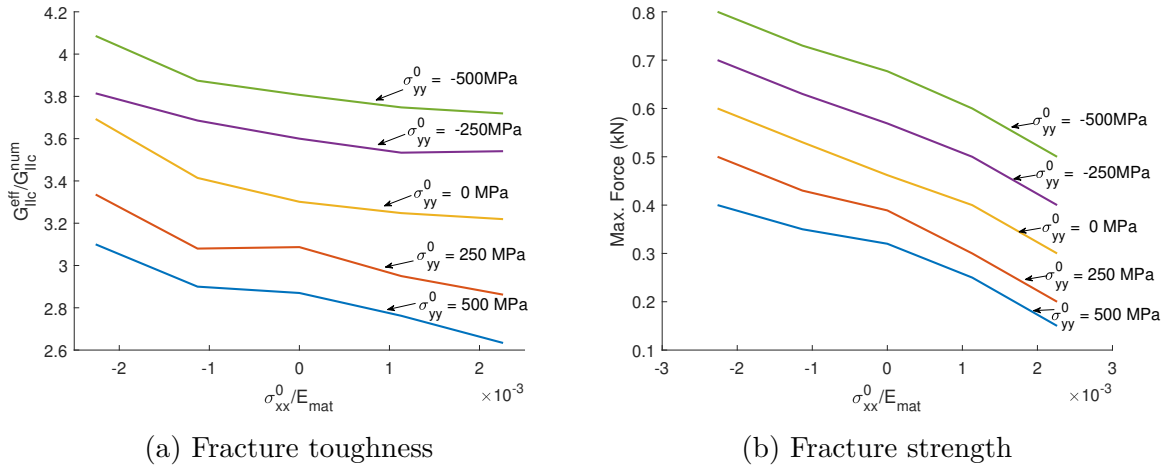


Figure 4.13: Toughening and strengthening effect in mode-II fracture with hard inclusions for uniaxial and biaxial, compression and tension pre-stress force.

4.3.3.2 Effect of soft inclusions

The geometries and boundary conditions are set the same as stated in section [4.3.3.1](#). Soft inclusions are represented as the same material that of the matrix but having a lower elastic modulus. The crack starts growing if the initial length is 0.97 mm. G_{IIc} is computed for different values of σ_0 . Fig. [4.14\(a\)](#) shows that pre-stressing

with the same set of values as used for hard inclusions, the effective fracture toughness is higher than that compared with hard inclusions. Compressive pre-stressing force gives higher toughness than the tensile pre-stressing force. This trend is similar to the observed results of mode-I crack propagation. Moreover, $G_{IIc}^{eff} > G_{IIc}^{num}$. Thus pre-stressing the inclusions enhances the fracture toughness in mode-II propagation also. Fig. 4.14(b) show the load-displacement curve for uni-axial pre-stressing values in principal y-direction. It is observed that there is not much improvement in the load-carrying capacity with soft inclusions. Fig. 4.15 shows the variation of effective fracture toughness and load-carrying capacity with σ_{xx}^0 . Bi-axial compressive pre-stress shows a significant increase in the fracture toughness, however, fracture strength is only slightly improved.

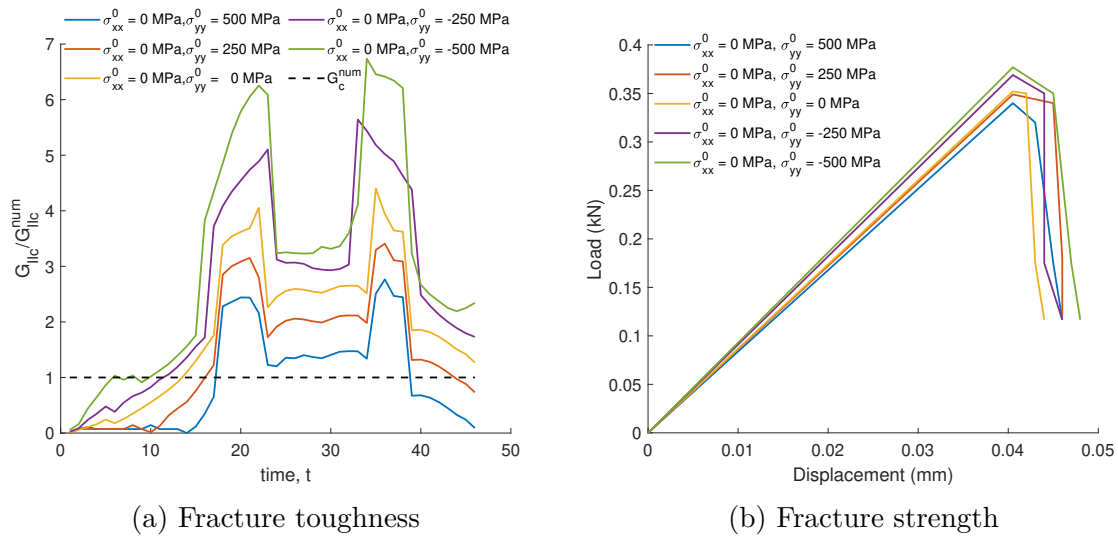


Figure 4.14: Toughening and strengthening effect in mode-II fracture with soft inclusions pre-stressed in the principal y-direction.

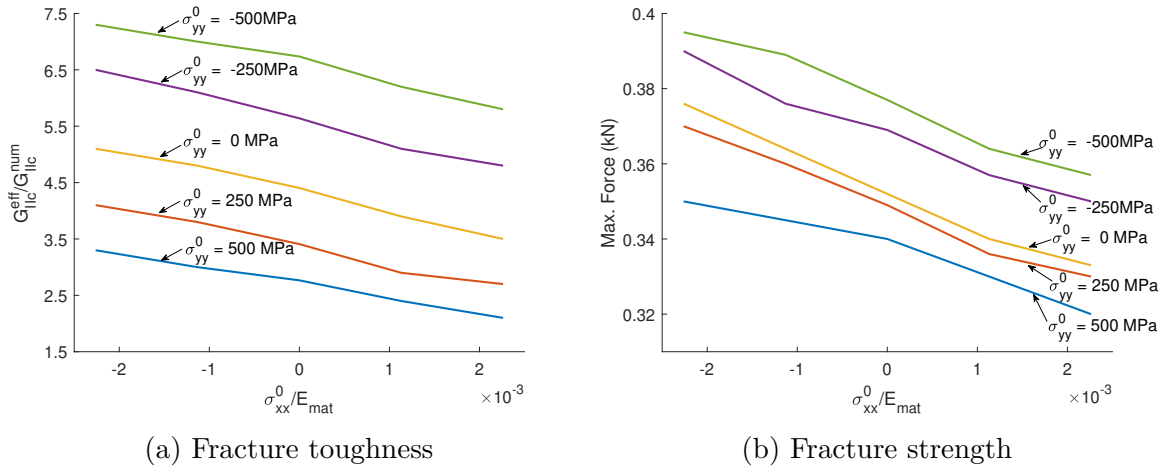


Figure 4.15: Toughening and strengthening effect in mode-II fracture with soft inclusions for uniaxial and biaxial, compression and tension pre-stress force.

4.4 Summary

In this study, we have carried out mode I and mode II fracture simulations on composites with inclusions and demonstrated that high-performance engineered composites can be designed by appropriately pre-stressing the inclusions. As anticipated, we have observed a significant enhancement in fracture toughness and strength of periodic composites when the inclusions are compressing pre-stressed. As seen from the numerical simulations, one may achieve simultaneous improvement in fracture toughness and strength by considering inclusions as hard and under a compressive pre-stressing force. With compressing pre-stressed soft inclusions, one may achieve even higher fracture toughness but with insignificant improvement in strength compared to hard inclusions. Hence, we recommend using pre-stressed hard inclusions where fracture toughness and strength are equally important, and soft inclusions where fracture toughness is predominately important. While this study is limited to brittle fracture (both inclusions and matrix), one may extend the present work to ductile matrix-brittle inclusions, where matrix plasticity may play an important role in fracture toughness and strength. We plan to extend this work and consider a geometrically interlocking shape for the inclusion such as osteomorphic brick to explore the effect of

interlocking geometry in presence of pre-stress in the inclusions. However, the effect of pre-stressed inclusion under a dynamic load may be more prominent and can be taken as a part of the immediate future scope of this study.

Chapter 5

Designing polymer metamaterial for protective armor: A coarse-grained formulation

Designing protective armor is important for varied civil and defense applications. Ceramic-polymer composite armors are particularly interesting for their high strength and lightweight with high energy absorption capability. While the function of ceramic is to retard ballistic impact penetration, polymer panel serves the purpose of absorbing high energy generated from the propagating elastic/stress waves. Enhancing this energy absorption capability of the armor is essential for its back-face signature (BFS). This chapter shows that energy absorption can be considerably enhanced if the bulk polymer panel is replaced with a polymer-based metamaterial. To demonstrate this, a comparison of the polymer metamaterial is made with its solid counterpart, i.e., bulk polymer matrix in terms of their respective transmission losses in the propagating elastic waves. We have also studied the effect of the size of the polymer metamaterial, e.g., by increasing the number of metamaterial layers and variation in the fiber length and thickness within a layer. A major challenge in such studies is the extreme computational overhead involved in solving continuum mechanics equations using finite element methods on the complex geometry with microstructure details. Note that microstructure details, i.e., geometry, size, and shape are mostly responsible for the nonintuitive properties of metamaterials. We have bypassed the huge computational

requirement by proposing a novel coarse-grained methodology based on the energetics of the structure of the polymer metamaterial. We envisage that the methodology would be useful to other related studies on mechanical metamaterials.

5.1 Introduction

A superior energy absorption mechanism is essential for protective armor toward resisting ballistic impacts [169]. In modern-day armor technology, advanced designs, e.g. ceramic-polymer composite armors are replacing their traditional counterpart of monolithic design owing to their lightweight with excellent ballistic resistance [170]. The competing interest comes from the fact that, for the need of today's advanced military and weapon technology, law enforcement applications, etc., monolithic armors appear to be too thick and heavy, affecting their mobility and flexibility. On the other hand, composite armor, which has the potential to overcome these drawbacks, can be made lightweight. This forms an important scope of research in the context of varied defense and civil applications [171, 172]. In engineering new types of composite armors, their material constituents play an important role in translating the kinetic energy of the impacts into internal energy, which has been explored by many researchers [13, 173, 174, 175, 176]. Generally, a composite armor is made up of bulk hard layered ceramic front panel and polymer-based rear panel joined by adhesives. The ceramic panel functions as a retarder of the impacted object penetration [177]. It transmits the shock wave, which is absorbed by the bulk polymer panel. Even if the impact object does not pierce the armor, in the absence of an adequate energy dissipation mechanism the shock wave can cause injuries to the wearer's body. Thus the energy-absorbing efficiency of polymer panels is crucial in the design of the armor. This forms the basis for active research on designing appropriate rear panels of the armor. For example, Wilhelm and Bir (2008) [178] have shown, via different case studies, that excessive vest deformation can also cause backface signature (BFS) injuries even if the bullet does not penetrate the vest. They have shown that by putting a threshold limit on the energy density of the impact is an effective measure to prevent BFS injuries.

Experimentally, Park *et. al.* (2012) [179] have quantified the energy dissipated to the backing material of a soft body armor panel. They have shown that the energy absorption per unit dent volume of the backing material varies linearly with impact velocity. Recently, Bajya *et. al.* (2020) [180] have shown an improvement in the energy absorption mechanism of armor backing material using shear thickening fluid (STF), reinforced with kevlar fabrics. They have also studied the size effect of silica nanoparticles (prime composition of STF) on the ballistic performance of armor and concluded that STF-500 (STF composed with 500 nm silica particles) has higher absorption energy in comparison to STF-100, designed with the same number of fabric layers. These works indicate that enhancement in the energy-absorbing mechanism of the polymer panel is crucial for an efficient design of the armors.

In this context, we would like to recall that metamaterials have certain clear advantages over their classical counterparts with the above-mentioned features desired from protective armors [181, 95]. While metamaterials are still among the developing areas of research, its journey actually started in the context of electromagnetism way back in 1968 with the visionary article by Veselago [182]. Over the last couple of decades, there have been a series of exciting works on metamaterials in different fields ranging from electromagnetics and optics to mechanics showcasing interesting properties, e.g. negative Poisson's ratio [36, 183], negative refractive index [184], frequency bandgap [95] etc. We believe that the efficiency of ceramic polymer composite armors can be increased drastically if we replace the bulk polymer panel with a metamaterial whose constituent chemical composition is a polymer. The present study is geared towards investigating this aspect. A major challenge in such a study is to incorporate microstructure details of the metamaterials in finite element-based solutions of the continuum laws. Note that metamaterials derive such non-intuitive properties mostly from their microstructures, i.e. geometry, size, and shape of the microstructures. Hence we can not ignore the microstructure details in modeling. The task involves extreme computational overhead which is not possible to afford for the large engineering scale of our interest. We need an efficient strategy with reduced degrees of freedom to analyze metamaterials. The usual rigid rotating square approximation-

based approaches are not accurate enough and may lead to erroneous results [185]. We need an appropriate coarse-grained description of the metamaterial that incorporates microstructure information and the chemical composition of its constituent material. With this motivation, we propose an energetic description of the polymer metamaterial via a finite element-based coarse-graining strategy. The reduced order model is utilized to get through-thickness transmission losses, which clearly demonstrates that appropriately designed polymer metamaterials can be much more efficient than monolithic polymer panels in absorbing the propagating shock waves. Via transmission loss diagrams, we basically check the frequency contents in the elastic wave that get heavily attenuated while propagating through the metamaterial.

Here we propose a novel high-energy absorbing design for a backing panel of armors with polymer-based mechanical metamaterial (PMM) which can be achieved via additive manufacturing (AM) technology. For analyzing PMM, we also provide a novel FEM-based coarse-grained description of the model to capture its mechanical behavior. Usually coarse graining is used in the context of molecular dynamics simulations. Here the phrase "Coarse-grain" is used contextually, which basically means a simplified model with reduced degrees of freedom, yet capable of capturing the overall behaviour of the structure accurately. The simulations are based on the simplified model derived from the energetic description of the whole structure. Thus our objective is twofold. First, we illustrate that polymer metamaterial panel (PMP, a schematic representation is given in Fig. 5.1) has high energy absorbing capacity than its monolithic counterpart, i.e. solid polymer panel (SPP) which has the same chemical composition. This is shown by studying the through-thickness transmission losses in elastic waves while propagating through the PMP and SPP. Second, to bypass the huge computational requirement involved in the micromechanical model of PMP, we propose a FEM-based coarse-grained formulation, which captures its energetics with reduced degrees of freedom. Specifically, we model the fiber elements of PMP as flexible 3D frame elements to avoid the erroneous approximations involved with the assumption of a rigid rotating square mechanism. Since the mechanics of the metamaterials is greatly influenced by their microstructural geometry, the contribu-

tion from the connecting filaments of the fiber elements are also accounted for in the energetics of the micromechanical model.

A detailed mathematical formulation of the coarse-grained methodology is given in section 5.2. Section 5.3 shows the validation of the coarse-grained formulation solving a test example and comparing it with the classical finite element-based continuum solution. The energy absorption efficiency of polymer metamaterial panel (PMP) in comparison to monolithic solid polymer panel (SPP) is shown by comparing transmission losses in section 5.4.

5.2 Mathematical formulation for coarse-grained description

En route to avoiding extreme computation involved in a finite element-based solution of the continuum equations, we need a coarse-graining methodology to incorporate the microstructure information and chemical composition of the polymer metamaterial in our coarse-grained description. A schematic representation of the proposed polymer metamaterial panel (PMP) is shown in Fig. 5.1. The abbreviation for dimensions of each modeled fiber element is as shown in the figure, i.e., length (L), thickness (d), and width (w) of each fiber element and thickness of the connector/hinge-like joint (l). We propose a coarse-grained formulation based on the energetics of the model to capture the mechanics of the metamaterial. In the process, the PMP fiber elements are modeled as flexible 3D frame elements and since micro details of metamaterial are essential, their connecting filaments which act as connectors/hinge-like joints are modeled based on rotating square mechanism capturing their energetics in bending, shear and stretch.

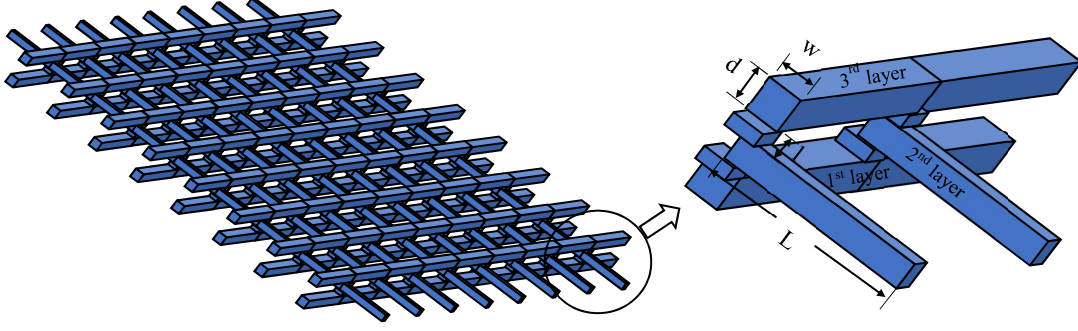


Figure 5.1: Schematic representation of a 3 layered polymer metamaterial panel (PMP).

We discretize each fiber element as two noded element and express the energetics of i^{th} fiber element (E_{f_i}) as given in Eq. (5.1).

$$E_{f_i} = \frac{1}{2} \mathbf{q}_i^T \mathbf{k}_i \mathbf{q}_i \quad (5.1)$$

where $\mathbf{q}_i = [\mathbf{q}_{s_i} \quad \mathbf{q}_{e_i}]^T$ captures the displacements along the degrees of freedom of the start and end connecting nodes, s_i and e_i , respectively, of i^{th} fiber element; $\mathbf{q}_{j_i} = [u_{jx} \quad u_{jy} \quad u_{jz} \quad \theta_{jx} \quad \theta_{jy} \quad \theta_{jz}]$ for $j = \{s, e\}$; u and θ being translational and rotational deformations, respectively along the directions x , y and z . \mathbf{k}_i is the classical stiffness matrix of i^{th} frame element. Element stiffness matrix, \mathbf{k}_i for a frame element in 3D space considering axial rigidity $(EA)_i$, flexural rigidities, $(EI_z)_i$ and $(EI_y)_i$ for bending about the local z and y , and torsional rigidity $(GJ)_i$ is given by Eq. (5.2).

$$\mathbf{k}_i = \begin{bmatrix} k_a & k_c^T \\ k_c & k_b \end{bmatrix} \quad (5.2)$$

where k_a , k_b and k_c is given by Eq. (5.3), (5.4) and (5.5).

$$k_a = \begin{bmatrix} \alpha_i & 0 & 0 & 0 & 0 & 0 \\ 0 & \frac{12\delta_{zi}}{L_i^2} & 0 & 0 & 0 & \frac{6\delta_{zi}}{L_i} \\ 0 & 0 & \frac{12\delta_{yi}}{L_i^2} & 0 & \frac{-6\delta_{yi}}{L_i} & 0 \\ 0 & 0 & 0 & \epsilon_i & 0 & 0 \\ 0 & 0 & \frac{-6\delta_{yi}}{L_i} & 0 & 4\delta_{yi} & 0 \\ 0 & \frac{6\delta_{zi}}{L_i} & 0 & 0 & 0 & 4\delta_{zi} \end{bmatrix} \quad (5.3)$$

$$k_b = \begin{bmatrix} \alpha_i & 0 & 0 & 0 & 0 & 0 \\ 0 & \frac{12\delta_{zi}}{L_i^2} & 0 & 0 & 0 & \frac{-6\delta_{zi}}{L_i} \\ 0 & 0 & \frac{12\delta_{yi}}{L_i^2} & 0 & \frac{6\delta_{yi}}{L_i} & 0 \\ 0 & 0 & 0 & \epsilon_i & 0 & 0 \\ 0 & 0 & \frac{6\delta_{yi}}{L_i} & 0 & 4\delta_{yi} & 0 \\ 0 & \frac{-6\delta_{zi}}{L_i} & 0 & 0 & 0 & 4\delta_{zi} \end{bmatrix} \quad (5.4)$$

$$k_c = \begin{bmatrix} -\alpha_i & 0 & 0 & 0 & 0 & 0 \\ 0 & \frac{-12\delta_{zi}}{L_i^2} & 0 & 0 & 0 & \frac{-6\delta_{zi}}{L_i} \\ 0 & 0 & \frac{-12\delta_{yi}}{L_i^2} & 0 & \frac{6\delta_{yi}}{L_i} & 0 \\ 0 & 0 & 0 & -\epsilon_i & 0 & 0 \\ 0 & 0 & \frac{-6\delta_{yi}}{L_i} & 0 & 2\delta_{yi} & 0 \\ 0 & \frac{6\delta_{zi}}{L_i} & 0 & 0 & 0 & 2\delta_{zi} \end{bmatrix} \quad (5.5)$$

Where,

- E is elastic modulus of the frame element
- A is the cross-sectional area
- I is the second moment of area
- G is shear modulus
- J is polar moment of inertia
- $\alpha_i = \frac{(EA)_i}{L_i}$

- $\delta_{zi} = \frac{(EI_z)_i}{L_i}$
- $\delta_{yi} = \frac{(EI_y)_i}{L_i}$
- $\epsilon_i = \frac{(GJ)_i}{L_i}$

We consider the connector to be flexible and its mechanics is characterized by adjoining fiber elements. The mechanism involved is characterized by the following description.

- [1] *Connector energetics*: This is described in most general way when we allow them for pure bending, shear and stretching. Each connector connects two adjacent flexible fibers, i.e., one fiber in the bottom layer to another fiber on top of it as shown in Fig. 5.1. The governed stiffnesses (C_b , C_{sh} and k for bending, shear and stretching, respectively) in linear elastic regime are calibrated by finite element based simulations following their detailed geometry.
- [2] *Parameters in energetic expression*: To express the energetics of the j^{th} connector, we use translational (u_j) and rotational (θ_j) displacements against external forcing on i^{th} fiber element as shown in Fig. 5.2. To account for shear deformations of the connectors, the shear angle (ψ_j) is also considered. We express the bending energy as $\frac{1}{2}C_b (\theta_i - \theta_{i+a})^2$, the shear energy as $\frac{1}{2}C_{sh} \left(\frac{\theta_i + \theta_{i+a}}{2} - \psi_j \right)^2$ and the stretching energy as $\frac{1}{2}k (u_i)^2$, where i and $i+a$ are the fibers connected by j^{th} connector; a being number of discretized fiber elements in one layer of PMP. It should be noted that in global coordinates $\{s_j, e_j\} = \{e_i, s_{i+1}\}$.
- [3] *Determination of stiffnesses*: As mentioned earlier, C_b , C_{sh} and k are calibrated via full scale finite element simulations of the 3D continuum equations of the system following exact geometry. Fig. 5.2 shows the loading pattern to determine these stiffnesses. For simulation of each connector with thickness, $l=0.01$ mm, effective dimensions of connecting fibers are chosen as length, $L=0.25$ mm, width, $w=0.1$ mm and thickness, $d=0.1$ mm.

Pure bending is implemented via counter rotations: $\theta_i = -\theta_{i+1}$ while $u_i = \psi_j = 0$

(Fig. 5.2(a)).

Pure shear is implemented via relative horizontal motion: $\psi_j \neq 0$ while $\theta_i = \theta_{i+1} = u_i = 0$ (Fig. 5.2(b)).

Pure stretch is implemented via relative vertical motion: $u_i \neq 0$ while $\theta_i = \theta_{i+1} = \psi_j = 0$ (Fig. 5.2(c)).

To determine C_b , increasing moment (M) is applied along y-direction on both the adjacent fibers as shown in Fig. 5.2(a), and corresponding rotational deformations (θ_j) on the opposite sides of j^{th} connector are measured. The slope of the plot between M and relative rotational deformation along z-direction ($\theta_{sz} - \theta_{ez}$) gives elastic bending coefficient of the connector in z-direction; s and e denote the starting and ending node of the j^{th} connector. Thus, bending coefficient (C_b) recovered from the plot, M versus $\theta_{sz} - \theta_{ez}$, has a value of 0.03 N · m. Similarly, C_{sh} is determined by applying load P in two opposite directions on the adjacent fibers as shown in Fig. 5.2(b) and capturing θ_{sy} , θ_{ex} and ψ_j , where $\psi_j = \frac{u_{sx} - u_{ey}}{l}$. Shear coefficient is the slope of plot between different P and corresponding $\frac{\theta_{sy} + \theta_{ex}}{2} - \psi_j$ values. The recovered shear coefficient (C_{sh}) from the plot, P versus $\frac{\theta_{sy} + \theta_{ex}}{2} - \psi_j$, has a value of 123.18 N. Stretch coefficient is determined by gradually pulling the adjacent fibers in opposite directions as shown in Fig. 5.2(c) and measuring the relative displacement of the sides of the connector ($u_{sx} - u_{ex}$). The slope of the plot obtained by varying P and measuring corresponding $u_{sx} - u_{ex}$ gives the stretch coefficient. The recovered stretch coefficient (k) from the plot, P versus $u_{sx} - u_{ex}$, has a value of 1.19×10^7 N/m. Thus, results of FEM simulations for elastic coefficients of the connectors in bending, shear and stretch, in linear elastic regime gives the values as $C_b = 0.03$ N · m, $C_{sh} = 123.18$ N and $k = 1.19 \times 10^7$ N/m, respectively. Using the numerical values of these coefficients, the energetics of j^{th} connector, E_{c_j} in 3D space is expressed as in Eq. (5.6).

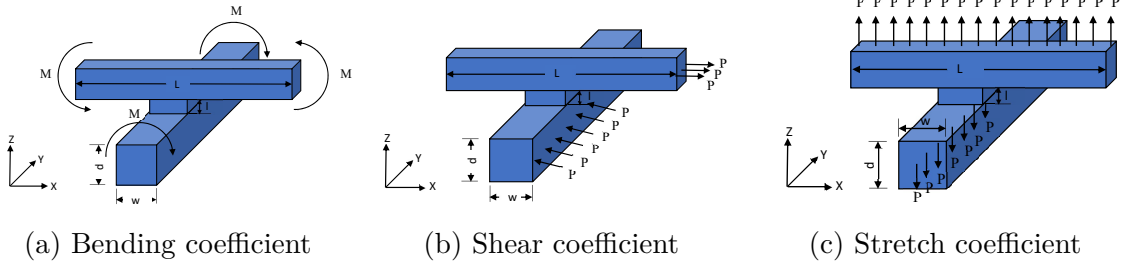


Figure 5.2: FEM simulations to obtain elastic coefficients of connector filaments, i.e., (a) bending, (b) shear, and (c) stretch. Dimensions $L=0.25$ mm, $l=0.01$ mm and $w=d=0.1$ mm.

$$\begin{aligned}
 E_{c_j} = & \frac{1}{2} C_{sh} \left(\frac{\theta_{sy,j} + \theta_{ex,j}}{2} - \frac{u_{sx,j} - u_{ey,j}}{l} \right)^2 + \frac{1}{2} C_{sh} \left(\frac{\theta_{sx,j} + \theta_{ey,j}}{2} - \frac{u_{sy,j} - u_{ex,j}}{l} \right)^2 \\
 & + \frac{1}{2} k (u_{sz,j} - u_{ez,j})^2 + \frac{1}{2} C_b (\theta_{sx,j} - \theta_{ex,j})^2 + \frac{1}{2} C_b (\theta_{sy,j} - \theta_{ey,j})^2 \\
 & + \frac{1}{2} C_b (\theta_{sz,j} - \theta_{ez,j})^2
 \end{aligned} \tag{5.6}$$

Combining Eq. (5.1) and Eq. (5.6), the total elastic energy (E_e) of the system is expressed as in Eq. (5.7), where n_1 and n_2 represents total number of fiber elements and total number of connectors, respectively.

$$E_e = \sum_{i=1}^{n_1} E_{f_i} + \sum_{j=1}^{n_2} E_{c_j} \tag{5.7}$$

Kinetic energy (E_k) of the system may be written as given in Eq. (5.8).

$$E_k = \sum_{i=1}^{n_1} \frac{1}{2} \dot{\mathbf{q}}_i^T \mathbf{m} \dot{\mathbf{q}}_i \tag{5.8}$$

Accordingly, Lagrangian, $\mathcal{L} = E_k - E_e$, and the Euler-Lagrangian equation, i.e., the equation of motion may be written as in Eq. (5.9).

$$\frac{\partial \mathcal{L}}{\partial \mathbf{q}_i} - \frac{\partial}{\partial t} \left(\frac{\partial \mathcal{L}}{\partial \dot{\mathbf{q}}_i} \right) = 0 \tag{5.9}$$

Since each fiber element is discretized into two noded element, Eq. (5.9) gives 12 number of equations of motion (6 dof at each node; 3 translational and 3 rotational). Thus, we arrive at $12N$ number of equations of motion, where N is the total number of discretized elements of the system. Including the contribution from external force vector, these equations, when rearranged, can be written in frequency domain as given in Eq. (5.10) where \mathbf{K} and \mathbf{M} are global stiffness and mass matrices, respectively, \mathbf{U} is assembled displacement vector and \mathbf{F} is the applied external force vector.

$$(\mathbf{K} - \omega^2\mathbf{M})\mathbf{U} = \mathbf{F} \quad (5.10)$$

In frequency domain, we compute \mathbf{U} by varying ω from Eq. (5.10) and represent transmission loss by Eq. (5.11); where u_i is deformation at incident node and u_o is deformation at node opposite of u_i through the thickness of PMP.

$$loss = 10 \log_{10} \frac{u_o^2}{u_i^2} \quad (5.11)$$

5.3 Validation of coarse-grained methodology

For validation purposes of the proposed coarse-grained methodology presented in section 5.2, its comparison is made with finite element simulation under similar conditions. A two-layered polymer metamaterial is fixed at its bottom layer as shown in Fig. 5.3. Unless otherwise specified, the PMP has material properties as Elastic modulus, $E = 152$ GPa, Poisson's ratio, $\mu = 0.35$ and density, $\rho = 1467$ kg/m³. The Length of each fiber element, L is taken as 0.25 mm, width, w , and thickness, d as 0.1 mm and 0.1 mm, respectively. The connector (hinge-like joint) thickness is taken as 0.01 mm. The metamaterial is subjected to a pulling force P in the form of a uniformly distributed load on selected fiber elements as shown in the figure. The force P is increased gradually and corresponding displacement is recorded.

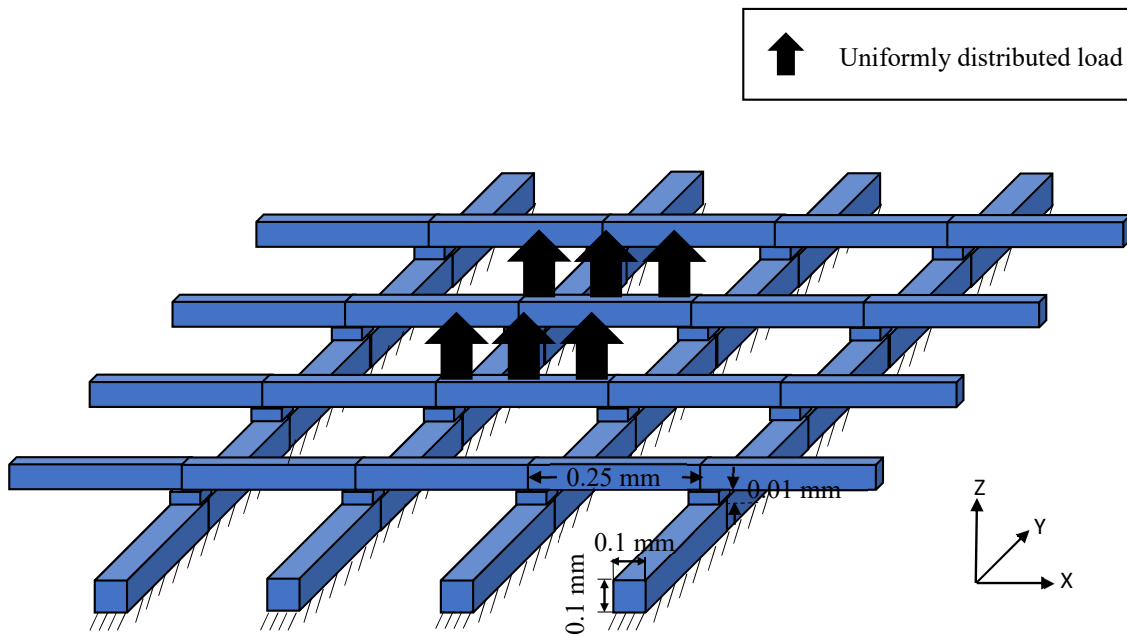


Figure 5.3: A two-layered PMP of armor with a dimension of each fiber element as, $L = 0.25$ mm, $w = d = 0.1$ mm and connector as, $l = 0.01$ mm, subjected to pulling by a uniformly distributed load on selected fibers.

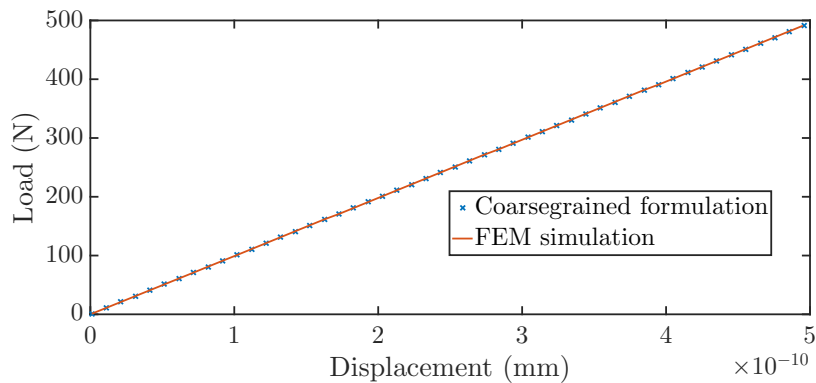


Figure 5.4: Load Vs displacement plot for a two-layered PMP (corresponding to fig. 5.3), simulated using full-scale finite element analysis (continuous marked line) and proposed coarse-grained formulation (star marked line).

The simulation results showing a comparison of both the methods, i.e., finite element method and the proposed coarse-grained method is given in Fig. 5.4. The plot shows that the coarse-grained formulation is in excellent agreement with the full-scale finite element simulation of 3D continuum laws. The volume of unit cell of PMP is

0.015 mm^3 approximately, whereas the homogeneous volume of the unit cell (for the detailed analysis) is 0.01875 mm^3 , which is higher than the simplified model. Thus, there is approximately 20 % reduction in the volume via simplified model, yet the model is able to capture the response accurately.

5.4 Numerical results and discussion

In this section, we demonstrate different numerical results of polymer metamaterial via transmission losses following coarse-grained solutions, of which a detailed explanation is given in section 5.2. The results are computed using in-house code developed on MATLAB 2019a. We first compare a 2 mm thick PMP based armor design to its solid counterpart, i.e., SPP of the same thickness under similar loading conditions. On arriving at a choice, we next examine the size effect of the microstructure of PMP on attenuating the propagation of elastic/stress waves via transmission losses. We specifically study the effect of increasing the number of layers and refining the fiber length and thickness along each layer of PMP.

5.4.1 Comparison of polymer metamaterial with its solid counterpart

To compare the energy absorbing capacity of PMP and its solid counterpart, i.e., bulk single polymer panel (SPP), we compute the transmission losses in both cases when an elastic wave from object impact is propagating through it. A 10-layered PMP is numerically analyzed using the coarse-grained formulation as demonstrated in section 5.2 while the bulk polymer panel, i.e., SPP is numerically analyzed using the finite element approach. Each layer of PMP is having an effective thickness of 0.1 mm, thus making a total thickness of PMP 2 mm (along the z-direction), and each fiber in the impact influence zone, of dimension 10 mm \times 10 mm in both x and y direction, is modeled using 1 mm frame element. For comparison purposes, the SPP is also chosen to have the same thickness, i.e., 2mm. Both the models, i.e., PMP and

SPP are studied for an elastic wave generating from an impact of 50 N in the frequency domain.

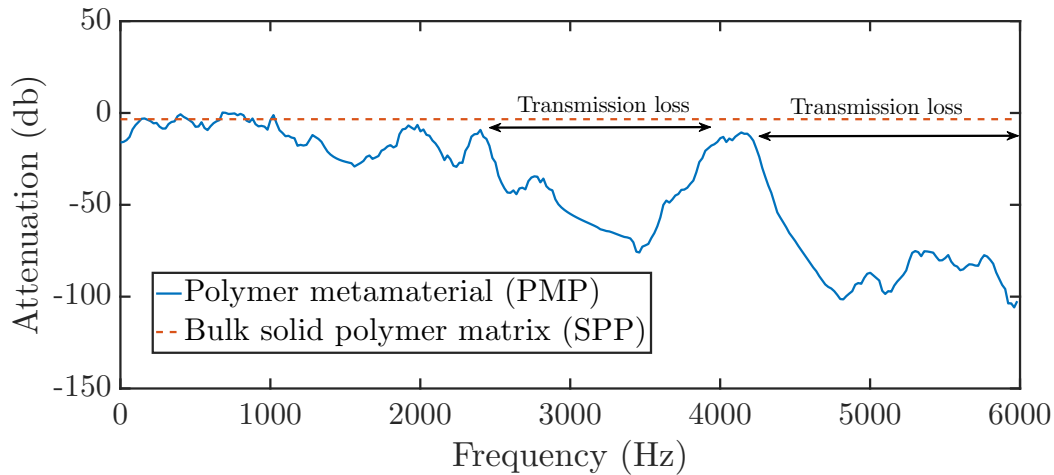


Figure 5.5: Comparison of transmission losses in polymer metamaterial (PMP) and its solid counterpart bulk polymer matrix (SPP), both having thicknesses of 2 mm.

Fig. 5.5 shows the attenuation of propagating elastic waves in PMP and SPP via transmission losses. Clearly, PMP shows large attenuation of elastic wave propagation in comparison to SPP under similar conditions. Where SPP can only attenuate the wave upto approximately 3 dB (see the dotted line of Fig 5.5), PMP on the other hand achieves large attenuation of wave propagation in the range of 2.5 kHz-4 kHz and beyond. This proves that SPP if is replaced with a PMP, the energy-absorbing capacity of the armor system can be enhanced significantly. Moreover, since the order of attenuation is very large for PMP in comparison to SPP, for a specific armor application the thickness of PMP can be varied by varying the number of PMP layers. This serves as an advantage of having a much lighter weight than the SPP-based design and also enhances defense system mobility.

5.4.2 Effect of an increasing number of layers in polymer metamaterial

On proving that PMP has high energy absorbing capacity in comparison to SPP, we further study the size effect of PMP on attenuating the elastic wave. For this purpose, we numerically simulate 2 models, i.e., the 4-layered and 8-layered PMP models keeping the fiber length and thickness the same in each layer. Each fiber is having a thickness of 0.1 mm (along the z-direction) and the impact influence zone is taken the same as in the previous test results, i.e., 10 mm \times 10 mm (x and y direction). Since in the earlier section we have shown that the thickness of PMP can be reduced by reducing the number of layers to a greater extent in comparison to SPP for a similar armor application, in this section we use a lesser number of layers, i.e., 4 and 8 to study the wave attenuation for thinner PMP design.

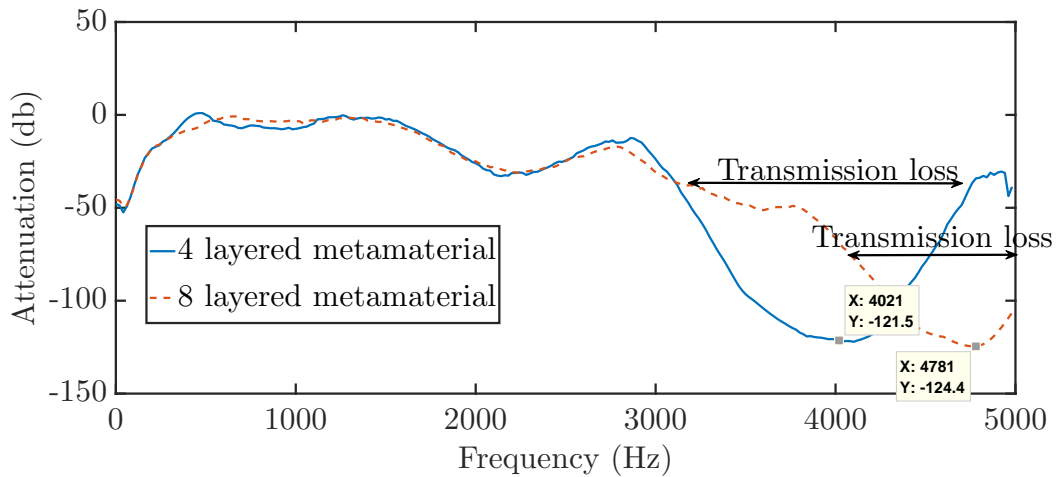


Figure 5.6: Comparison of transmission losses in a 4-layered and 8-layered polymer metamaterial (PMP).

Fig. 5.6 shows the elastic wave attenuation in a 4 and 8-layered PMP. The former PMP model shows transmission losses in the frequency range of 3.5 kHz - 4.5 kHz, while the latter shows transmission losses in a slightly higher frequency range, i.e., above 4.5 kHz frequency. Thus the number of layers in a PMP-based design of armor is also an essential parameter that can be regulated to achieve desirable properties

of the defense system based on the striking velocities of the impact. However, one should note that the attenuation difference in 4 and 8-layered models is not more than approximately 3 dB (121.5 dB for 4-layered and 124.4 dB for 8-layered), i.e., around 2.5 %.

5.4.3 Effect of varying fiber length and thickness in the microstructural geometry of polymer metamaterial

To further investigate the effect of varying fiber length and thickness on elastic wave attenuation, we numerically simulate a 4 layered PMP model. This model is tested with two types of arrangements for the length and thickness of the fiber element, keeping the dimensions of the influence zone the same, i.e, $10 \text{ mm} \times 10 \text{ mm}$. Within the influence zone, one arrangement of finely spaced fiber elements is considered and the other one is taken as coarsely spaced fiber elements. For simulation purposes, we keep the length to thickness ratio of each fiber element the same. Figure 5.7 shows the wave attenuation in both types of arrangements. The figure depicts that the finer arrangement of the fiber elements in the microstructural geometry of PMP attenuates the propagating wave to a large extent in comparison to the coarser arrangement. The former arrangement of PMP shows better wave attenuation than the latter arrangement in the frequency range of 2 kHz-2.2 kHz and again in the range of 3.3 kHz-4.4 kHz. Although the finer arrangement shows better attenuation, this may again increase the computational time. Thus, there can be a trade-off between the fiber arrangement in PMP design and the required computational time based on the importance of the defense structure.

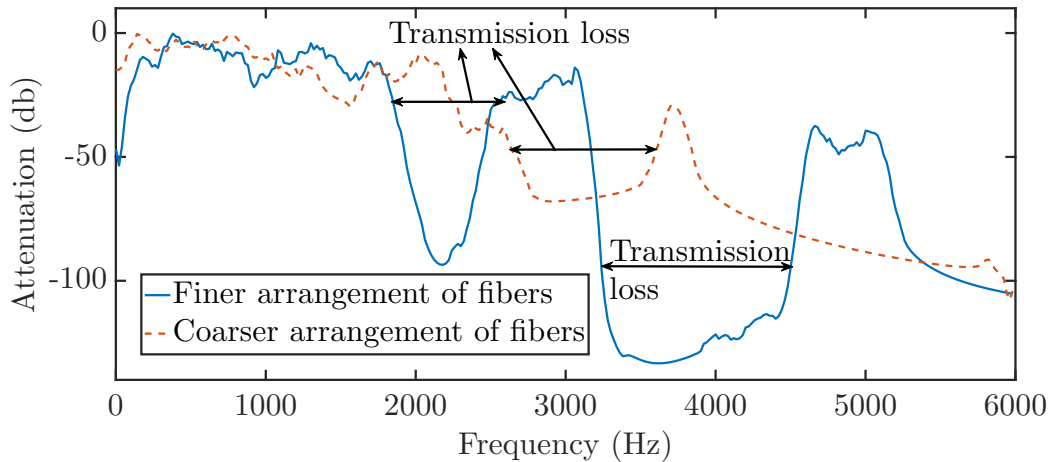


Figure 5.7: Comparison of transmission losses in a 4-layered PMP design of armor with finer and coarser arrangement of fibers in its microstructure.

5.5 Summary

In the present study, we have shown that the energy-absorbing efficiency of composite armors can be drastically improved if the bulk polymer matrix is replaced by an appropriate metamaterial whose constitute chemical composition is a polymer. The finite element-based solution of 3D continuum laws for metamaterials requires huge computational power, thus making the traditional route infeasible for analyzing metamaterials for engineering applications like armor design. At the same time, we cannot ignore the microstructural geometries of the metamaterials from which they derive their nonintuitive properties. Thus, to bypass the huge computational requirement which comes from finite element-based solutions, we have proposed a novel coarse-grained methodology to analyze metamaterials for armor design. In this coarse-grained formulation, the PMP behavior is analyzed by capturing its energetics with reduced degrees of freedom. Since microstructural geometries of metamaterial are also influential, the contribution from the energetics of the connecting filaments of PMP fiber is also accounted for in the whole micromechanical model. Specifically, the PMP fiber elements were modeled as 3D frame elements and their connectors were modeled by capturing their linear elastic behavior in bending, shear, and stretching.

The elastic coefficients of connectors are obtained via finite element-based simulations whose detailed description is given in section 5.2.

The PMP of armor has a great energy-absorbing capacity than its solid counterpart SPP. This is shown by comparing through-thickness transmission losses in elastic/stress waves propagating through a 2 mm thick PMP and SPP of armor. PMP achieves large attenuation in wave propagation in the range of 2.5 kHz-4 kHz and beyond, in comparison to 3 dB attenuation of SPP-designed armor. The size effect of metamaterial in PMP is also influential in attenuating elastic/stress waves, i.e., with increasing the number of layer in the metamaterial, stress waves further attenuate considerably. An 8-layered PMP attenuates elastic waves approximately 2.5 % more than a 4-layered PMP, both having thicknesses of 0.1 mm for each layer. However, transmission loss is obtained in a slightly higher frequency domain for the 8-layered than for the 4-layered PMP. This necessitates proper tuning to achieve the number of PMP layers for desirable properties of the defense system based on the striking velocities of the impact. The influence of the size effect of PMP is further shown by comparing the simulations on a 4-layered PMP with finely and coarsely spaced fiber elements. Better attenuation is obtained with the finer arrangement of fiber elements in comparison to the coarser arrangement. While this study shows a novel aspect of designing composite armor using metamaterials, it has many scopes for further research. Since this study is conducted in a linear regime, one would like to explore the non-linearity involved in the model. One may also be interested in investigating the behavior of PMP in the failure regime.

Chapter 6

Conclusions and Future Work

This thesis primarily investigates the effect of internal geometries on the macroscopic deformation of a solid. The mechanical response of a solid body does not only depend on its elastic properties but also on the subsystem's internal geometry and its arrangements. This research work uses the concept of metamaterials and shows that tweaking the geometrical parameters of a unit cell of periodic media affects the bulk overall response such as frequency bandgap, stress wave attenuation, energy absorption capability, etc. The length scale of internal geometry's dimensions may vary from nano-meter to meter depending on the specific applications. In particular, we have shown that such designs are important for applications in developing efficient protective structures such as seismic shields and body armor.

6.1 Conclusions

From the present study the following conclusions are drawn:

- [1] Firstly, we noticed the importance of internal geometry to further enhance the filtering effects from the propagating wave in a periodic solid medium. By changing the internal geometries, it is observed that seismic waves can get weakened to a great extent. Further, tilting the junctions between the inertial resonators and the bulk medium of seismic metamaterials (SMs), a torsional mode opens up a frequency bandgap in the upper region of the frequency spectrum. The addi-

tional stopbands at higher frequencies might find applications in the suppression of ground vibrations induced by traffic.

- [2] For SMs, inclusions having a square cross-section with sides aligned with the square lattice gives a wider bandgap in comparison to any other cross-sections for the same substitution ratio of the constituent material. This has been demonstrated by computing transmission losses in addition to the dispersion curves for different microstructure geometries of the SM.
- [3] By mixing stress-free and clamped boundary conditions (where the bottoms of SMs are clamped), we observe zero frequency bandgaps. Practically, clamping the bottom is possible if the steel columns are embedded in bedrock or a layer of gravel. Such designs are important for tall structures whose natural frequencies are close to zero.
- [4] As fabricating large volumes of steel is not feasible, both economically and technically, we have shown that concrete can also be used to design inclusions for large wave attenuations in very loose soil. Since concrete is easily mouldable in desired shapes, and more cost-effective than steel, it will help in the industrial scaling up of technology in such designs.
- [5] As very soft soil is not suitable for construction, an architecture of SM is prescribed, with concrete inclusions in a narrow strip of very soft soil matrix surrounding the protected region. The rest portion of the soil can be in its natural state.
- [6] We have observed that square cross-section inclusions with an initial prestressing force can also be used to design high-performance engineered composites having simultaneous fracture toughness and fracture strength. Such composites will find applications in designing efficient protective armor front panels, where ceramic inclusions are introduced periodically in the steel matrix.
- [7] A compressive prestressing force applied to the hard inclusions shows significant improvement in the fracture toughness and fracture strength. A similar force

is applied to the soft inclusions showing even higher fracture toughness but a negligible increase in fracture strength. Thus, where fracture toughness and fracture strength are equally important, we recommend hard inclusions whereas soft inclusions will find application where only fracture toughness is predominately important.

- [8] We have observed that cubic voids arranged periodically in a polymer matrix can drastically improve the energy-absorbing efficiency of the material. Such designs are useful in developing efficient back panels of a composite armor whose chemical composition is a polymer.
- [9] A Finite Element-based solution of 3D continuum laws for designs incorporating internal geometries requires huge computational power. Thus, to bypass this a novel coarse-grained methodology is proposed (with reduced dofs) to analyze such structures.
- [10] It is observed that a polymer-based metamaterial panel design for a backing panel of armors shows large attenuation of the propagating wave throughout the frequency spectrum in comparison to its solid counterpart.

6.2 Future Research Directions

The study of the arrangement of internal geometry and its effect on the macroscopic deformation of a solid body is a new idea and there are a lot of scopes for future studies. Some of them are listed below.

- [1] We have assumed linear elastic materials for SMs in our study. However, it would be interesting to investigate the performance of SMs in the context of material and geometric non-linearity; soil often shows a significant amount of plastic deformation.
- [2] It would be interesting to consider a geometrically interlocking shape of the inclusion such as osteomorphic brick to explore the effect of interlocking geome-

try in the presence of pre-stressed inclusions on the macroscopic deformation of solid.

- [3] Crack branching and coalescence of cracks in a periodic media is an interesting topic to explore.
- [4] Effects of internal geometries in the nonlinear regime leading to permanent deformation and failure is another aspect which one can focus on.
- [5] Studying the effect of projectile impact on the integrated metamaterial-based front and back panels of armor is yet another interesting aspect.

Bibliography

- [1] JD Clayton. Penetration resistance of armor ceramics: dimensional analysis and property correlations. *International Journal of Impact Engineering*, 85:124–131, 2015.
- [2] Congjie Wei, Chenglin Wu, and Charles Wojnar. Effect of patterned inclusions on the fracture behavior of ceramic composites. *Composites Part B: Engineering*, 172:564–592, 2019.
- [3] John B Pendry, Anthony J Holden, David J Robbins, and WJ Stewart. Magnetism from conductors and enhanced nonlinear phenomena. *IEEE transactions on microwave theory and techniques*, 47(11):2075–2084, 1999.
- [4] Xi-yuan Zhou, Wei-ming Yan, and Run-lin YANG. Seismic base isolation, energy dissipation and vibration control of building structures. *Journal of Building Structures*, 23(2):2–13, 2002.
- [5] HJ Xiang, ZF Shi, SJ Wang, and YL Mo. Periodic materials-based vibration attenuation in layered foundations: experimental validation. *Smart Materials and Structures*, 21(11):112003, 2012.
- [6] Ping Xiang and Akira Nishitani. Seismic vibration control of building structures with multiple tuned mass damper floors integrated. *Earthquake Engineering & Structural Dynamics*, 43(6):909–925, 2014.
- [7] P Scott Harvey Jr and Karah C Kelly. A review of rolling-type seismic isolation: Historical development and future directions. *Engineering Structures*, 125:521–531, 2016.

- [8] Hamidreza Anajafi and Ricardo A Medina. Comparison of the seismic performance of a partial mass isolation technique with conventional tmd and base-isolation systems under broad-band and narrow-band excitations. *Engineering Structures*, 158:110–123, 2018.
- [9] Cristiano Fabrizio, Andrea M de Leo, and Angelo Di Egidio. Tuned mass damper and base isolation: a unitary approach for the seismic protection of conventional frame structures. *Journal of Engineering Mechanics*, 145(4):04019011, 2019.
- [10] Peter Moser and Babak Moaveni. Environmental effects on the identified natural frequencies of the dowling hall footbridge. *Mechanical Systems and Signal Processing*, 25(7):2336–2357, 2011.
- [11] Paul-Remo Wagner, Vasilis K Dertimanis, Eleni N Chatzi, and James L Beck. Robust-to-uncertainties optimal design of seismic metamaterials. *Journal of Engineering Mechanics*, 144(3):04017181, 2018.
- [12] Stéphane Brûlé, EH Javelaud, Stefan Enoch, and Sébastien Guenneau. Experiments on seismic metamaterials: molding surface waves. *Physical review letters*, 112(13):133901, 2014.
- [13] M Wasif Ali, A Mubashar, Emad Uddin, S Waheed Ul Haq, and M Khan. An experimental and numerical investigation of the ballistic response of multi-level armour against armour piercing projectiles. *International journal of impact engineering*, 110:47–56, 2017.
- [14] Roberto Ballarini, Claudio Boni, and Gianni Royer Carfagni. Geometry of sliding lamellae dictates the constitutive properties of nacre-like hierarchical materials. *Journal of the Mechanics and Physics of Solids*, 167:105000, 2022.
- [15] V Macián, V Bermúdez, R Payri, and J Gimeno. New technique for determination of internal geometry of a diesel nozzle with the use of silicone methodology. *Experimental techniques*, 27(2):39–43, 2003.

- [16] DA Zumbrennen, R Viskanta, and FP Incropera. Heat transfer through porous solids with complex internal geometries. *International Journal of Heat and Mass Transfer*, 29(2):275–284, 1986.
- [17] L Buligins, K Thomsen, O Lielausis, E Platacis, and A Poznaks. Internal geometry and coolant choices for solid high power neutron spallation targets. *Nuclear Instruments and Methods in Physics Research Section A: Accelerators, Spectrometers, Detectors and Associated Equipment*, 761:58–68, 2014.
- [18] YJ Cao, WQ Shen, Nicolas Burlion, and Jian-Fu Shao. Effects of inclusions and pores on plastic and viscoplastic deformation of rock-like materials. *International Journal of Plasticity*, 108:107–124, 2018.
- [19] Pascale Penicot, Hervé Muhr, Edouard Plasari, and Jacques Villiermaux. Influence of the internal crystallizer geometry and the operational conditions on the solid product quality. *Chemical Engineering & Technology: Industrial Chemistry-Plant Equipment-Process Engineering-Biotechnology*, 21(6):507–514, 1998.
- [20] Vivek R Jayan, Lekhani Tripathi, Promoda Kumar Behera, Michal Petru, and BK Behera. Prediction of internal geometry and tensile behavior of 3d woven solid structures by mathematical coding. *Journal of Industrial Textiles*, 51(4_suppl):7034S–7055S, 2022.
- [21] Katleen Vallons, Georg Adolphs, Paul Lucas, Stepan V Lomov, and Ignaas Verpoest. The influence of the stitching pattern on the internal geometry, quasi-static and fatigue mechanical properties of glass fibre non-crimp fabric composites. *Composites Part A: Applied Science and Manufacturing*, 56:272–279, 2014.
- [22] Balth van der Pol and MJO Strutt. Ii. on the stability of the solutions of mathieu’s equation. *The London, Edinburgh, and Dublin Philosophical Magazine and Journal of Science*, 5(27):18–38, 1928.

- [23] Maximilian JO Strutt. Eigenschwingungen einer saite mit sinusförmiger massenverteilung. *Annalen der Physik*, 390(2):129–136, 1928.
- [24] Felix Bloch. Über die quantenmechanik der elektronen in kristallgittern. *Zeitschrift für physik*, 52(7):555–600, 1929.
- [25] Joseph Gazalet, Samuel Dupont, Jean-Claude Kastelik, Q Rolland, and B303954707001222 Djafari-Rouhani. A tutorial survey on waves propagating in periodic media: Electronic, photonic and phononic crystals. perception of the bloch theorem in both real and fourier domains. *Wave Motion*, 50(3):619–654, 2013.
- [26] Haruki Watanabe. A proof of the bloch theorem for lattice models. *Journal of Statistical Physics*, 177(4):717–726, 2019.
- [27] A Parrinello, GL Ghiringhelli, and N Atalla. Generalized transfer matrix method for periodic planar media. *Journal of Sound and Vibration*, 464:114993, 2020.
- [28] Hai-Sheng Shu, Xing-Guo Wang, Ru Liu, Xiao-Gang Li, Xiao-Na Shi, Shan-Jun Liang, Li-Huan Xu, and Fu-Zhen Dong. Bandgap analysis of cylindrical shells of generalized phononic crystals by transfer matrix method. *International Journal of Modern Physics B*, 29(24):1550176, 2015.
- [29] Leon Brillouin. *Wave propagation in periodic structures: electric filters and crystal lattices*, volume 2. Dover publications, 1953.
- [30] Jihong Wen, Gang Wang, Dianlong Yu, Honggang Zhao, and Yaozong Liu. Theoretical and experimental investigation of flexural wave propagation in straight beams with periodic structures: Application to a vibration isolation structure. *Journal of Applied Physics*, 97(11):114907, 2005.
- [31] Ardalan Hosseini, Elyas Ghafoori, Masoud Motavalli, Alain Nussbaumer, and Xiao-Ling Zhao. Mode I fatigue crack arrest in tensile steel members using prestressed cfrp plates. *Composite Structures*, 178:119–134, 2017.

- [32] Hong-Jun Xiang and Zhi-Fei Shi. Analysis of flexural vibration band gaps in periodic beams using differential quadrature method. *Computers & structures*, 87(23-24):1559–1566, 2009.
- [33] Hong-Jun Xiang and Zhi-Fei Shi. Vibration attenuation in periodic composite timoshenko beams on pasternak foundation. *Structural Engineering and Mechanics*, 40(3):373–392, 2011.
- [34] John B Pendry, AJ Holden, DJ Robbins, and WJ Stewart. Low frequency plasmons in thin-wire structures. *Journal of Physics: Condensed Matter*, 10(22):4785, 1998.
- [35] Muamer Kadic, Tiemo Bückmann, Robert Schittny, and Martin Wegener. Metamaterials beyond electromagnetism. *Reports on Progress in physics*, 76(12):126501, 2013.
- [36] Roderic Lakes. Foam structures with a negative poisson’s ratio. *Science*, 235(4792):1038–1040, 1987.
- [37] Zachary G Nicolaou and Adilson E Motter. Mechanical metamaterials with negative compressibility transitions. *Nature materials*, 11(7):608–613, 2012.
- [38] H MA Kolken and AA Zadpoor. Auxetic mechanical metamaterials. *RSC advances*, 7(9):5111–5129, 2017.
- [39] Zhenwei Wang, Congcong Luan, Guangxin Liao, Jiapeng Liu, Xinhua Yao, and Jianzhong Fu. Progress in auxetic mechanical metamaterials: structures, characteristics, manufacturing methods, and applications. *Advanced Engineering Materials*, 22(10):2000312, 2020.
- [40] Kaikai Che, Chao Yuan, Jiangtao Wu, H Jerry Qi, and Julien Meaud. Three-dimensional-printed multistable mechanical metamaterials with a deterministic deformation sequence. *Journal of Applied Mechanics*, 84(1), 2017.

- [41] Xiaojun Tan, Shuai Chen, Bing Wang, Shaowei Zhu, Linzhi Wu, and Yuguo Sun. Design, fabrication, and characterization of multistable mechanical metamaterials for trapping energy. *Extreme Mechanics Letters*, 28:8–21, 2019.
- [42] Bastiaan Florijn, Corentin Coulais, and Martin van Hecke. Programmable mechanical metamaterials. *Physical review letters*, 113(17):175503, 2014.
- [43] Hongbin Fang, Shih-Cheng A Chu, Yutong Xia, and Kon-Well Wang. Programmable self-locking origami mechanical metamaterials. *Advanced Materials*, 30(15):1706311, 2018.
- [44] Shahram Janbaz, Molly McGuinness, and Amir A Zadpoor. Multimaterial control of instability in soft mechanical metamaterials. *Physical Review Applied*, 9(6):064013, 2018.
- [45] Deepak Sharma, Somashekhar S Hiremath, and Nagesha Bommanahalli Kenchappa. Bio-inspired ti-6al-4v mechanical metamaterials fabricated using selective laser melting process. *Materials Today Communications*, 33:104631, 2022.
- [46] Li Xin, Yu Siyuan, Liu Harry, Lu Minghui, and Chen Yanfeng. Topological mechanical metamaterials: A brief review. *Current Opinion in Solid State and Materials Science*, 24(5):100853, 2020.
- [47] Andrea Colombi, Philippe Roux, Sebastien Guenneau, Philippe Gueguen, and Richard V Craster. Forests as a natural seismic metamaterial: Rayleigh wave bandgaps induced by local resonances. *Scientific reports*, 6(1):1–7, 2016.
- [48] Marco Miniaci, Anastasiia Krushynska, Federico Bosia, and Nicola M Pugno. Large scale mechanical metamaterials as seismic shields. *New Journal of Physics*, 18(8):083041, 2016.
- [49] Yu Ming Luo, Ting Ting Huang, Yi Zhang, Hang Hang Xu, Yi Min Xie, and Xin Ren. Novel meter-scale seismic metamaterial with low-frequency wide bandgap for lamb waves. *Engineering Structures*, 275:115321, 2023.

- [50] JD Achenbach. Wave motion in elastic solids amsterdam, 1973.
- [51] Pengpeng Shi. Singular integral equation method for 2d fracture analysis of orthotropic solids containing doubly periodic strip-like cracks on rectangular lattice arrays under longitudinal shear loading. *Applied Mathematical Modelling*, 77:1460–1473, 2020.
- [52] PGBB Shanmugavel, GB Bhaskar, M Chandrasekaran, PS Mani, and SP Srinivasan. An overview of fracture analysis in functionally graded materials. *European Journal of Scientific Research*, 68(3):412–439, 2012.
- [53] Fabian Lipperman, Michael Ryvkin, and Moshe B Fuchs. Fracture toughness of two-dimensional cellular material with periodic microstructure. *International Journal of Fracture*, 146(4):279–290, 2007.
- [54] Ted Belytschko, Nicolas Moës, Shuji Usui, and Chandu Parimi. Arbitrary discontinuities in finite elements. *International Journal for Numerical Methods in Engineering*, 50(4):993–1013, 2001.
- [55] Pierre-Olivier Bouchard, François Bay, and Yvan Chastel. Numerical modelling of crack propagation: automatic remeshing and comparison of different criteria. *Computer methods in applied mechanics and engineering*, 192(35-36):3887–3908, 2003.
- [56] Natarajan Sukumar, David L Chopp, Nicolas Moës, and Ted Belytschko. Modeling holes and inclusions by level sets in the extended finite-element method. *Computer methods in applied mechanics and engineering*, 190(46-47):6183–6200, 2001.
- [57] James MW Brownjohn, Alessandro De Stefano, You-Lin Xu, Helmut Wenzel, and A Emin Aktan. Vibration-based monitoring of civil infrastructure: challenges and successes. *Journal of Civil Structural Health Monitoring*, 1(3):79–95, 2011.

- [58] T Bajcar, F Cimerman, B Širok, and M Ameršek. Impact assessment of traffic-induced vibration on natural gas transmission pipeline. *Journal of Loss Prevention in the process industries*, 25(6):1055–1068, 2012.
- [59] Jie Zhang, Zheng Liang, Ding Feng, Chuan Zhang, Chengyu Xia, and Yiliu Tu. Response of the buried steel pipeline caused by perilous rock impact: Parametric study. *Journal of Loss Prevention in the Process Industries*, 43:385–396, 2016.
- [60] Jinbao Yao, Rutao Zhao, Nan Zhang, and Dujuan Yang. Vibration isolation effect study of in-filled trench barriers to train-induced environmental vibrations. *Soil Dynamics and Earthquake Engineering*, 125:105741, 2019.
- [61] Sébastien Guenneau, Alexander Movchan, Gunnar Pétursson, and S Anantha Ramakrishna. Acoustic metamaterials for sound focusing and confinement. *New Journal of physics*, 9(11):399, 2007.
- [62] Richard V Craster and Sébastien Guenneau. *Acoustic metamaterials: Negative refraction, imaging, lensing and cloaking*, volume 166. Springer Science & Business Media, 2012.
- [63] Claire M Watts, Xianliang Liu, and Willie J Padilla. Metamaterial electromagnetic wave absorbers (adv. mater. 23/2012). *Advanced Materials*, 24(23):OP181–OP181, 2012.
- [64] A Poddubny, I Iorsh, P Belov, and Y Kivshar. Nat. photonics 7 (12), 948–957 (2013), 2013.
- [65] Yihao Yang, Huaping Wang, Faxin Yu, Zhiwei Xu, and Hongsheng Chen. A metasurface carpet cloak for electromagnetic, acoustic and water waves. *Scientific reports*, 6(1):1–6, 2016.
- [66] Stéphane Brûlé, Bogdan Ungureanu, Younes Achaoui, André Diatta, Ronald Aznavourian, Tryfon Antonakakis, Richard Craster, Stefan Enoch, and Sébastien Guenneau. Metamaterial-like transformed urbanism. *Innovative Infrastructure Solutions*, 2(1):1–11, 2017.

- [67] Stéphane Brûlé, Stefan Enoch, and Sebastien Guenneau. Experimental evidence of auxetic features in seismic metamaterials: Ellipticity of seismic rayleigh waves for subsurface architected ground with holes. *arXiv preprint arXiv:1809.05841*, 2018.
- [68] Stéphane Brûlé, Stefan Enoch, and Sébastien Guenneau. Role of nanophotonics in the birth of seismic megastructures. *Nanophotonics*, 8(10):1591–1605, 2019.
- [69] Andrea Colombi, Richard V Craster, Daniel Colquitt, Younes Achaoui, Sébastien Guenneau, Philippe Roux, and Matthieu Rupin. Elastic wave control beyond band-gaps: shaping the flow of waves in plates and half-spaces with subwavelength resonant rods. *Frontiers in Mechanical Engineering*, 3:10, 2017.
- [70] Orazio Casablanca, G Ventura, F Garescì, Bruno Azzerboni, Bernardino Chiaia, Massimo Chiappini, and G Finocchio. Seismic isolation of buildings using composite foundations based on metamaterials. *Journal of Applied Physics*, 123(17):174903, 2018.
- [71] Muamer Kadic, André Diatta, Tobias Frenzel, Sebastien Guenneau, and Martin Wegener. Static chiral willis continuum mechanics for three-dimensional chiral mechanical metamaterials. *Physical Review B*, 99(21):214101, 2019.
- [72] Yi Zeng, Yang Xu, Hongwu Yang, Muhammad Muzamil, Rui Xu, Keke Deng, Pai Peng, and Qiuqiao Du. A matryoshka-like seismic metamaterial with wide band-gap characteristics. *International Journal of Solids and Structures*, 185:334–341, 2020.
- [73] Sébastien Guenneau and AB Movchan. Analysis of elastic band structures for oblique incidence. *Archive for rational mechanics and analysis*, 171(1):129–150, 2004.
- [74] Dionisio Del Vescovo and Ivan Giorgio. Dynamic problems for metamaterials: review of existing models and ideas for further research. *International Journal of Engineering Science*, 80:153–172, 2014.

- [75] N Aravantinos-Zafiris and MM Sigalas. Large scale phononic metamaterials for seismic isolation. *Journal of Applied Physics*, 118(6):064901, 2015.
- [76] Parikshit Moitra, Brian A Slovick, Wei Li, Ivan I Kravchenko, Dayrl P Briggs, S Krishnamurthy, and Jason Valentine. Large-scale all-dielectric metamaterial perfect reflectors. *Acs Photonics*, 2(6):692–698, 2015.
- [77] Bogdan Ungureanu, Younes Achaoui, Stefan Enoch, Stéphane Brûlé, and Sébastien Guenneau. Auxetic-like metamaterials as novel earthquake protections. *arXiv preprint arXiv:1510.08785*, 2015.
- [78] Bogdan Ungureanu, Sebastien Guenneau, Younes Achaoui, Andre Diatta, Mohamed Farhat, Harsha Hutridurga, Richard V Craster, Stefan Enoch, and Stephane Brûlé. The influence of building interactions on seismic and elastic surface waves. *arXiv preprint arXiv:1904.04133*, 2019.
- [79] Andrea Colombi, Daniel Colquitt, Philippe Roux, Sebastien Guenneau, and Richard V Craster. A seismic metamaterial: The resonant metawedge. *Scientific reports*, 6(1):1–6, 2016.
- [80] André Diatta, Younes Achaoui, Stéphane Brûlé, Stefan Enoch, and Sébastien Guenneau. Control of rayleigh-like waves in thick plate willis metamaterials. *AIP Advances*, 6(12):121707, 2016.
- [81] Matthew Mosby and Karel Matouš. Computational homogenization at extreme scales. *Extreme Mechanics Letters*, 6:68–74, 2016.
- [82] A Palermo, S Krodel, A Marzani, and C Daraio. Engineered metabarrier as shield from seismic surface waves. *sci rep* 6: 39356, 2016.
- [83] Yi-fan Liu, Jian-kun Huang, Ya-guang Li, and Zhi-fei Shi. Trees as large-scale natural metamaterials for low-frequency vibration reduction. *Construction and Building Materials*, 199:737–745, 2019.

- [84] CW Lim et al. Elastic waves propagation in thin plate metamaterials and evidence of low frequency pseudo and local resonance bandgaps. *Physics Letters A*, 383(23):2789–2796, 2019.
- [85] Feifei Sun and Lei Xiao. Bandgap characteristics and seismic applications of inerter-in-lattice metamaterials. *Journal of Engineering Mechanics*, 145(9):04019067, 2019.
- [86] EN Economou and MM Sigalas. Classical wave propagation in periodic structures: Cermet versus network topology. *Physical Review B*, 48(18):13434, 1993.
- [87] Daniel Mandelik, HS Eisenberg, Y Silberberg, R Morandotti, and JS Aitchison. Band-gap structure of waveguide arrays and excitation of floquet-bloch solitons. *Physical review letters*, 90(5):053902, 2003.
- [88] Alvaro Gómez-León and Gloria Platero. Floquet-bloch theory and topology in periodically driven lattices. *Physical review letters*, 110(20):200403, 2013.
- [89] Francisco Meseguer, M Holgado, D Caballero, N Benaches, Cefe Lopez, J Sanchez-Dehesa, and J Llinares. Two-dimensional elastic bandgap crystal to attenuate surface waves. *Journal of lightwave technology*, 17(11):2196–2201, 1999.
- [90] Mamdouh R Gadallah and Ray L Fisher. *Applied seismology: A comprehensive guide to seismic theory and application*. Number Sirsi) i9781593700225. 2005.
- [91] Steven Lawrence Kramer. *Geotechnical earthquake engineering*. Pearson Education India, 1996.
- [92] SR Chestler and KC Creager. Evidence for a scale-limited low-frequency earthquake source process. *Journal of Geophysical Research: Solid Earth*, 122(4):3099–3114, 2017.
- [93] Masaru Nakano, Takane Hori, Eiichiro Araki, Shuichi Kodaira, and Satoshi Ide. Shallow very-low-frequency earthquakes accompany slow slip events in the nankai subduction zone. *Nature communications*, 9(1):1–8, 2018.

- [94] Stéphane Brûlé, Stefan Enoch, and Sébastien Guenneau. Emergence of seismic metamaterials: Current state and future perspectives. *Physics Letters A*, 384(1):126034, 2020.
- [95] Y Achaoui, T Antonakakis, S Brûlé, RV Craster, S Enoch, and S Guenneau. Clamped seismic metamaterials: ultra-low frequency stop bands. *New Journal of Physics*, 19(6):063022, 2017.
- [96] Davide Bigoni, Sébastien Guenneau, Alexander B Movchan, and Morvan Brun. Elastic metamaterials with inertial locally resonant structures: Application to lensing and localization. *Physical Review B*, 87(17):174303, 2013.
- [97] Pai Wang, Filippo Casadei, Sicong Shan, James C Weaver, and Katia Bertoldi. Harnessing buckling to design tunable locally resonant acoustic metamaterials. *Physical review letters*, 113(1):014301, 2014.
- [98] Pai Wang, Ling Lu, and Katia Bertoldi. Topological phononic crystals with one-way elastic edge waves. *Physical review letters*, 115(10):104302, 2015.
- [99] Tobias Frenzel, Julian Köpfler, Erik Jung, Muamer Kadic, and Martin Wegener. Ultrasound experiments on acoustical activity in chiral mechanical metamaterials. *Nature communications*, 10(1):1–6, 2019.
- [100] Clive L Dym and Harry E Williams. Estimating fundamental frequencies of tall buildings. *Journal of Structural Engineering*, 133(10):1479–1483, 2007.
- [101] Clive L Dym. Approximating frequencies of tall buildings. *Journal of Structural Engineering*, 139(2):288–293, 2013.
- [102] Junuthula Narasimha Reddy. *Introduction to the finite element method*. McGraw-Hill Education, 2019.
- [103] Nico Van der Aa, H Ter Morsche, and R Mattheij. Computation of eigenvalue and eigenvector derivatives for a general complex-valued eigensystem. *The electronic journal of linear algebra*, 16:300–314, 2007.

- [104] Elias Jarlebring, Giampaolo Mele, and Olof Runborg. The waveguide eigenvalue problem and the tensor infinite arnoldi method. *SIAM Journal on Scientific Computing*, 39(3):A1062–A1088, 2017.
- [105] Huang-Ming Lee and Jong-Ching Wu. Transmittance spectra in one-dimensional superconductor-dielectric photonic crystal. *Journal of Applied Physics*, 107(9):09E149, 2010.
- [106] Francois Duplan, Ariane Abou-Chakra, Anaclet Turatsinze, Gilles Escadeillas, S Brule, and F Masse. Prediction of modulus of elasticity based on micromechanics theory and application to low-strength mortars. *Construction and Building Materials*, 50:437–447, 2014.
- [107] E Sapountzakis, P Syrimi, and I Antoniadis. Engineered metabarrier as shield from seismic surface waves. *Int. J. Geoen. Case Hist*, 4:289–305, 2018.
- [108] MZ Hossain, C-J Hsueh, B Bourdin, and K Bhattacharya. Effective toughness of heterogeneous media. *Journal of the Mechanics and Physics of Solids*, 71:15–32, 2014.
- [109] F Barthelat and HD Espinosa. An experimental investigation of deformation and fracture of nacre–mother of pearl. *Experimental mechanics*, 47(3):311–324, 2007.
- [110] Bingfeng Wang, Bingqing Zhou, and Xiaoyong Zhang. A high toughness and light weight armor structure bioinspired design based on a bovine hoof wall. *Materials Letters*, 264:127296, 2020.
- [111] T Venkatesh Varma and Saikat Sarkar. Designing polymer metamaterial for protective armor: a coarse-grained formulation. *Meccanica*, 56(2):383–392, 2021.
- [112] T Venkatesh Varma, Bogdan Ungureanu, Saikat Sarkar, Richard Craster, Sebastien Roger Louis Guenneau, and Stéphane Brûlé. The influence of clamping, structure geometry and material on seismic metamaterial performance. *Frontiers in Materials*, 8:106, 2021.

- [113] KH Pham and K Ravi-Chandar. The formation and growth of echelon cracks in brittle materials. *International Journal of Fracture*, 206(2):229–244, 2017.
- [114] Robert O Ritchie. The conflicts between strength and toughness. *Nature materials*, 10(11):817–822, 2011.
- [115] Jiyu Sun and Bharat Bhushan. Hierarchical structure and mechanical properties of nacre: a review. *Rsc Advances*, 2(20):7617–7632, 2012.
- [116] John D Currey. Hierarchies in biomineral structures. *Science*, 309(5732):253–254, 2005.
- [117] Francois Barthelat, Zhen Yin, and Markus J Buehler. Structure and mechanics of interfaces in biological materials. *Nature Reviews Materials*, 1(4):1–16, 2016.
- [118] Fabrizio Greco, Lorenzo Leonetti, Andrea Pranno, and Stephan Rudykh. Mechanical behavior of bio-inspired nacre-like composites: A hybrid multiscale modeling approach. *Composite Structures*, 233:111625, 2020.
- [119] Yongtae Kim, Youngsoo Kim, Flavia Libonati, and Seunghwa Ryu. Designing tough isotropic structural composite using computation, 3d printing and testing. *Composites Part B: Engineering*, 167:736–745, 2019.
- [120] Chaoqun Zhang, Daniel A Mcadams, and Jaime C Grunlan. Nano/micro-manufacturing of bioinspired materials: a review of methods to mimic natural structures. *Advanced Materials*, 28(30):6292–6321, 2016.
- [121] Seyed Mohammad Mirkhalaf Valashani and Francois Barthelat. A laser-engraved glass duplicating the structure, mechanics and performance of natural nacre. *Bioinspiration & biomimetics*, 10(2):026005, 2015.
- [122] Lionel Vargas-Gonzalez, Robert F Speyer, and James Campbell. Flexural strength, fracture toughness, and hardness of silicon carbide and boron carbide armor ceramics. *International Journal of Applied Ceramic Technology*, 7(5):643–651, 2010.

- [123] WY Wan Hanif, MS Risby, and Mazlee Mohd Noor. Influence of carbon nanotube inclusion on the fracture toughness and ballistic resistance of twaron/epoxy composite panels. *Procedia Engineering*, 114:118–123, 2015.
- [124] WL Goh, Y Zheng, J Yuan, and KW Ng. Effects of hardness of steel on ceramic armour module against long rod impact. *International Journal of Impact Engineering*, 109:419–426, 2017.
- [125] EA Flores-Johnson, Luming Shen, Irene Guiamatsia, and Giang D Nguyen. Numerical investigation of the impact behaviour of bioinspired nacre-like aluminium composite plates. *Composites Science and Technology*, 96:13–22, 2014.
- [126] C Kuhn and R Müller. A discussion of fracture mechanisms in heterogeneous materials by means of configurational forces in a phase field fracture model. *Computer Methods in Applied Mechanics and Engineering*, 312:95–116, 2016.
- [127] Neng Wang and Shuman Xia. Cohesive fracture of elastically heterogeneous materials: an integrative modeling and experimental study. *Journal of the Mechanics and Physics of Solids*, 98:87–105, 2017.
- [128] CJ Hsueh, L Avellar, B Bourdin, G Ravichandran, and K Bhattacharya. Stress fluctuation, crack renucleation and toughening in layered materials. *Journal of the Mechanics and Physics of Solids*, 120:68–78, 2018.
- [129] Stella Brach, Erwan Tanné, Blaise Bourdin, and Kaushik Bhattacharya. Phase-field study of crack nucleation and propagation in elastic–perfectly plastic bodies. *Computer Methods in Applied Mechanics and Engineering*, 353:44–65, 2019.
- [130] Stella Brach. Effects of plasticity on the anisotropy of the effective fracture toughness. *International Journal of Fracture*, 226(2):181–196, 2020.
- [131] Guo-Jun Zhang, Jian-Feng Yang, Motohide Ando, and Tatsuki Ohji. Reactive hot pressing of alumina-silicon carbide nanocomposites. *Journal of the American Ceramic Society*, 87(2):299–301, 2004.

- [132] Alan Lai, Zehui Du, Chee Lip Gan, and Christopher A Schuh. Shape memory and superelastic ceramics at small scales. *Science*, 341(6153):1505–1508, 2013.
- [133] Patrick M Kelly and LR Francis Rose. The martensitic transformation in ceramics—its role in transformation toughening. *Progress in materials science*, 47(5):463–557, 2002.
- [134] Yu I Golovin, VV Korenkov, and B Ya Farber. Kinetics of martensite transformations in zirconium-based ceramics in nanoindentation. *Izvestiya Akademii Nauk. Rossijskaya Akademiya Nauk. Seriya Fizicheskaya*, 67(6):840–844, 2003.
- [135] Hunter A Rauch, Yan Chen, Ke An, and Z Yu Hang. In situ investigation of stress-induced martensitic transformation in granular shape memory ceramic packings. *Acta Materialia*, 168:362–375, 2019.
- [136] Ehsan Moshkelgosha and Mahmood Mamivand. Concurrent modeling of martensitic transformation and crack growth in polycrystalline shape memory ceramics. *Engineering Fracture Mechanics*, 241:107403, 2021.
- [137] Javier Sanchez, José Fulla, Carmen Andrade, and C Alonso. Stress corrosion cracking mechanism of prestressing steels in bicarbonate solutions. *Corrosion science*, 49(11):4069–4080, 2007.
- [138] Francesco Dal Corso, Davide Bigoni, and Massimiliano Gei. The stress concentration near a rigid line inclusion in a prestressed, elastic material. part i.: Full-field solution and asymptotics. *Journal of the Mechanics and Physics of Solids*, 56(3):815–838, 2008.
- [139] Davide Bigoni, Francesco Dal Corso, and Massimiliano Gei. The stress concentration near a rigid line inclusion in a prestressed, elastic material. part ii.: Implications on shear band nucleation, growth and energy release rate. *Journal of the Mechanics and Physics of Solids*, 56(3):839–857, 2008.

- [140] Luca Argani, Davide Bigoni, and Gennady Mishuris. Dislocations and inclusions in prestressed metals. *Proceedings of the Royal Society A: Mathematical, Physical and Engineering Sciences*, 469(2154):20120752, 2013.
- [141] SD Akbarov and Arzu Turan. Mathematical modelling and the study of the influence of initial stresses on the sif and err at the crack tips in a plate-strip of orthotropic material. *Applied mathematical modelling*, 33(9):3682–3692, 2009.
- [142] Sha-Xu Zhou and Xian-Fang Li. Full incremental elastic field induced by a mode-I crack in a prestressed orthotropic material. *Engineering Fracture Mechanics*, 235:107070, 2020.
- [143] Xinyan Guo, Bin Yu, Peiyan Huang, Xiaohong Zheng, and Chen Zhao. J-integral approach for main crack propagation of rc beams strengthened with prestressed cfrp under cyclic bending load. *Engineering Fracture Mechanics*, 200:465–478, 2018.
- [144] Nicolas Moës, Anthony Gravouil, and Ted Belytschko. Non-planar 3d crack growth by the extended finite element and level sets—part i: Mechanical model. *International journal for numerical methods in engineering*, 53(11):2549–2568, 2002.
- [145] Anthony Gravouil, Nicolas Moës, and Ted Belytschko. Non-planar 3d crack growth by the extended finite element and level sets—part ii: Level set update. *International journal for numerical methods in engineering*, 53(11):2569–2586, 2002.
- [146] Marc Dufloot. A study of the representation of cracks with level sets. *International journal for numerical methods in engineering*, 70(11):1261–1302, 2007.
- [147] N Stein, S Dölling, K Chalkiadaki, W Becker, and P Weißgraeber. Enhanced xfm for crack deflection in multi-material joints. *International Journal of Fracture*, 207(2):193–210, 2017.

- [148] Danas Sutula, Pierre Kerfriden, Tonie van Dam, and Stéphane PA Bordas. Minimum energy multiple crack propagation. part i: Theory and state of the art review. *Engineering Fracture Mechanics*, 191:205–224, 2018.
- [149] Danas Sutula, Pierre Kerfriden, Tonie van Dam, and Stéphane PA Bordas. Minimum energy multiple crack propagation. part-ii: discrete solution with xfem. *Engineering Fracture Mechanics*, 191:225–256, 2018.
- [150] Danas Sutula, Pierre Kerfriden, Tonie van Dam, and Stéphane PA Bordas. Minimum energy multiple crack propagation. part iii: Xfem computer implementation and applications. *Engineering Fracture Mechanics*, 191:257–276, 2018.
- [151] Thomas-Peter Fries. A corrected xfem approximation without problems in blending elements. *International Journal for Numerical Methods in Engineering*, 75(5):503–532, 2008.
- [152] Thomas-Peter Fries and Ted Belytschko. The extended/generalized finite element method: an overview of the method and its applications. *International journal for numerical methods in engineering*, 84(3):253–304, 2010.
- [153] Thomas-Peter Fries. Overview and comparison of different variants of the xfem. *PAMM*, 14(1):27–30, 2014.
- [154] Nicolas Moës, Mathieu Cloirec, Patrice Cartraud, and J-F Remacle. A computational approach to handle complex microstructure geometries. *Computer methods in applied mechanics and engineering*, 192(28-30):3163–3177, 2003.
- [155] Eric Feulvarch, Rémi Lacroix, Komlanvi Madou, Hubert Deschanel, and Moïse Pignol. 3d xfem investigation of the plasticity effect on fatigue propagation under thermo-mechanical loading. *International Journal of Fracture*, pages 1–9, 2021.
- [156] Peter Dumstorff and Günther Meschke. Crack propagation criteria in the framework of x-fem-based structural analyses. *International Journal for Numerical and Analytical Methods in Geomechanics*, 31(2):239–259, 2007.

- [157] Jeong-Ho Kim and Glaucio H Paulino. T-stress, mixed-mode stress intensity factors, and crack initiation angles in functionally graded materials: a unified approach using the interaction integral method. *Computer Methods in Applied Mechanics and Engineering*, 192(11-12):1463–1494, 2003.
- [158] NR Brodnik, S Brach, CM Long, G Ravichandran, B Bourdin, KT Faber, and K Bhattacharya. Fracture diodes: Directional asymmetry of fracture toughness. *Physical Review Letters*, 126(2):025503, 2021.
- [159] Alan T Zehnder. *Fracture mechanics*, volume 62. Springer Science & Business Media, 2012.
- [160] James R Rice et al. Mathematical analysis in the mechanics of fracture. *Fracture: an advanced treatise*, 2:191–311, 1968.
- [161] Chun-Jen Hsueh and Kaushik Bhattacharya. Homogenization and path independence of the j-integral in heterogeneous materials. *Journal of Applied Mechanics*, 83(10), 2016.
- [162] Patrick Laborde, Julien Pomschmier, Yves Renard, and Michel Salaün. High-order extended finite element method for cracked domains. *International Journal for Numerical Methods in Engineering*, 64(3):354–381, 2005.
- [163] Alan Arnold Griffith. Vi. the phenomena of rupture and flow in solids. *Philosophical transactions of the royal society of london. Series A, containing papers of a mathematical or physical character*, 221(582-593):163–198, 1921.
- [164] Wen-Xue Wang, Dongmei Luo, Yoshihiro Takao, and Koichi Kakimoto. New solution method for homogenization analysis and its application to the prediction of macroscopic elastic constants of materials with periodic microstructures. *Computers & structures*, 84(15-16):991–1001, 2006.
- [165] Zeyao Chen, Yi Min Xie, Zhe Wang, Qing Li, Xian Wu, and Shiwei Zhou. A comparison of fast fourier transform-based homogenization method to asymptotic homogenization method. *Composite Structures*, 238:111979, 2020.

- [166] Behrooz Hassani and Ernest Hinton. A review of homogenization and topology optimization i—homogenization theory for media with periodic structure. *Computers & Structures*, 69(6):707–717, 1998.
- [167] Martin Philip Bendsøe and Noboru Kikuchi. Generating optimal topologies in structural design using a homogenization method. *Computer methods in applied mechanics and engineering*, 71(2):197–224, 1988.
- [168] Nicole R Harlan, Rosa I Merino, José I Pena, Angel Larrea, Victor M Orera, Carlos González, Pedro Poza, and Javier LLorca. Phase distribution and residual stresses in melt-grown $\text{al}_2\text{o}_3\text{-zro}_2$ (y_2o_3) eutectics. *Journal of the American Ceramic Society*, 85(8):2025–2032, 2002.
- [169] Manunya Okhawilai, Tewarak Parnklang, Phattarin Mora, Salim Hiziroglu, and Sarawut Rimdusit. The energy absorption enhancement in aramid fiber-reinforced poly (benzoxazine-co-urethane) composite armors under ballistic impacts. *Journal of Reinforced Plastics and Composites*, 38(3):133–146, 2019.
- [170] Yu Zhou, Guoju Li, Qunbo Fan, Yangwei Wang, Haiyang Zheng, Lin Tan, and Xuan Xu. Study on protection mechanism of 30crmnmo-uhmwpe composite armor. *Materials*, 10(4):405, 2017.
- [171] J Jiusti, EH Kammer, L Neckel, NJ Lóh, W Trindade, AO Silva, ORK Montedo, and A De Noni Jr. Ballistic performance of al_2o_3 mosaic armors with gap-filling materials. *Ceramics International*, 43(2):2697–2704, 2017.
- [172] Weilan Liu, Zhaohai Chen, Zhaofeng Chen, Xingwang Cheng, Yangwei Wang, Xianhui Chen, Jingyi Liu, Binbin Li, and Shaogang Wang. Influence of different back laminate layers on ballistic performance of ceramic composite armor. *Materials & Design*, 87:421–427, 2015.
- [173] Teyfik Demir, Mustafa Übeyli, and R Orhan Yıldırım. Investigation on the ballistic impact behavior of various alloys against 7.62 mm armor piercing projectile. *Materials & Design*, 29(10):2009–2016, 2008.

- [174] K Krishnan, S Sockalingam, S Bansal, and SD Rajan. Numerical simulation of ceramic composite armor subjected to ballistic impact. *Composites Part B: Engineering*, 41(8):583–593, 2010.
- [175] EA Flores-Johnson, M Saleh, and L Edwards. Ballistic performance of multi-layered metallic plates impacted by a 7.62-mm apm2 projectile. *International Journal of Impact Engineering*, 38(12):1022–1032, 2011.
- [176] Yanfei Yang and Xiaogang Chen. Study of energy absorption and failure modes of constituent layers in body armour panels. *Composites Part B: Engineering*, 98:250–259, 2016.
- [177] Weilan Liu, Zhaofeng Chen, Xingwang Cheng, Yangwei Wang, Adjei Richard Amankwa, and Jiang Xu. Design and ballistic penetration of the ceramic composite armor. *Composites Part B: Engineering*, 84:33–40, 2016.
- [178] Marianne Wilhelm and Cynthia Bir. Injuries to law enforcement officers: the backface signature injury. *Forensic science international*, 174(1):6–11, 2008.
- [179] JL Park, YS Chi, MH Hahn, and TJ Kang. Kinetic dissipation in ballistic tests of soft body armors. *Experimental mechanics*, 52(8):1239–1250, 2012.
- [180] Mukesh Bajya, Abhijit Majumdar, Bhupendra Singh Butola, Sanjeev Kumar Verma, and Debarati Bhattacharjee. Design strategy for optimising weight and ballistic performance of soft body armour reinforced with shear thickening fluid. *Composites Part B: Engineering*, 183:107721, 2020.
- [181] Guosheng Ji, Yi Fang, Jie Zhou, and Xun Huang. Porous labyrinthine acoustic metamaterials with high transmission loss property. *Journal of Applied Physics*, 125(21):215110, 2019.
- [182] Viktor G Veselago. Electrodynamics of substances with simultaneously negative and. *Usp. fiz. nauk*, 92(7):517, 1967.

- [183] Krzysztof K Dudek, Ruben Gatt, and Joseph N Grima. 3d composite metamaterial with magnetic inclusions exhibiting negative stiffness and auxetic behaviour. *Materials & Design*, 187:108403, 2020.
- [184] Shuang Zhang, Wenjun Fan, NC Panoiu, KJ Malloy, RM Osgood, and SRJ Brueck. Experimental demonstration of near-infrared negative-index metamaterials. *Physical review letters*, 95(13):137404, 2005.
- [185] Corentin Coulais, Chris Kettenis, and Martin van Hecke. A characteristic length scale causes anomalous size effects and boundary programmability in mechanical metamaterials. *Nature Physics*, 14(1):40–44, 2018.